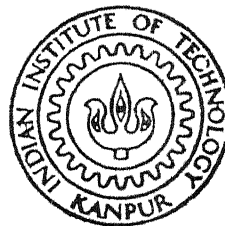


ANALYSIS OF DEFORMATIONS IN 9 Cr - 1Mo STEEL AND 316 STAINLESS STEEL

By

RAMACHANDRA UPADHYAYA K.



TH
ME/1988/M
Up1a

DEPARTMENT OF METALLURGICAL ENGINEERING
INDIAN INSTITUTE OF TECHNOLOGY, KANPUR
November, 1988

ANALYSIS OF DEFORMATIONS IN 9 Cr - 1Mo STEEL AND 316 STAINLESS STEEL

A Thesis Submitted
In Partial Fulfilment of the Requirements
for the Degree of
MASTER OF TECHNOLOGY

By
RAMACHANDRA UPADHYAYA K.

to the
DEPARTMENT OF METALLURGICAL ENGINEERING
INDIAN INSTITUTE OF TECHNOLOGY, KANPUR
November, 1988


26 APR 1989
CENTRAL LIBRARY
FLEET PAID
Acc. No. 1.104244

ME-1988-M-RAM-ANA

CERTIFICATE4/11/88
B₂

This is to certify that the present work "Analysis of Deformations in 9 Cr-1 Mo Steel and 316 Stainless Steel" has been carried out by Sri K. Ramachandra Upadhyaya under my supervision and it has not been submitted elsewhere for a degree.


November, 1988


M.N. Shetty
Professor
Department of Metallurgical Engineering
Indian Institute of Technology
Kanpur, India

CERTIFICATE4/11/88
B

This is to certify that the present work "Analysis of Deformations in 9 Cr-1 Mo Steel and 316 Stainless Steel" has been carried out by Sri K. Ramachandra Upadhyaya under my supervision and it has not been submitted elsewhere for a degree.

November, 1988


M.N. Shetty
Professor
Department of Metallurgical Engineering
Indian Institute of Technology
Kanpur, India

ACKNOWLEDGEMENTS

I express my sincere gratitude to Dr. M.N. Shetty, Department of Metallurgical Engineering, for his invaluable guidance and constant encouragement throughout the program.

Thanks are due to Mr. B.K. Jain of the ACMS for his kind help during the experimental work. I appreciate the timely helps of Mr. V.P. Gupta during the course of this work. The helps rendered by the staff of Metallurgical Engineering Workshop in preparing test samples are acknowledged thankfully.

I am greatly indebted to Messers A.M. Potdar, M.G. Muralidhara and H.K. Madhusudhana for their timely help during the final stages of preparation of this thesis. I thank all my friends whose association made my stay pleasant and memorable. Direct or indirect help of anybody for this thesis is acknowledged.

I cherish the kind and affectionate care taken by Dr. M.N. Shetty and his family which made me to feel homely during the stay.

I also thank Mr. R.N. Srivastava for his patient and neat typing.

Kanpur
November 1988

K. RAMACHANDRA UPADHYAYA

CONTENTS

	Page
LIST OF TABLES	v
LIST OF FIGURES	vi
NOMENCLATURE	x
ABSTRACT	xii
 1 INTRODUCTION	 1
1.1 Importance of the Materials Used	1
1.2 Objectives of the Present Work	2
 2 LITERATURE REVIEW AND THEORETICAL ANALYSIS	 5
2.1 Introduction	5
2.2 Thermally Activated Plastic Deformation	15
2.2.1 The determination of τ^* and τ_i	16
2.2.2 Energetics	19
2.2.3 Determination of m^*	21
2.2.4 Determination of activation parameters	22
2.2.5 Temperature dependence of m^*	24
2.2.6 Effect of strain on τ_i and τ^*	26
2.3 Dynamic Strain Ageing	26
2.4 Stress Relaxation	31
2.5 Load Cycling	37
 3 EXPERIMENTAL PROCEDURE	 44
3.1 Materials	44
3.2 Mechanical Testing	45
 4 RESULTS AND DISCUSSIONS	 52
4.1 General	52
4.2 Strain Rate Cycling	52
4.2.1 Determination of m^*	58
4.2.2 Stress components τ_i and τ^*	58
4.2.3 Activation parameters	68
4.3 Dynamic Strain Ageing	74
4.4 Stress Relaxation	80
4.5 Load Cycling	93
4.6 Toughness Measurements	104
 5 CONCLUSIONS	 112
REFERENCES	114

LIST OF TABLES

<u>Number</u>	<u>Title</u>	<u>Page</u>
2.1	Activation volume values for some thermally activated processes	9
3.1	Chemical compositions of the two steels in wt. %	44
4.1	Intercept U_0 and the slope S converted to shear values for the different test conditions	108
4.2	Estimated values of dislocation density and vacancy concentration for the two steels	108
4.3	Estimated entropy values due to dislocations and vacancies, total entropy and that attributed to the heat dissipation	111

LIST OF FIGURES

<u>Number</u>	<u>Title</u>	<u>Page</u>
2.1	An edge dislocation; open circles represent atom positions after motion	7
2.2	Variation in energy and stress with distance for a dislocation in a close packed direction	7
2.3	Thermally activated dislocation mechanisms	10
2.4	Internal stress fields encountered by a dislocation moving through the crystal lattice	10
2.5	Variation of stress with temperature and strain rate, showing thermal and athermal stress components	12
2.6	A common type of thermal activation barrier after reference 10	12
2.7	Variation of "m" with strain, strain rate and strain rate increment for polycrystalline iron at 300°K	23
2.8	Applied stress τ_A , effective stress τ^* and internal stress τ_i vs. strain for polycrystalline iron at 300°K	23
2.9	Temperature dependence of m^* for single crystals of iron and polycrystalline iron	25
2.10	Schematic sketch of load cycling with the load limits shown	39
3.1	Dimensions of the test samples	46
3.2	Microstructures of (a) the 9 Cr-1 Mo steel and (b) 316 SS	47
3.3	Schematic sketch of stress relaxation test	49
3.4	Schematic sketch of load cycling (a) without creep holds and (b) with creep holds of one minute at maximum load	51
4.1	Engineering stress-strain curves for the 9 Cr-1 Mo steel at different temperatures	53
4.2	Engineering stress-strain curves for the 316 SS at different temperatures	54

4.3	Variation of the flow stress and flow stress ratio $(\sigma_T/E_T)/(\sigma_{298}/E_{298})$ at yield and UTS	55
4.4	Some selected strain rate cycling curves for the 9 Cr-1 Mo steel	56
4.5	Some selected strain rate cycling curves for the 316 SS	57
4.6	Variation of reciprocal of strain rate sensitivity parameter, $m' (= 1/m = (\frac{\Delta \ln \dot{\gamma}}{\Delta \ln \tau}))$ at different temperatures for the 9 Cr-1 Mo steel	59
4.7	Variation of reciprocal of strain rate sensitivity parameter, $m' (= 1/m = (\frac{\Delta \ln \dot{\gamma}}{\Delta \ln \tau}))$ at different temperatures for the 316 SS	60
4.8	Variation of velocity stress exponent m^* with temperature ($V = \text{const. } (\tau^*)^{m^*}$, $\tau^* = \text{effective stress as in Figure 4.9}$)	61
4.9	Variation of shear stresses τ , τ^* and τ_i for the 9 Cr-1 Mo steel at (a) 298K (b) 423K (c) 723K and (d) 873K ($\tau^* = \text{effective stress}$, $\tau_i = \tau - \tau^*$ is the internal stress)	63
4.10	Variation of shear stresses τ , τ^* and τ_i for the 316 SS at (a) 298K, (b) 423K, (c) 573K and (d) 723K	65
4.11	Variation of the ratio of internal stress to the applied stress, α with shear strain at (a) 298K, (b) 423K, (c) 573K and (d) 723K	67
4.12	Activation volume V^* versus effective stress τ^* for (a) 9 Cr-1 Mo steel and (b) 316 SS	69
4.13	$\frac{V^* \tau^*}{kT}$ versus $1/kT$ for determination of activation energy	70
4.14	Normalised effective stress versus \bar{d}/b plot at different temperatures for (a) 9 Cr-1 Mo steel and (b) 316 SS	73
4.15	Engineering stress-strain curves for the 9 Cr-1 Mo steel in the dynamic strain ageing (DSA) regime	75
4.16	Appearance of serrations (DSA) at 523K at different strain rates for 9 Cr-1 Mo steel	76

4.17	Appearance of serrations (DSA) at 573K at different strain rates for 9 Cr-1 Mo steel	77
4.18	Appearance of serrations (DSA) at 648K at different strain rates for 9 Cr-1 Mo steel	78
4.19	Variation of critical strain at the appearance of DSA in 9 Cr-1 Mo steel as a function of strain rate at different temperatures	79
4.20	Variation of critical strain at the appearance of DSA as a function of temperature at different strain rates	79
4.21	Stress relaxation versus time at 3% tensile strain for the 9 Cr-1 Mo steel at different temperatures	81
4.22	Stress relaxation versus time at 4.7% tensile strain for the 9 Cr-1 Mo steel at different temperatures	82
4.23	Stress relaxation versus time at 6.0% tensile strain for the 9 Cr-1 Mo steel at different temperatures	83
4.24	Stress relaxation versus time at 25°C (298K) for the 9 Cr-1 Mo steel at different strain levels	85
4.25	Stress relaxation versus time at 450°C (723K) for the 9 Cr-1 Mo steel at different strain levels	86
4.26	Stress relaxation versus time at 3% tensile strain for the 316 SS at different temperatures	87
4.27	Stress relaxation versus time at 5.5% tensile strain for the 316 SS at different temperatures	88
4.28	Stress relaxation versus time at 8.2% tensile strain for the 316 SS at different temperatures	89
4.29	Stress relaxation versus time at 25°C (298K) for the 316 SS at different strain levels	90
4.30	Stress relaxation versus time at 150°C (423K) for the 316 SS at different strain levels	91
4.31	Activation volume determined from stress relaxation versus shear strain for the 9 Cr-1 Mo steel at different temperatures	94
4.32	Activation volume determined from stress relaxation versus shear strain for the 316 SS at different temperatures	95

4.33	Energy absorbed per cycle, ΔE_0 versus temperature at different strain levels for (a) 9 Cr-1 Mo steel and (b) 316 SS	96
4.34	Ratio of energy absorbed per cycle to twice the elastic energy versus temperature at different strains for (a) 9 Cr-1 Mo steel and (b) 316 SS	98
4.35	$\ln(\frac{V^* \Delta E}{kT})$ versus $1/kT$ for the two steels at (a) 2.5%, (b) 3.78% and (c) 5.57% shear strains	99
4.36	Variation of activation energy U_0 with temperature for 9 Cr-1 Mo steel at different strain levels	102
4.37	Variation of activation energy U_0 with temperature for the 316 SS at different strain levels	103
4.38	Variation of corrected toughness with temperature at different test conditions for (a) 9 Cr-1 Mo steel and (b) 316 SS	106

NOMENCLATURE

Some important symbols used in this thesis are listed out as below:

a	Cross-sectional area
A	Area swept by a dislocation line segment
b	Burgers vector
B	Dislocation mobility at unit shear stress
C_v	Vacancy concentration
d	Distance moved by dislocation after one full cycle
d^*	Activation distance
D, D_0	Diffusion coefficients
E	Modulus of load cell (used in load relaxation)
E_s	Strain energy per unit length of dislocation
F	Force on dislocation
G	Shear modulus
h	Plancks constant
k	Boltzmann constant
K	Number of activations per sec.
l	Effective radius of solute atmosphere around dislocation
l^*	Activation length
m	Strain rate sensitivity
m^*	Velocity stress exponent
Q_m	Activation energy for solute migration
R, r_0	Outer and inner cut off radii of stress field of a dislocation
S	Entropy

S_r	Slope of relaxed stress versus time plot
T	Temperature, $^{\circ}\text{K}$
U_0	Activation energy under no stress
$U(\tau^*, T)$	Activation energy under stress
v	Dislocation velocity
V^*	Activation volume
α	Geometric factor
α	Thermal expansion coefficient
β	Transmission coefficient
γ	Shear strain
$\dot{\gamma}$	Shear strain rate
ϵ	Tensile strain
$\dot{\epsilon}$	Tensile strain rate
θ	Coefficient of work hardening
ν	Poisson's ratio
ν	Frequency of dislocation
ρ	Dislocation density
σ	Tensile stress
τ	Shear stress
τ_t	Relaxation time
$\Delta\tau$	Incremental stress
$\Delta\tau_R$	Shear stress range in load cycling
ΔE	Energy absorbed per cycle in load cycling
$\Delta\gamma$	Maximum strain amplitude in hysteresis cycle.

ABSTRACT

Different aspects of plastic deformation are reviewed and analysed. A model is developed for the analysis of plastic deformation under low cycle fatigue conditions.

The following types of experiments were undertaken on 9 Cr-1 Mo steel and 316 stainless steel.

1. Constant strain rate tests - for strength and Dynamic Strain Ageing
2. Strain rate change tests to determine activation parameters
3. Stress relaxation tests
4. Load cycling between a tensile stress range below the flow stress, with and without creep holds to measure energy absorption in cyclic deformation.

Constant strain rate tests were used to obtain flow stress values at different temperatures. In the temperature range of 523-673K and strain rate range of 2.99×10^{-5} /sec to 1.19×10^{-3} /sec, the critical strain values for the onset of serrated flow were used to get the activation energy for solute migration and the process is identified as carbon diffusion. Strain rate change tests were made use of to determine effective and internal stresses, velocity stress exponent, activation volume and activation energy. From the activation parameters the dislocation mechanism controlling the rate of plastic deformation was identified and a force (F) - distance (d) relationship of the type $F \propto d^{-1/2}$ is obtained for the process.

To analyse the results of cyclic deformation the activation volume was separately obtained by stress relaxation experiments. Expressions are developed to correlate the energy absorption to a dislocation relaxation process. The temperature dependence of the energy absorption is examined and analysed in terms of a rate controlled dislocation relaxation process and its activation energy identified. It is found that the observations can be rationalised in terms of a model where dislocations undergo small fluctuations from pinned impurities giving rise to micro-strain and irreversible energy absorption in cyclic deformation. A number of data are presented with a possible similarity to internal friction.

Toughness values are analysed for the direct tensile tested samples and load cycled samples with and without creep holds at different temperatures. Density of dislocations and point defects, preferably vacancies are determined from the extrapolated toughness at 0°K . Nearly 50% of the entropy may be accounted for as arising from dislocations and vacancies. The remaining is attributed to the entropy of heat dissipation.

CHAPTER 1

INTRODUCTION

1.1 Importance of the Materials Used:

Both 9 Cr-1 Mo steel and 316 stainless steel (316 SS) are commercially important. 9 Cr-1 Mo ferritic steel, though originated mainly for oil industry in the 1930s, has now become one of the most important constructional materials. This material is well accepted as a structural material in the nuclear industry. It also finds its use in steam-generators, evaporators and parts of the superheaters of the Advanced Gas Cooled Reactors. It shows excellent strength and ductility, tolerance to variations in heat treatment and cold work, good microstructural stability [1], good creep resistance [2] and good corrosion resistance [3]. All these properties enhance the range of applicability of this material in nuclear industry. The general application is in the normalised and tempered condition.

AISI Type 316 stainless steel is a modification of the standard type 304 austenitic SS by the addition of molybdenum. It shows good creep and corrosion resistance. It is used for the construction of high temperature thermal power plants and is a candidate structural material for the fast breeder reactors. It is generally fabricated in the solution treated or slightly cold-worked state.

1.2 Objectives of the Present Work:

Both 9 Cr-1 Mo steel and 316 SS are high temperature materials. In the normalised and tempered condition, the microstructure of 9 Cr-1 Mo steel essentially consists of ferrite which is B.C.C. along with some martensite and carbide particles. 316 SS is austenitic (F.C.C.) with some amount of carbide precipitates in it. Thus, the two materials belong to two different crystal structures, microstructurally similar, and find similar applications.

The general application of these materials is in the temperature range of 100-500°C and therefore a knowledge of their flow properties in this temperature range is essential for design. In use, they undergo complex stress hysteresis resulting in creep and fatigue. An extensive evaluation of the tensile and creep properties are available [2, 4], but, there has been no significant efforts made to determine the fundamental deformation mechanisms, though some studies on 316 SS are available [5, 6]. Normally these materials are also known to exhibit dynamic strain ageing, with different combinations of temperature and strain rates.

An attempt has been made to identify the mechanisms under different conditions of flow by separately determining the activation parameters. The activation parameters for deformation are obtained by first determining the velocity-stress exponent (m^*), and then using this value along with the stress increment $\Delta\tau$ observed in instantaneous strain rate change tests, the effective and the internal stresses along the stress-strain curve are determined. Activation volume (V^*) and the total activation energy are

then obtained to identify a dislocation mechanism. The activation energy for dynamic strain ageing is determined by determining the critical strain for the onset of strain ageing in constant strain rate tests in the temperature range 523-673° K. With the combinations of temperature and strain rates used here, the 316 SS did not exhibit any dynamic strain ageing, and therefore the analysis is shown only for 9 Cr-1 Mo steel.

In the temperature range of their application both the materials are well into the domain of creep. Their yield and ultimate tensile strengths, toughness, etc. decrease and reach nominal values at temperatures at about half the melting point. In addition, temperature variations give rise to thermal stresses and other service factors lead to fatigue. Hence, the materials are simultaneously subjected to a combination of creep and fatigue under service conditions leading to creep-fatigue interaction. Though it is difficult to simulate these service conditions, a quantitative evaluation of the energy absorbed per cycle, under conditions of low cycle-fatigue with a constant tensile stress range with and without creep holds can nevertheless be made. A mathematical expression is developed to correlate the energy absorption to a rate controlling mechanism with an activation energy. Since energy absorption involves anelastic deformation, the activation volume in low cycle-fatigue is separately determined by stress relaxation experiments. It is found that this activation volume is about one fourth of that observed for plastic deformation.

Thus the work dwells upon five different aspects of deformation and its analysis:

- (1) Analysis of thermally activated deformation wherein the internal stress (τ_i), effective stress (τ^*) and activation volume (V^*) etc. are experimentally determined leading to the determination of an activation energy and a rate controlling deformation mechanism. The force distance curve for the dislocation-obstacle interaction is then worked out.
- (2) Dynamic strain ageing in the 9 Cr-1 Mo steel is then analysed to determine the activation energy for carbon diffusion.
- (3) Analysis of the stress relaxation under constant strain with an intention to determine activation volume is carried out.
- (4) A detailed analysis of the energy absorption characteristics in low cycle fatigue using a tensile stress range below the flow stress, with and without creep holds is carried out.
- (5) Analysis of the temperature dependence of toughness in both the steels is performed.

CHAPTER 2

LITERATURE REVIEW AND THEORETICAL ANALYSIS

2.1 Introduction:

Plastic deformation of metals is associated with dislocation motion under stress. During their motion, dislocations come across some obstacles or a spectrum of obstacles. The applied stress and thermal fluctuations of the dislocations assist them in overcoming these barriers. Plastic deformation depends upon the rate of overcoming these obstacles — the hardest obstacle controlling the rate of deformation at any given temperature. Hence an Arrhenius type equation can be used to describe the plastic deformation rate:

$$\dot{\gamma} = A \nu \exp -\left[\frac{U(\tau^*, T)}{kT}\right] \quad (2.1)$$

where

- $\dot{\gamma}$ is the shear strain rate,
- A is a constant,
- ν is the frequency factor and
- $U(\tau^*, T)$ is the activation energy.

The idea of expressing plastic deformation by this type of expression was originally conceived by Becker [7] without any consideration of dislocation motion.

A number of factors offer resistance to dislocation motion. In a perfect lattice, dislocation motion takes place by slight readjustments of atoms [ref. Figure 2.1]. The energy configuration

of a dislocation varies with its position in between the two equilibrium positions [ref. Figure 2.2]. The energy is maximum half way between the two equilibrium positions. The stress required to move a dislocation along this energy path is maximum at $x = b/4$ [ref. Figure 2.2]. This maximum stress is called Peierls-Nabarro stress [8, 9]. Peierls-Nabarro stress is the intrinsic resistance offered by an otherwise perfect crystal lattice to the motion of dislocation. The distance between two equilibrium positions being least in the close-packed planes and directions, Peierls-Nabarro stress is low for dislocation motion in these planes for F.C.C. and C.P.H. metals and is an effective source of resistance to dislocation motion at low temperatures.

The other crystal defects include point defects like vacancies, interstitials, substitutional atoms, etc. and surface defects like twin boundaries, grain boundaries, etc. The volume defects include precipitate particles, second phase particles, etc. The presence of these involve rearrangement of atoms and hence straining of the lattice and introduces local stress barriers in the lattice. Presence of dislocations also increases the internal stresses in the lattice. These stress fields are long range and extend to several interatomic distances.

During their motion, dislocations may intersect a stationary forest of dislocations threading the glide plane leading to jog or kink formation. These, along with the Peierls-Nabarro stress cause resistance to dislocation motion in the slip plane. Apart from these, screw dislocations may cross slip and edge dislocations may climb. These two represent resistance to the motion of dislocations out of the slip plane. All these are

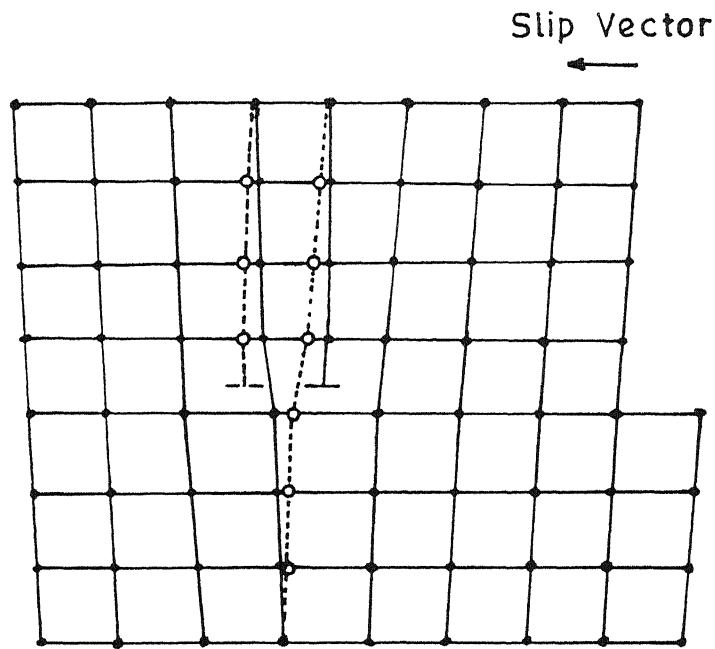


Fig:2.1 An Edge Dislocation; Open Circles Represent Atom positions After Motion

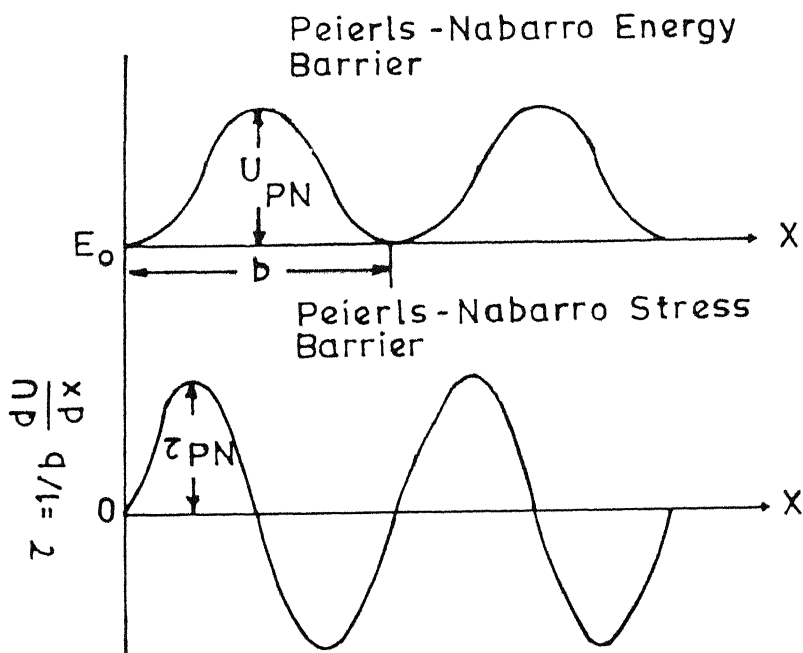


Fig:2.2 Variation in Energy and Stress with Distance for a Dislocation in a Close Packed Direction

represented in Figure 2.3. These barriers to dislocation motion are of short range in order, with an intensity distance of about 10 atomic diameters.

The dislocations should have high energy to overcome the long range obstacles. The energy associated with thermal fluctuations alone is not sufficient to assist dislocations in overcoming these barriers. The long range barriers which are generally independent of temperature are called athermal barriers. The short range obstacles can be overcome by the assistance of thermal vibrations since they are associated with small activation energy values. These constitute thermal obstacles resisting dislocation motion. Thermal fluctuations assist the applied stress in getting a dislocation segment of length l^* past the barrier. Detailed analysis of the mechanisms of the process, effect of stress on the activation energy for these thermal obstacles, etc., are given in a number of papers [10-18].

The activation energy $U(\tau^*, T)$, depends on the mechanism of activation. The effect of stress on activation energy may be negligibly small as in climb or appreciable as in intersection of dislocations. The activation length l^* and activation distance d^* over which dislocation segment l^* is to be moved by the stress determine the dependence of activation energy on stress. An activation volume V^* is defined as the change in $U(\tau^*, T)$ with respect to shear stress. Activation volumes vary from 1 to $10^4 b^3$ for different mechanisms as shown in Table 2.1.

At any position in the lattice a dislocation will experience a combined effect of long range and short range stress fields along with the Peierls-Nabarro stress. The internal stress field

encountered by a dislocation is shown in Figure 2.4. It is obvious that a positive internal stress opposes the dislocation motion and a negative internal stress aids it.

Table 2.1

Activation volume values for some thermally activated processes

Mechanism	Typical activation volume
Overcoming the Peierls-Nabarro stress	$10^1 - 10^2 b^3$
Intersection of forest dislocations resulting in the formation of two jogs	$10^2 - 10^4 b^3$
Non-conservative motion of jogs	$10^2 - 10^4 b^3$
Cross slip	$10^1 - 10^2 b^3$
Climb	$1 b^3$

As can be seen from Figure 2.4, the rate controlling process will be the thermally activated overcoming of the strongest short range obstacle situated near the top of the opposing long range stress field. At 0°K the applied stress needed to cause plastic flow is τ_0 . At any higher temperature, thermal fluctuations assist the applied stress, so that plastic flow occurs at a stress τ lower than τ_0 . Shaded area in Figure 2.4 gives the thermal energy required to overcome the barrier. As the temperature is increased τ can decrease upto τ_i which is the amplitude of the opposing long range stress field. The τ_i value depends only on the shear modulus and the dislocation density.

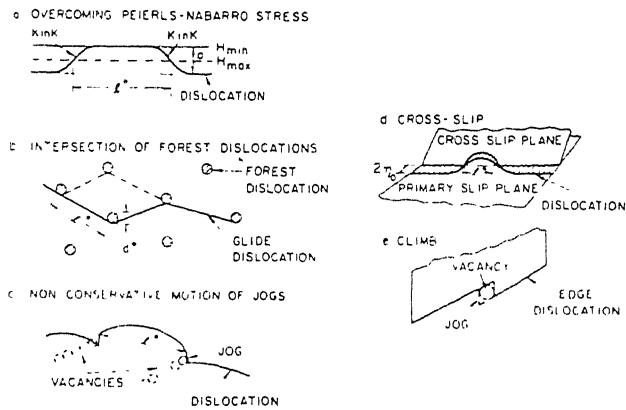


Fig. 2.3 Thermally activated dislocation mechanisms.

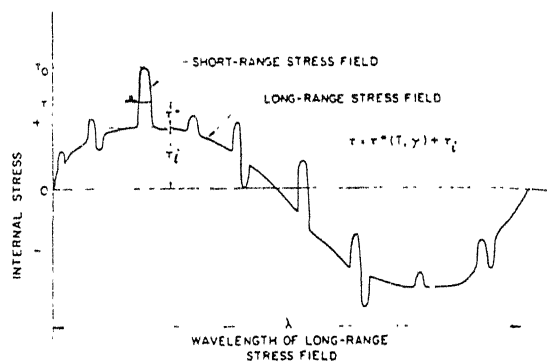


Fig. 2.4 Internal stress fields encountered by a dislocation moving through the crystal lattice.

Further increase in temperature will not have any effect on the stress required for plastic flow. The flow stress (τ) of a material can be represented as the sum of a thermal component (τ^*) and an athermal component (τ_i) [19]. τ_i and τ^* are termed internal and effective stresses respectively. The internal stress depends on the temperature only through the shear modulus, whereas the effective stress depends on temperature and strain rate. Accordingly,

$$\tau = \tau_i + \tau^*(T, \dot{\gamma}) . \quad (2.2)$$

The variation of yield or flow stress in this model is shown in Figure 2.5. The temperature at which τ^* becomes zero is represented by T_0 in Figure 2.5. At this temperature the entire energy for overcoming the short range barrier is supplied by the thermal fluctuations. In actuality, the temperature T_0 may be above the melting temperature.

A thermal activation barrier where the energy barrier is not a function of τ^* is shown in Figure 2.6. Such a situation arises at the intersection of dislocations and during non-conservative motion of dislocations. Under the application of a stress $\tau > \tau_i$, the dislocation moves up the barrier to the position F given by

$$F = \tau^* b l^* \quad (2.3)$$

where

τ^* is the effective stress equal to the difference between the applied and internal stresses,

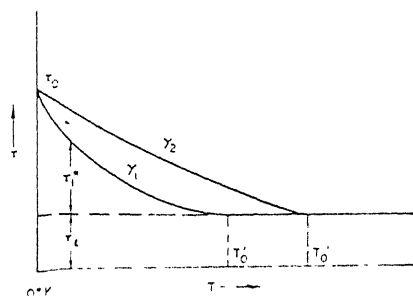


Fig. 2.5 Variation of stress with temperature and strain rate, showing thermal and athermal stress components.

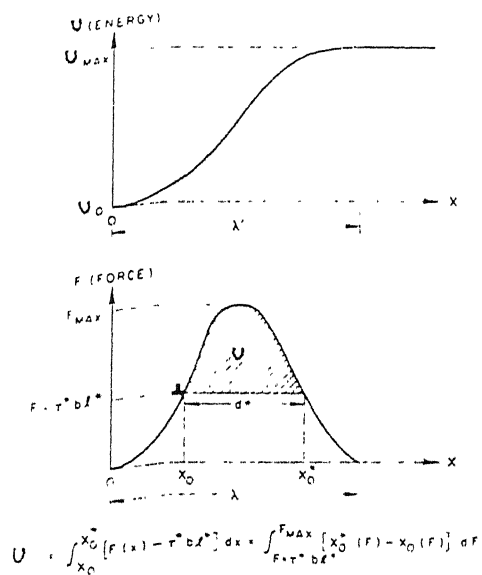


Fig. 2.6 A common type of thermal activation barrier after reference 10.

b is the Burgers vector and

l^* is the length of dislocation segment involved in the thermal activation.

The energy which must be supplied by thermal fluctuations to overcome the obstacle is given by the shaded area under the curve in Figure 2.6 and is designated by $U(\tau^*, T)$. Work done by the applied stress during thermal activation is:

$$W = \tau^* b l^* d^* \quad (2.4)$$

where $d^* = x_O^* - x_O$.

The term $U(\tau^*, T)$ can be represented in two ways:

- (a) If U_O is taken as the total area under the force distance curve, then $U(\tau^*, T)$ is given by the difference between U_O and the total work done by the applied stress in overcoming the obstacle.

$$U = U_O - \left[\int_0^{x_O} F(x) dx + \tau^* b l^* d^* + \int_{x_O^*}^{x_\lambda} F(x) dx \right] \quad (2.5)$$

$$U = U_O - V^* \tau^* \quad (2.5a)$$

where V^* is simply the sum of the energy terms within the brackets divided by τ^* . Since V^* has the dimensions of a volume, it is termed as activation volume.

- (b) The term $U(\tau^*, T)$ is also given by the area under the force distance curve between x_O and x_O^* (designated as U^*) minus the work done by the applied stress during thermal activation i.e.

$$\begin{aligned}
 U(\tau^*, T) &= \int_{x_0}^{x_0^*} [F(x) - \tau^* b l^*] dx \\
 &= \int_{F=\tau^* b l^*}^{F_{\max}} [x_0^*(F) - x_0(F)] dF
 \end{aligned} \tag{2.6}$$

$$= U^* - V^* \tau^* \tag{2.6a}$$

$$\text{where } U^* = \int_{x_0}^{x_0^*} F(x) dx \quad \text{and} \quad V^* = - \frac{dU(\tau^*, T)}{d\tau^*} = b d^* l^*$$

The symbol V^* is termed the activation volume.

This analysis applies only to the situation where the energy barrier and l^* do not depend on the stress. For such cases where the energy barrier varies with stress (e.g. Peierls-Nabarro stress, cross-slip, etc.) there does not exist a single U versus distance curve and the situation is more complicated. In such cases V^* does not represent the product $b d^* l^*$, but simply gives $-dU(\tau^*, T)/d\tau^*$.

The identification of a rate controlling mechanism involves the determination of activation energy and activation volume. The rate of deformation is expressed as an Arrhenius type of equation involving the appropriate variables and activation energy. The equation is simplified to the form which would make it possible to estimate the activation energy associated with the process using experimentally obtained values. The activation energy so obtained and the activation volume calculated with the help of the simplified equations are compared with those values calculated for different mechanisms to identify the mechanism.

2.2 Thermally Activated Plastic Deformation:

Seeger [19], based on his studies on the flow stress on zinc and cadmium at different temperatures, suggested that the flow stress τ of a material can be represented as the sum of a temperature dependent component τ^* and a temperature independent component τ_i . He pointed out that the athermal component τ_i is due to the long range stress fields of dislocations and its dependence on the temperature is only through the shear modulus as:

$$\tau_i = \alpha G b \rho^{1/2} \quad (2.7)$$

where

α is a constant ranging between 0.1 and 0.2,

G is shear modulus,

b is Burgers vector of dislocation and

ρ is dislocation density.

The thermal component τ^* depends on the temperature and the strain rate.

The flow stress of a material at a temperature and strain rate can then be represented as in Eq. 2.2. The flow stress versus temperature plots show a flat region at higher temperatures. The stress in this region gives the athermal internal stress component τ_i . The thermal component τ^* , also termed as effective stress is given at any temperature by the difference between the applied stress τ and internal stress τ_i .

Based on the above concepts, Conrad and Weidersich [20] developed a thermodynamic theory of thermally activated deformation

in terms of τ^* and temperature. These were extended further by Christian and Masters [21] and Li [22, 23].

There is contention about the usage of τ^* as a thermodynamic variable [24, 25, 26]. Hirth and Nix [27] support the idea that τ^* and T are the natural variables to use in comparing experimental results with theory if a local activation site can be pin pointed.

The stress field envisaged in the Seeger-Conrad-Weidersich approach is as shown in Figure 2.4. The long range internal stress field is assumed to be periodic with a wavelength λ . Superimposed on this are the short range stress fields. Thermal fluctuations assist the applied stress in moving the dislocation segment past the thermal obstacles since the latter are low energy barriers. Dislocations cannot overcome the long range stress fields by thermal fluctuations alone. The short range stress fields of highest energy situated near or on the maximum of the long range stress field will control the plastic deformation. The detailed analysis of common thermal activation mechanisms are reported in a number of publications [10-18].

Each mechanism can be identified by the activation parameters namely activation energy and quantitative variation of activation energy with shear stress. Change in $U(\tau^*, T)$ with respect to shear stress is termed as the activation volume, $V^* = -dU(\tau^*, T)/d\tau^*$. In the case of thermal activation where the energy barrier is not a function of stress we have $V^* = b d^* l^*$.

2.2.1 The determination of τ^* and τ_i :

The dislocation velocity is a strong function of the stress and temperature [28, 29, 30]. Usually the

effective stress acting on a dislocation line is differentiated from the applied stress during deformation [31, 32, 33].

Following dislocation velocity measurements in LiF, Jhonston and Gilman [28] obtained an empirical relationship:

$$v = B \tau^{*m^*} \quad (2.8)$$

where

- v is the dislocation velocity,
- B is dislocation mobility at unit shear stress,
- τ^* is effective shear stress and
- m^* is the velocity stress exponent.

The constant m^* is characteristic of a material and dependent on temperature. The relationship in the Eq. 2.8 has since then been confirmed by other research workers [29, 30, 31].

Dynamic aspects of crystal plasticity are related to the dislocation mobility. The relationship between the shear strain rate $\dot{\gamma}$, the mobile dislocation density ρ , and the average velocity of these dislocations is given by [34]

$$\dot{\gamma} = \alpha b \rho v \quad (2.9)$$

where

- b is Burgers vector of the dislocations and
- α is a geometric factor.

Combining equations 2.8 and 2.9 we can write

$$\dot{\gamma} = \alpha b \rho B \tau^{*m^*} \quad (2.10)$$

The mobile dislocation density is assumed to be unchanging with the strain rate, provided the changes in strain rates are not

very high. Equation 2.10 can also be represented as:

$$\ln \dot{\gamma} = \ln(\alpha b B) + \ln \rho + m^* \ln \tau^* \quad (2.11)$$

Differentiating this we get:

$$\partial \ln \dot{\gamma} = \partial \ln(\alpha b B) + \partial \ln(\rho) + m^* \partial \ln \tau^* \quad (2.12)$$

From the aforesaid assumptions this reduces to

$$\partial \ln \dot{\gamma} = m^* \partial \ln \tau^* \quad (2.13)$$

For the instantaneous strain rate change tests we can write this equation as:

$$m^* = \left(\frac{\Delta \ln \dot{\gamma}}{\Delta \ln \tau^*} \right)_{T, \gamma} \quad (2.14)$$

The Eq. 2.14 can be written in the form

$$\ln \left(\frac{\tau_2^*}{\tau_1^*} \right) = \ln \frac{\tau_1^* + \Delta \tau^*}{\tau_1^*} = \frac{1}{m} \ln \frac{\dot{\gamma}_2}{\dot{\gamma}_1} \quad (2.15)$$

where τ_1^* and τ_2^* are the effective stresses at the strain rates $\dot{\gamma}_1$ and $\dot{\gamma}_2$, respectively and $\Delta \tau^*$ is the change in effective stress associated with the strain rate change. From the assumption, that during the strain rate change there is no variation of internal stress, the change in effective stress $\Delta \tau^*$ is equal to the change in applied stress $\Delta \tau$. Using this, Eq. 2.15 can be solved for τ_1^* to get

$$\tau_1^* = \frac{\Delta \tau}{(\dot{\gamma}_2 / \dot{\gamma}_1)^{1/m^*} - 1} \quad (2.16)$$

Since the effective stress is given by

$$\tau^* = \tau - \tau_i \quad (2.17)$$

we can find out τ_i as

$$\tau_i = \tau - \frac{\Delta\tau}{(\dot{\gamma}_2/\dot{\gamma}_1)^{1/m^*} - 1} \quad (2.18)$$

The use of Eqs. 2.16 and 2.18 is based on two assumptions:

1. The Jhonston-Gilman velocity stress relationship is valid throughout the deformation.
2. m^* is independent of strain.

Validation of these assumptions is confirmed by the studies on LiF crystals [28] and single crystalline and polycrystalline pure iron [32].

2.2.2 Energetics:

The shear strain rate is given by

$$\dot{\gamma} = N A b \nu \exp \left[- \frac{U(\tau^*, T)}{kT} \right] = \dot{\gamma}_0 \exp \left[- \frac{U(\tau^*, T)}{kT} \right] \quad (2.19)$$

where

N is the number of activation sites per unit volume,

A is the area swept by a dislocation line segment during thermal activation,

ν is the frequency of vibration associated with the dislocation segment,

k is Boltzmann constant,

$\dot{\gamma}_0 = N A b \nu$ and

$U(\tau^*, T)$ is the thermal component of the total activation energy U_0 expressed as:

$$U(\tau^*, T) = U_0 - V^* \tau^* \quad (2.20)$$

For a single rate controlling mechanism, where $U(\tau^*, T)$ is primarily a function of τ^* , and the frequency factor $\dot{\gamma}_0$ does not change with temperature or stress it can be shown that [20]:

$$U(\tau^*, T) = -kT^2 \left(\frac{\partial \ln \dot{\gamma}}{\partial \tau} \right) \frac{\partial \tau^*}{\partial T} \quad (2.21)$$

$$= -kT^2 \left(\frac{\partial \ln \dot{\gamma}}{\partial \tau} \right) \left[\frac{\partial \tau}{\partial T} - \frac{\tau_i}{G} \cdot \frac{dG}{dT} \right] \quad (2.21a)$$

for constant strain rate tests. Also

$$V^* = - \frac{dU(\tau^*, T)}{d\tau^*} = kT \left(\frac{\partial \ln \dot{\gamma}}{\partial \tau} \right)_{T, \gamma} \quad (2.22)$$

$$= k \frac{\ln(\dot{\gamma}_0/\dot{\gamma})}{(\partial \tau^*/\partial T)_{\gamma}} \quad (2.22a)$$

Equation 2.19 can be rearranged to give

$$U(\tau^*, T) = -kT \ln(\dot{\gamma}/\dot{\gamma}_0) \quad (2.23)$$

The significance of the above equations is that, an evaluation of the deformation process can be done experimentally, from the knowledge of the three macro-deformation partials

$$\left(\frac{\partial \ln \dot{\gamma}}{\partial (1/T)} \right)_{\tau^*}, \quad \left(\frac{\partial \tau^*}{\partial T} \right) \quad \text{and} \quad \left(\frac{\partial \ln \dot{\gamma}}{\partial \tau} \right)$$

The values of $U(\tau^*, T)$, V^* and γ can also be obtained from measurements on the effect of stress and temperature on dislocation velocity by replacing the strain rate term in Eqs. 2.19 to 2.23

with the dislocation velocity v . The assumption is that $U(\tau^*, T)$ is a function of effective stress, independent of temperature. If $U(\tau^*, T)$ is a strong function of temperature, Eqs. 2.22, 2.22a and 2.23 are not valid and these should be replaced by

$$\frac{dU(\tau^*, T)}{d\tau^*} = kT \left\{ \left(\frac{\partial \ln \dot{\gamma}}{\partial \tau} \right)_{\tau^*} - \left[\frac{\partial (T \frac{\partial \ln \dot{\gamma}}{\partial T})}{\partial T} \right]_{\tau^*} \right\} \quad (2.24)$$

$$= -kT^2 \left[\frac{\partial}{\partial T} \left(\frac{\partial \ln \dot{\gamma}}{\partial \tau} \right) \right]_{\tau^*, T} \quad (2.24a)$$

and

$$U(\tau^*, T) = kT \ln \frac{\gamma_0}{\dot{\gamma}} - T \left\{ \frac{\partial [kT \ln(\dot{\gamma}_0/\dot{\gamma})]}{\partial T} \right\}_{\tau^*} \quad (2.25)$$

2.2.3 The determination of m^* :

The constitutive equation for stress (τ) and strain rate ($\dot{\gamma}$) is

$$\tau = K \dot{\gamma}^m \Big|_{\gamma, T} \quad (2.26)$$

where K is a constant and m is the strain rate sensitivity. This equation on suitable differentiation gives:

$$m = \frac{\partial \ln \tau}{\partial \ln \dot{\gamma}}$$

i.e. $1/m = \frac{\partial \ln \dot{\gamma}}{\partial \ln \tau}$ (2.27)

The expression for strain rate as given in Eq. 2.9 on differentiation gives

$$\frac{\partial \ln \dot{\gamma}}{\partial \ln \tau} = \frac{\partial \ln v}{\partial \ln \tau} + \frac{\partial \ln \rho}{\partial \ln \tau} \quad (2.28)$$

Substituting from Eq. 2.13 in the above equation we get

$$\frac{1}{m} = m^* + \frac{\partial \ln \rho}{\partial \ln \tau^*} \quad (2.29)$$

At very small strains the contribution due to dislocation density is negligible [30]. This is true only if the strain is so small that only one dislocation moves. This gives,

$$m^* = \left(\frac{\partial \ln \dot{\gamma}}{\partial \ln \tau^*} \right)_{\gamma \rightarrow 0} = \left(\frac{1}{m} \right)_{\gamma \rightarrow 0} \quad (2.30)$$

The value of m^* is obtained by extrapolating $1/m$ versus shear strain curve to zero strain. This method though not very accurate gives reasonably close values of m^* if m values are not very low [29, 30]. Results of strain rate cycling tests on single crystalline and polycrystalline pure iron are shown in Figures 2.7 and 2.8 after reference 32.

Michalak [32] suggested another expression for m^* as follows:

$$m^* = \frac{1}{m} - \tau_i \frac{\Delta \ln \dot{\gamma}}{\Delta \tau} \quad (2.31)$$

The increase in $1/m$ with strain (ref. Figure 2.7) can be explained on the basis of this expression as due to the increase in internal stress with the increase in strain (ref. Figure 2.8). It is still assumed that m^* is constant.

2.2.4 Determination of activation parameters:

Once m^* is determined the stress components τ_i and τ^* can be calculated using Eqs. 2.16 to 2.18. Activation volume is then determined using the Eq. 2.22. Using the calculated activation

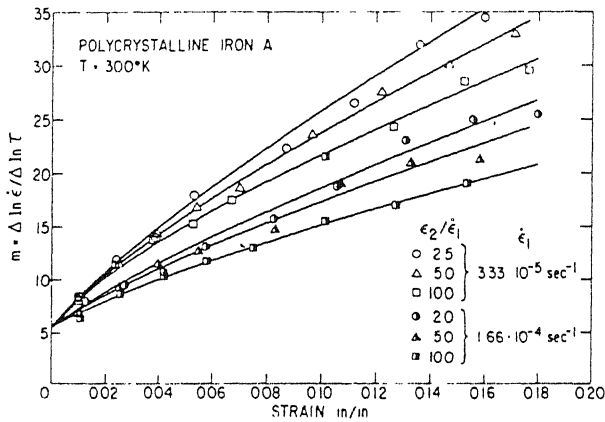


Fig. 2.7 Variation of "m" with strain, strain rate and strain rate increment for polycrystalline iron at 300°K .

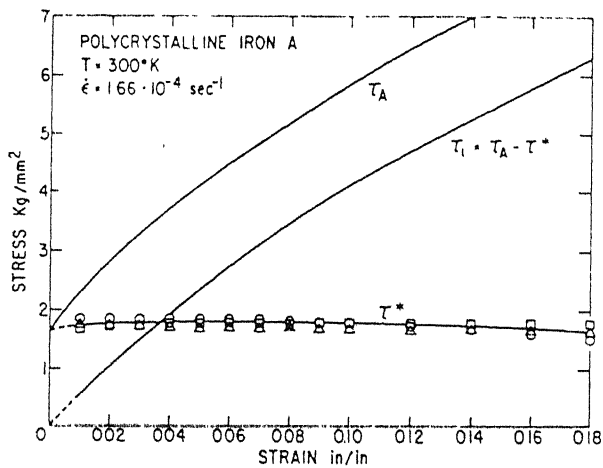


Fig. 2.8 Applied stress τ_A , effective stress τ^* and internal stress τ_i vs. strain for polycrystalline iron at 300°K .

volume and the effective stress, the stress dependent part of the activation energy $V^* \tau^*$ can be calculated at different temperatures. The activation energy is then determined from Eq. 2.20. Equation 2.19 can be rewritten as:

$$U(\tau^*, T) = -kT \ln(\dot{\gamma}/\dot{\gamma}_0) \quad (2.32)$$

On substituting this in Eq. 2.20 and on rearrangement, it gives

$$\frac{V^* \tau^*}{kT} = \frac{U_0}{kT} + \ln\left(\frac{\dot{\gamma}}{\dot{\gamma}_0}\right) \quad (2.33)$$

A plot of $\frac{V^* \tau^*}{kT}$ versus $1/kT$ gives a straight line with its slope giving U_0 and intercept giving the frequency parameter. Thus the thermal component of the activation energy is given by $-kT \ln \dot{\gamma}/\dot{\gamma}_0$. From the values of V^* and U_0 the activation process is characterised.

Frank [35] showed that Eq. 2.20 is valid even in the case of an obstacle spectrum, because the hardest obstacle with the highest activation energy would still be rate controlling. N of course, will then be represented in terms of an obstacle density distribution function for a slip plane and will cover all such possible slip systems in polycrystalline materials. For a single crystal, however, this will be a discrete sum.

2.2.5 The temperature dependence of m^* :

Temperature dependence of m^* in the sub-zero temperature range had been determined by etch pit technique and strain rate cycling method [30, 32, 36]. The results from the two methods are in good agreement (ref. Figure 2.9). However, below 200°K,

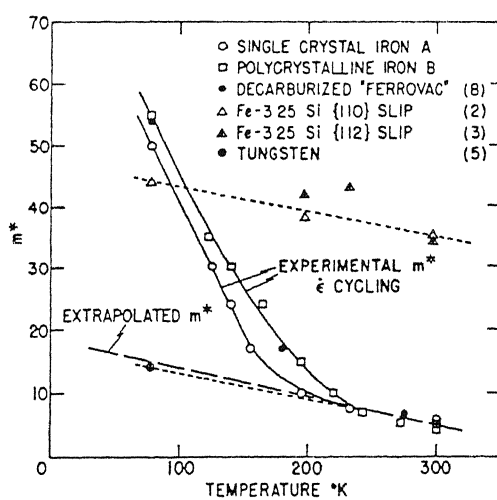


Fig. 2.9 Temperature dependence of m^* for single crystals of iron and polycrystalline iron.

the m^* values from strain rate cycling are found to be considerably higher than those obtained by etch pit technique, in the case of iron and other B.C.C. metals (ref. Figure 2.9).

It is observed that the value of m^* from strain rate cycling is considerably larger than the one from etch pit technique and that the strain rate sensitivity is strain independent [37]. Strain independent nature of strain rate sensitivity is also reported for iron below 175K [32].

It is suggested that strain rate change causes a large change in mobile dislocation density below 180K and hence gives a higher value for m^* than that obtained by etch pit technique [32]. However at higher temperatures this effect is negligible.

2.2.6 Effect of strain on τ_i and τ^* :

The effective stress remains almost independent of strain, whereas internal stress increases with strain. Works of Michalak [32] support this (ref. Figure 2.8). It is seen that effective stress slightly decreases with the increase in strain. This is attributed to the decrease in mobile dislocation density with strain. The internal stress is considered to be the long range stress exerted by dislocation tangles and cell walls [38]. Hence the increase in internal stress with strain can be explained as the effect of increased dislocation tangles and cell walls.

2.3 Dynamic Strain Ageing:

During tensile or compressive testing some materials exhibit repeated and systematic fluctuations of load in the load elongation curve. This serrated flow is attributed to the process

of dynamic strain ageing (DSA). The discontinuous flow is otherwise known also as Portevian-Le-Chatelier effect. This field is of much importance as revealed by numerous investigations. The temperature regime of serrated flow has been found to depend on the chemistry and strain rate [39] and grain size [40].

There is no clear consensus as to the details of the mechanisms of DSA. The early attempt to explain the mechanism was that of Cottrell [41, 42]. According to this model a solute atmosphere is formed about the moving dislocation, and dragged along the dislocations moving at less than a critical velocity,

$$v_c = \frac{4D}{l} \quad (2.34)$$

where

D is the solute diffusion coefficient and

l is the effective radius of the atmosphere given by

$$l = \frac{U_m b}{kT} \quad (2.35)$$

U_m is solute-dislocation binding energy.

The dislocations escape from the solute atmosphere under the application of stress and hence the load required to deform decreases. The process of formation of solute atmosphere around dislocations and the dislocations escaping from the solute atmosphere takes place repeatedly. This leads to a serrated flow.

According to this model, the serrated flow should start right from the beginning of plastic flow. But experimental results have shown that the onset of serrated flow at a critical strain which depends upon the strain rate and temperature. Further, in substitutional alloys, D is initially far too small to account

for the observed phenomenon. But the increase in vacancy concentration associated with the plastic deformation enhances diffusion of solute atoms. Dislocation velocity also decreases with straining. This results in a critical strain at which serrated flow begins.

The strain rate can be expressed in terms of the vacancy concentration (C_v) and the mobile dislocation density ρ [42, 43] as:

$$\dot{\epsilon} = 4 b \rho C_v D_o \exp(-Q_m/kT) \quad (2.36)$$

where

Q_m is the activation energy for migration of solute atoms and

D_o is the diffusion frequency parameter.

The increase in vacancy concentration and mobile dislocation density with strain can be expressed as:

$$C_v = K \epsilon^{m_1} \quad (2.37)$$

$$\rho = N \epsilon^\beta \quad (2.38)$$

Substitution of these values in Eq. 2.36 gives on rearrangement

$$\epsilon_c^{m_1+\beta} = \frac{1}{4 b K N D_o} \frac{\dot{\epsilon} \exp(Q_m/kT)}{\quad} \quad (2.39)$$

Measurement of the strain rate dependence and temperature dependence is in accordance with Eq. 2.39. Taking logarithms this can be written as:

$$(m_1 + \beta) \ln \epsilon_c = \ln\left(\frac{1}{4 b K N D_o}\right) + \ln \dot{\epsilon} + \left(\frac{Q_m}{kT}\right) \quad (2.40)$$

At a particular temperature a plot of $\ln \dot{\epsilon}$ versus $\ln \epsilon_c$ results in a straight line with a slope giving $(m_1 + \beta)$. The general values of $(m_1 + \beta)$ range from 1.6 to 3.3 [44, 45]. Value of Q_m is obtained from the slope of $\ln \epsilon_c$ versus $(1/T)$ at constant strain rate using the $(m_1 + \beta)$ value already obtained.

It is reported that critical strain variation with temperature shows a reversal at higher temperatures [46, 47]. This represents a delay in the onset of serrated flow. The explanation as given by Hayes and Hayes [46] for this phenomenon is given below.

1. Solute atmosphere form on moving dislocations.
2. Advancing lines of dislocations are arrested at precipitates.
3. Atmospheres condense on dislocation lines during the waiting time at the precipitate barriers.
4. Dislocation lines bow out between the precipitates during deformation (Orowan mechanism).
5. Carbon diffuses by pipe diffusion down these dislocation lines from the bowed out segment of the lines to the precipitate which acts as a sink for carbon.

These dislocation lines, then drained of carbon, move on in a normal fashion without producing serrations.

At higher temperatures solute precipitate reaction rate being higher, more and more solute is able to diffuse down the dislocation line to the precipitates. At lower strain rates, more time is available for the diffusion. Both these lead to a higher critical strain for the onset of serrated flow. Finally at very high strain the atmosphere formation rate at the dislocation

segment is higher than the rate of depletion. Hence normal serrated flow is observed at higher strains.

The variation of stress decrement can be used as a criterion for identifying the process controlling the DSA [46]. Stress decrement is reported to increase as strain or temperature is increased and/or strain rate is decreased. No anomalous behaviour was observed even at higher temperatures [46].

As the temperature is increased or the strain rate is decreased, the serrated flow disappears. This occurs by either a progressively longer strain to the onset of serrations (a strain delay mechanism) or by a progressively smaller strain to the disappearance of serrations (disappearance off the end of the flow curve). This is attributed to the precipitation reaction [48]. For a serrated flow there should be a minimum concentration of the solute atoms in the solute atmosphere around the dislocation. The precipitate particles acting as sink, deplete the arrested dislocations of their atmosphere species. In the temperature region where strain delay exists, serrations appear on the flow curve only after the delay sinks approach saturation. Serrations then progress until their disappearance off the end of the flow curve. This may be because of the reaction between the carbon atmosphere and the surrounding carbide forming species. This reaction occurs nearly simultaneously at all reaction sites with no long range diffusion of either reactants required.

In the DSA range materials exhibit a negative strain rate sensitivity [44, 48, 49] and an increase in work hardening rate [6, 49] with increase in temperature. Mulford and Kocks [49] made an attempt to explain the negative strain rate sensitivity by

considering the flow stress σ as the sum of σ_m relating to friction imposed by the solutes on the mobile dislocations and, σ_d relating to the dislocation-dislocation interaction which is the cause of strain hardening. Assuming this they derive two contributions m_f and m_d to the total strain rate sensitivity (m).

Following dislocation arrest theory of Sleeswyk [50] which involves formation of solute atmosphere on forest dislocation and draining of these by pipe diffusion to the mobile dislocation while they are waiting at the forest dislocations, Mulford and Kocks [49] conclude that the strength of obstacles increases with the waiting time resulting in a negative m_d . Role of pipe diffusion as a factor in the process causing serrations is also forwarded by other authors [47, 51].

2.4 Stress Relaxation:

When a tensile test in a hard beam machine is stopped the stress relaxes. The relaxation results from a limited continuation of glide initiated during yielding, if the material is held isothermally under stress. Dislocation 'hung ups' at obstacles in the glide planes are probably impelled to move to adjacent positions of lower potential energy in the internal stress fields and can do so only slowly as thermal activation assists the stress in overcoming the drag on dislocations [52]. This implies that the material continues to flow plastically even after the loading is stopped. Since the cross-head is stopped this results in a decrease in the stress with time.

The stress relaxation takes place from an initial value σ_0 to a value σ_t at any time t according to a logarithmic law [52] given by

$$(\sigma_0 - \sigma_t) = S_r \ln(1 + \nu t) \quad (2.41)$$

where

ν is a constant and

S_r is a constant depending upon the temperature and the strain at which relaxation is started.

The value of S_r can be approximated to

$$S_r = \frac{d\sigma}{d(\ln t)} \quad (2.42)$$

Creep and relaxation are related to each other in the sense, that the former involve continued dislocation glide under constant stress, whereas, the latter under constant strain [53]. The variation in stress with time can be expressed as:

$$\frac{d\sigma}{dt} = \frac{\partial \sigma}{\partial t} + \frac{\partial \sigma}{\partial \epsilon} \cdot \frac{d\epsilon}{dt} \quad (2.43)$$

where

ϵ is the strain and

$\partial \sigma / \partial \epsilon = \theta$, coefficient of work hardening i.e. $d\sigma / d\epsilon$.

For stress relaxation $\frac{d\epsilon}{dt} = 0$ and for creep $\frac{d\sigma}{dt} = 0$. From these it can be deduced that

$$\frac{d\sigma}{d \ln t} = -\theta \frac{d\epsilon}{d \ln t} \quad (2.44)$$

From Eq. 2.19 tensile strain rate can be expressed as:

$$\frac{d\epsilon}{dt} = 1.4 \frac{d\dot{\gamma}}{dt} = N A b \nu_0 \exp [-U(\tau^*, T)/kT] \quad (2.45)$$

This can be rewritten for activation energy as:

$$U(\tau^*, T) = U_0 - V^*(\tau - \tau_1) = kT \ln(\nu' t) \quad (2.46)$$

where $\nu' = N A b \nu_0$.

This on differentiation gives

$$- V^* d\tau = kT d(\ln t) \quad (2.47)$$

Taking $\sigma = 2\tau$ and rearranging, this reduces to

$$\frac{d\sigma}{d(\ln t)} = - \frac{2kT}{V^*} \quad (2.48)$$

From Eqs. 2.42 and 2.48,

$$S_r = - \frac{2kT}{V^*} \quad (2.49)$$

Now the stress dependent part of the activation energy can be obtained as:

$$V^*(\tau - \tau_i) = - \frac{2kT}{S_r} (\tau - \tau_i) \quad (2.50)$$

More elaborate analysis considering machine specimen interaction was given by Sargent [54] as follows.

The specimen is strained in the machine and the test stopped at some specimen length l_s corresponding to a load L . The load cell is regarded as a strong spring with a spring constant E . The spring length corresponding to load L is l_1 . Then the load cell and specimen may be considered as a system held rigidly between two points $l_1 + l_s$ apart. A change in length dl_s of the specimen due to plastic flow causes a load change,

$$- dL = E dl_s \quad (2.51)$$

and a corresponding change in stress given by:

$$d\sigma = \frac{dL}{a} \quad (2.52)$$

where 'a' is the cross-sectional area of the specimen.

Rate of relaxation can be expressed as

$$-\frac{d\sigma}{dt} = -\frac{dL}{a dt} = \frac{E}{a} \frac{dl_s}{dt} = \frac{E}{a} l_s \dot{\epsilon} \quad (2.53)$$

where $\dot{\epsilon}$ is the strain rate.

It is assumed that a single deformation process is controlling the rate of relaxation. Effective stress acting on the dislocation during thermal activation is given by:

$$\sigma_t^* = \sigma_t - \theta \epsilon_s - \sigma_i \quad (2.54)$$

where

σ_t^* is the effective tensile stress at any time t

σ_t is the observed tensile stress at the time t

θ is the coefficient of work hardening defined as

$\frac{d\sigma}{d\epsilon}$ which is assumed constant

σ_i is the internal stress assumed to remain constant, and

ϵ_s is the specimen strain which may be written as:

$$\epsilon_s = \frac{dl_s}{l_s} = \frac{a}{E l_s} (\sigma_o - \sigma_t) \quad (2.55)$$

where σ_o is the observed stress at t = 0.

From Eqs. 2.54 and 2.55,

$$\sigma_t^* = \sigma_t - \frac{\theta a}{E l_s} (\sigma_o - \sigma_t) - \sigma_i \quad (2.56)$$

The activation energy for the thermal activation is given by:

$$U(\tau^*, T) = U_o - V^* \tau^* \quad (2.20)$$

Using a resolution factor of 1/2 for a polycrystalline sample, to convert the tensile stress to the shear stress and combining Eqs. 2.56 and 2.20, we get:

$$U(\tau^*, T) = U_0 - \frac{V^*}{2} \left\{ \sigma_t - \frac{\theta a}{E l_s} (\sigma_0 - \sigma_t) - \sigma_i \right\} \quad (2.57)$$

The shear strain ^{rate}/expression (Eq. 2.19) can be written as:

$$\dot{\gamma} = \dot{\gamma}_0 \exp - \left[U_0 - \frac{V^*}{2} (\sigma_t - \sigma_i) + \frac{V^*}{2} \cdot \frac{\theta a}{E l_s} (\sigma_0 - \sigma_t) \right] / kT \quad (2.58)$$

Using a resolution factor of 1/1.4 to convert the tensile strain rate to shear strain rate and substituting from Eq. 2.58 in Eq. 2.53 to get relaxation rate as:

$$- \frac{d\sigma}{dt} = 1.4 \frac{E l_s}{a} \dot{\gamma}_0 \exp - \left[\frac{U_0 - \frac{V^*}{2} (\sigma_t - \sigma_i) + \frac{V^*}{2} \frac{\theta a}{E l_s} (\sigma_0 - \sigma_t)}{kT} \right] \quad (2.59)$$

If

$$C = 1.4 \frac{E l_s}{a} \dot{\gamma}_0 \exp - \left[\frac{U_0 + \frac{V^*}{2} (\sigma_t - \sigma_i) + \frac{V^*}{2} \frac{\theta a}{E l_s} (\sigma_0 - \sigma_t)}{kT} \right]$$

and

$$B = \frac{V^*}{2kT} \left[1 + \frac{\theta a}{E l_s} \right]$$

then Eq. 2.59 reduces to

$$- \frac{d\sigma}{dt} = C \exp(B\sigma) \quad (2.60)$$

Assuming that C and B are constants it follows by integration that

$$(\sigma_0 - \sigma_t) = \frac{1}{B} \ln [C B t \exp(B \sigma_0) + 1] \quad (2.61)$$

This is in the form of Feltham's logarithmic law (Eq. 2.41). The slope S_r of the $(\sigma_o - \sigma_t)$ versus $\ln t$ is identified as:

$$S_r = \frac{1}{B} = \frac{2kT}{V^* \left[1 + \frac{\theta a}{E l_s} \right]} \quad (2.62)$$

i.e. the slope is proportional to the reciprocal of the activation volume V^* for the process controlling the rate of flow.

Similarly the constant ν' is given by:

$$\nu' = C B \exp(B \sigma_o) \quad (2.63)$$

Thus using the experimental values it is possible to determine the activation volume according to Eq. 2.62. But no sound theoretical basis is provided for the logarithmic relationship between relaxed stress and time. Feltham [52] suggested that the jogs in screw dislocations may be responsible for the stress relaxation of F.C.C. metals. However, considering the energy required for the non conservative motion of jogs in screw dislocations this view cannot be accepted [54].

The technique of stress relaxation has been found quite useful to study the phenomenon of plastic strain prior to the yield point in molybdenum and columbium [55] and to study the plastic properties of copper [52], α -brass [53], α -iron [56], cobalt [57] and magnesium [58].

The effect of load stop and strain rate on the load relaxation in molybdenum and columbium was studied by Feltham [55]. According to him load relaxation at a constant strain rate increases linearly with increase in strain at which load relaxation is taking place. Interaction of mobile dislocations with either

pinning defects or grain boundaries might be resulting in this behaviour. The effect of loading rate on the amount of relaxation can be interpreted by assuming that initially, at each stress level, there are a certain number of free dislocations available for plastic flow. The area swept out by the free dislocations per unit time depends upon the applied stress. At low loading rates more time is spent at each stress level and hence fewer dislocations are available for relaxation at each constant load stop.

2.5 Load Cycling:

Fatigue studies and fatigue creep interaction studies are well established [59]. But these studies are confined to find either the number of cycles to failure or crack growth rates with an intention to confirm any one of the life prediction techniques. Fatigue experiments have been extensively carried out to measure internal friction [60]. No energy measurements during low cycle fatigue to understand the mechanism of deformation has been done. The present work aims at analysing the low cycle fatigue and low cycle fatigue-creep interaction behaviours in terms of thermal activation.

It is shown that energy absorbed per cycle decreases with the number of cycles during the first few cycles and reaches a constant value as number of cycles is increased. This constant value is reported to vary linearly with strain rate [61]. This suggests that some internal adjustments are taking place to accommodate the anelastic strain and this is generally called the 'relaxation phenomenon'.

The present analysis is done by measuring the energy absorption in a cyclic test using a tensile stress range lying between a minimum and maximum stress values, arbitrarily chosen to be some fixed fractions of the flow stress as shown in Figure 2.10.

Material is loaded in tension till some plastic strain is accumulated and a shear stress τ_m , corresponding to this plastic strain. Then it is unloaded and load cycled between a minimum stress $\tau_1 = 0.1 \tau_m$ and $\tau_2 = 0.95 \tau_m$. Since the loop area was generally quite small, a large stress range was chosen to obtain measurable energy absorption. The irreversible work done during each cycle ΔE is given by [62]

$$\Delta E = 2 \int_{\tau_1}^{\tau_2} \tau \, d\gamma = 2 \int_0^{\Delta\tau_R} \tau \, d\gamma = 2\tau_F \Delta\gamma \quad (2.63)$$

where, τ_F is the frictional stress and

$\Delta\gamma$ is the maximum strain amplitude in one hysteresis cycle, taken as the maximum width of loop.

The frictional stress τ_F is taken to be the sum of the Peierls-Nabarro stress τ_P and the internal stress τ_i considered earlier. τ_P estimations at 0°K for several F.C.C. and B.C.C. metals are available [63] and is in the range of $10^{-4} - 10^{-5} \text{ G}(0^\circ\text{K})$ with a lower value for B.C.C. metals. Moreover, the τ_P decreases with increasing temperature, as it depends exponentially on the negative of the dislocation width which increases with increasing temperature. Since the present measurements are all at the higher temperatures and since the τ_i values are in the range

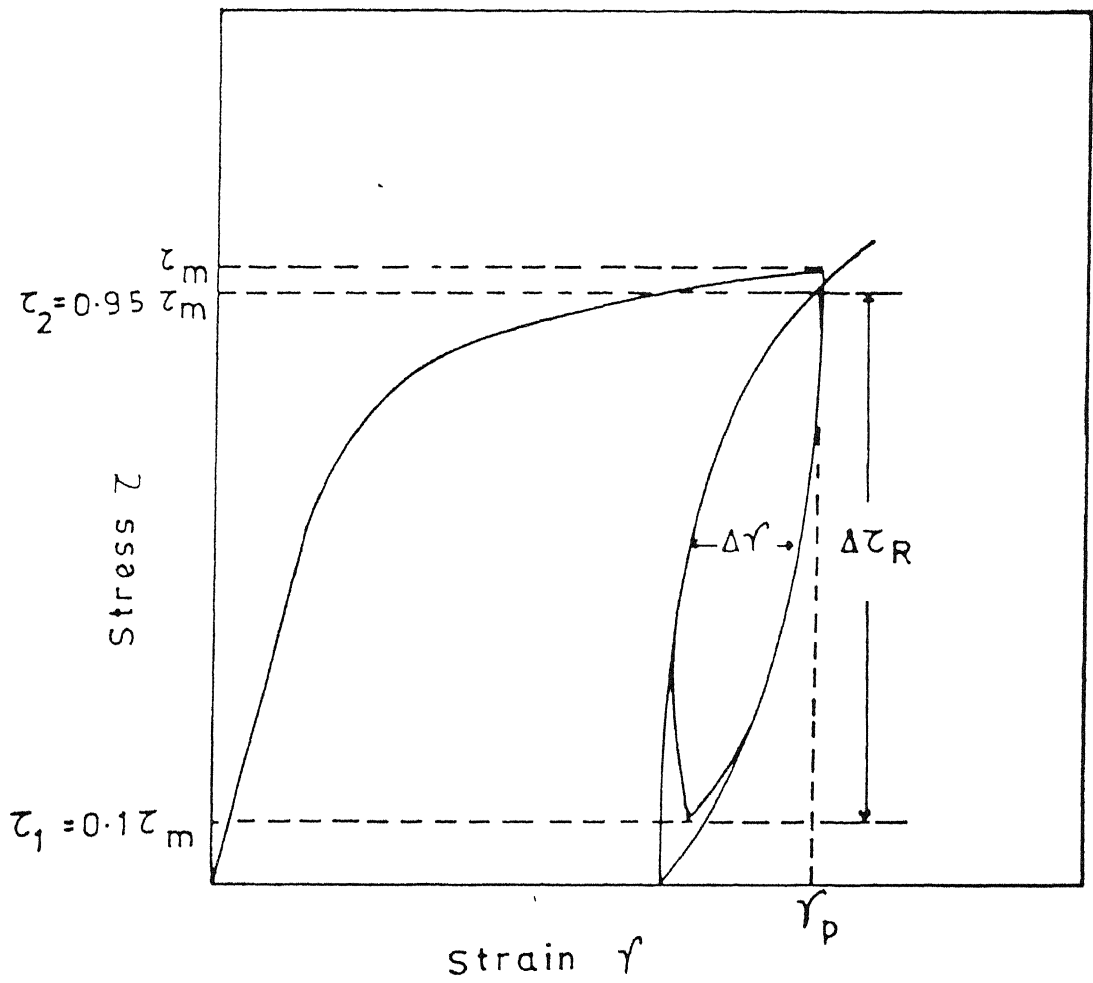


Fig. 2.10 Schematic sketch of load cycling with the load limits shown.

greater than 10^{-3} G, the τ_p contribution to energy absorption in cyclic deformation is neglected and the ΔE is taken to be equal to $2\tau_i \Delta\gamma$. Accordingly,

$$\Delta E = 2\tau_i \Delta\gamma \quad (2.64)$$

In utilising the experimentally obtained ΔE values obtained from direct tensile cyclic tests certain care is to be taken. The on-going equations derived here use shear stress and shear strains which are calculated from engineering stress-strain curves using resolution factors of 1/2 and 1/1.4 respectively [31]. This gives a multiplying factor of 1/2.8 to convert energy under the engineering stress-strain curves to that under shear stress-strain curves.

During load cycling though there is no macroscopic plastic deformation, dislocations which are pinned between two points move forward and backward giving rise to small anelastic strain as a result of dislocations not coming back to their original configurations owing to line tension effects and to the presence of internal stress fields [64]. This leads to the irreversible work done during stress cycling. The shear strain amplitude $\Delta\gamma$ can be taken as:

$$\Delta\gamma = \rho b d \quad (2.65)$$

where

ρ is the mobile dislocation density

b is Burgers vector and

d is the net distance moved by the dislocation after one full cycle.

From the theory of rate processes [65] the number of activations K/sec contributed by each of the thermally activated processes to the total anelastic deformation can be given by the expression:

$$K = \beta \left(\frac{kT}{h} \right) \exp - \left[\frac{U(\tau^*, T)}{kT} \right] \quad (2.66)$$

where

β is the transmission coefficient (< 1),

k is the Boltzmann constant ,

T is the absolute temperature,

h is Planck's constant and

$U(\tau^*, T)$ is the apparent activation energy which is a function of effective stress and temperature.

The dislocation velocity depends on its forward and backward jump frequencies. But during forward motion its backward jump probability is very small if the stresses are high and neglecting this term, the expression given by Krausz [66] for dislocation velocity v can then be written as:

$$v = \beta \cdot \frac{kT}{h} d^* \exp - \left[\frac{U(\tau^*, T)}{kT} \right] \quad (2.67)$$

where d^* is a characteristic relaxation distance. ' d^* ' cannot be identified as the activation distance or the distance over which dislocation moves during the forward cycle.

The distance d moved during activation can be related to dislocation velocity as:

$$d = v \tau_t \quad (2.68)$$

where τ_t is the relaxation time and is equal to the reciprocal of dislocation frequency ν .

From Eqs. 2.67 and 2.68 we can write

$$d = \nu \tau_t = \frac{\nu}{\nu} = \beta \cdot \frac{kT}{h} \left(\frac{d^*}{\nu} \right) \exp - \left[\frac{U(\tau^*, T)}{kT} \right] \quad (2.69)$$

Substituting this in Eq. 2.65, the shear strain amplitude,

$$\Delta \gamma = \beta \left(\frac{kT}{h\nu} \right) \rho b d^* \exp - \left[\frac{U(\tau^*, T)}{kT} \right] \quad (2.70)$$

From Eqs. 2.64 and 2.70, expression for the energy absorbed per cycle can be written as:

$$\Delta E = 2\tau_i \beta \left(\frac{kT}{h\nu} \right) (\rho b d^*) \exp - \left[\frac{U(\tau^*, T)}{kT} \right] \quad (2.71)$$

If V^* is the activation volume, then the energy absorbed in a single activation can be expressed as:

$$V^* \Delta E = 2\beta V^* \tau_i \left(\frac{\rho b d^*}{h\nu} \right) kT \exp - \left[\frac{U(\tau^*, T)}{kT} \right] \quad (2.72)$$

which on rearrangement gives:

$$\left(\frac{V^* \Delta E}{kT} \right) = 2\beta \left(\frac{V^* \tau_i}{h\nu} \right) (\rho b d^*) \exp - \left[\frac{U(\tau^*, T)}{kT} \right] \quad (2.73)$$

Many of the rate controlling mechanisms of plastic deformation have an apparent activation energy $U(\tau^*, T)$ which depends linearly on the effective stress τ^* :

$$U(\tau^*, T) = U_0 - V^* \tau^* \quad (2.20)$$

where U_0 is the activation energy without any stress assistance. The effective stress doing work during stress cycling is equal to stress range $\Delta\tau_R$ minus the internal stress τ_i . Accordingly,

$$U(\tau^*, T) = U_0 - V^*(\Delta\tau_R - \tau_i) \quad (2.74)$$

Using this in Eq. 2.73, it can be rewritten as:

$$\left(\frac{V^* \Delta E}{kT}\right) = 2\beta\left(\frac{V^* \tau_i}{h\nu}\right) (\rho b d^*) \exp - \left[\frac{U_0 - V^*(\Delta\tau_R - \tau_i)}{kT} \right] \quad (2.75)$$

Taking logarithm on both sides

$$\ln\left(\frac{V^* \Delta E}{kT}\right) = \ln\left(2\beta\left(\frac{V^* \tau_i}{h\nu}\right) (\rho b d^*)\right) - \frac{U_0 - V^*(\Delta\tau_R - \tau_i)}{kT} \quad (2.76)$$

The first term on the right side of the Eq. 2.76 can be treated relatively as a constant. This gives a linear plot when $\ln\left(\frac{V^* \Delta E}{kT}\right)$ is plotted against $(1/kT)$ with the slope equal to $U_0 - V^*(\Delta\tau_R - \tau_i)$.

Thus from the slope of $\ln\left(\frac{V^* \Delta E}{kT}\right)$ versus $1/kT$ it is possible to determine U_0 - the activation energy when no stress is applied. U_0 can nevertheless have a temperature dependence.

CHAPTER 3

EXPERIMENTAL PROCEDURE

3.1 Materials:

Experimental work was carried out on both the 9 Cr-1 Mo steel and 316 SS. The former was obtained from Indira Gandhi Centre for Atomic Research (IGCAR) Kalpakkam, as a forged thick section in the quenched and tempered condition. 316 SS was procured in the form of rods of diameter 16 mm in the cold worked and annealed condition. Chemical compositions of the two steels are given in Table 3.1.

Table 3.1: Chemical compositions of the two steels in wt. %

9 Cr-1 Mo steel*	C	Si	Mn	S	P	Cr	Mo	N
	0.09	0.75	0.67	0.0003	0.02	9.27	1.05	0.054
316 SS**	C	Ni	Cr	Mn	Si	P	S	Mo
	0.08 max.	10-14	16-18	2.0	1.0	0.045	0.036	2-3

* As given by IGCAR Kalpakkam

** Nominal composition [4].

9 Cr-1 Mo steel sections obtained were cut into small square sections of 11 mm x 11 mm and the length that was possible with the original section. 316 SS rods were swaged down to 11 mm diameter rods and then annealed at 750°C in Argon atmosphere for 2 hours. Test samples were machined out from these materials;

dimensions of the test specimen are given in Figure 3.1. The specimen surface was polished mechanically following machining.

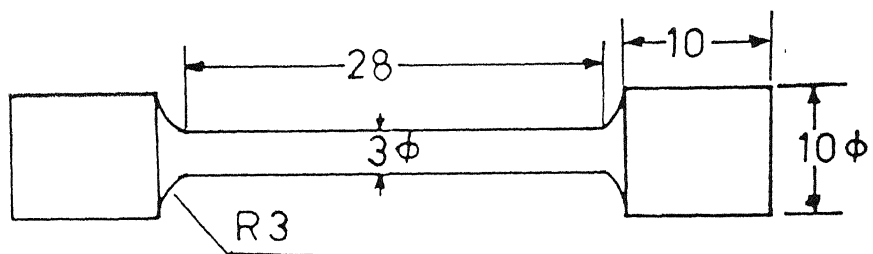
The microstructures of the materials are shown in Figure 3.2. The grain size of these materials was measured and it was in the range of 20-30 μ .

3.2 Mechanical Testing:

The specimens were tested in a floor model Instron Universal Testing Machine (Model No. 1195). The tests conducted were:

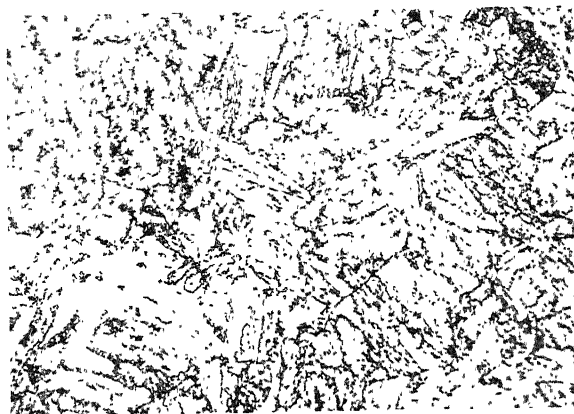
1. Constant strain rate tension tests.
2. Strain rate changing tests for the measurement of flow stress increments. Strain rate changes were made by instantaneously changing the box cross-head speed from a base strain rate $\dot{\epsilon}_1 = 2.99 \times 10^{-4}/\text{sec}$ to higher strain rate $\dot{\epsilon}_2 = 2.99 \times 10^{-3}/\text{sec}$. Only two strain rates were used.
3. Stress relaxation tests: Specimens were pulled at constant strain rate to a plastic strain ϵ_p and then machine was switched off to allow the load to relax.
4. Load cycling.
5. Load cycling with a creep hold at maximum load.

All the tests were conducted at the temperatures of 298K, 423K, 573K, 723K and 873K. High temperature tests were carried out using the high temperature grip assembly and enclosing the complete assembly in a cylindrical furnace. Temperature was controlled with the help of a temperature controller attachment to about $\pm 3\text{K}$. Temperature was continuously monitored by placing



All Dimensions in mms

Fig. 3.1 Dimensions of the test samples.



500 X



500 X

Fig. 3.2 Microstructures of (a) the 9 Cr-1 Mo steel and (b) 316 SS.

a chromel alumel thermocouple touching the gauge length zone of the specimen.

The thermocouple readings were noted down at regular intervals of 2 minutes with the help of a direct reading digital multimeter. At each temperature, the specimens were allowed to be soaked for 30 minutes before the commencement of testing.

Constant strain rate tests were conducted at a nominal strain rate of 2.99×10^{-4} /sec. For strain rate cycling tests a strain rate ratio of $\dot{\epsilon}_2/\dot{\epsilon}_1 = 10$ was used where $\dot{\epsilon}_1$ is base strain rate ($\dot{\epsilon}_1 = 2.99 \times 10^{-4}$ /sec) and $\dot{\epsilon}_2$ the new strain rate ($\dot{\epsilon}_2 = 2.99 \times 10^{-3}$ /sec). Very little amount of straining was allowed at the newer strain rate to avoid appreciable changes in micro-structure.

During the constant strain rate tests, 9 Cr-1 Mo steel showed serrated flow at 573K. So constant strain rate tests were conducted at different temperatures in the range of 523K to 673K. Tests were carried out in the strain rate ranges of 2.99×10^{-5} /sec to 1.19×10^{-3} /sec. Since no serrated flow was observed in the case of 316 SS, no further investigations were undertaken.

In stress relaxation tests, straining was done at a nominal strain rate of 2.99×10^{-4} /sec to a particular strain ϵ_p and corresponding load level. Then machine was switched off and load was recorded on a chart with constant speed. When no recognisable load drop was attained, the specimen was further strained at the basic strain rate to a higher strain and then again allowed to relax. The procedure was repeated. A schematic sketch of relaxation test is shown in Figure 3.3.

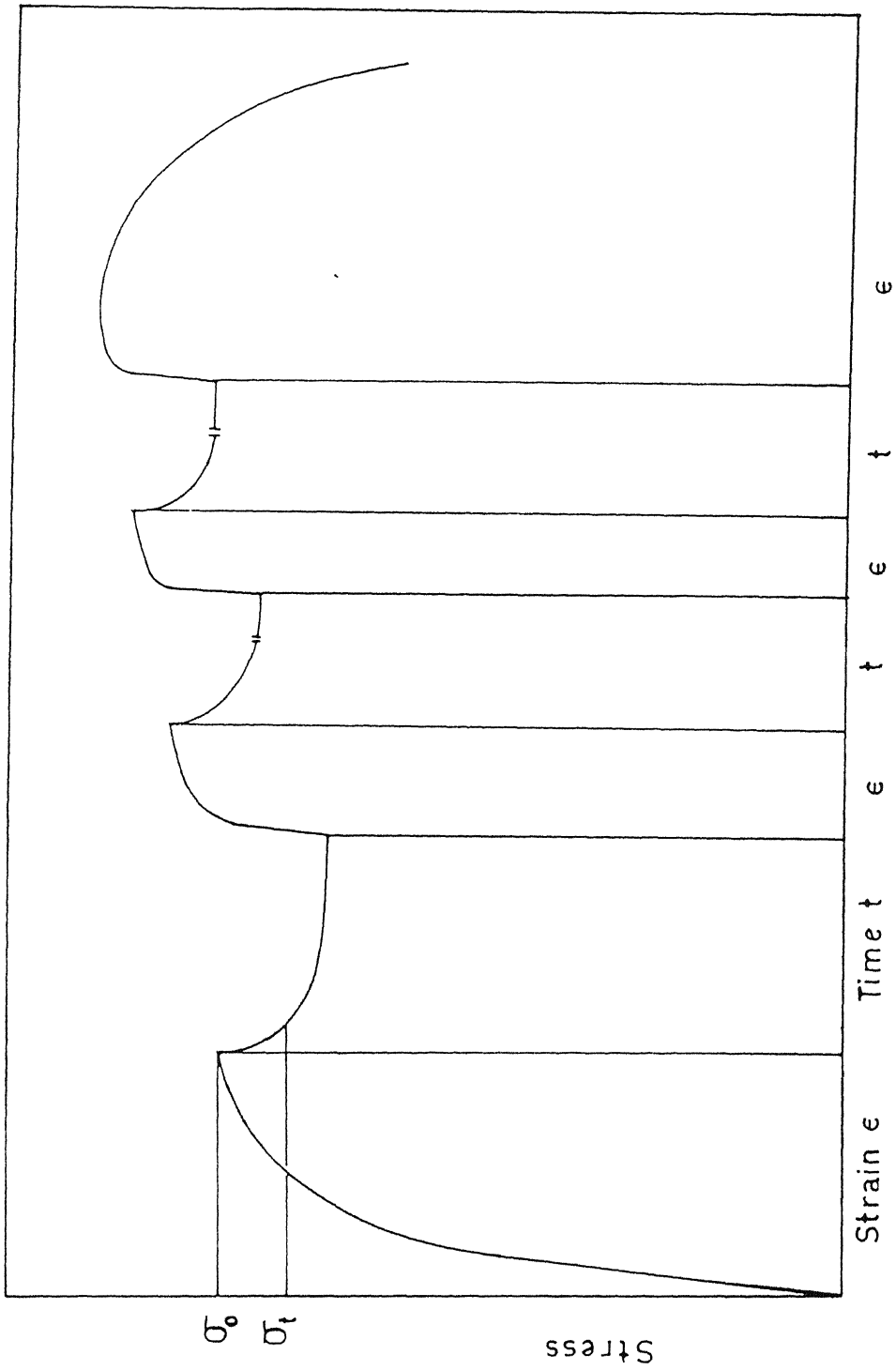


Fig. 3.3 Schematic sketch of stress relaxation test.

Load cycling tests were done under a constant nominal strain rate of 2.99×10^{-4} /sec. Initially the loading was done to a particular plastic strain ϵ_p and the corresponding flow stress σ_m , after which the specimens were unloaded. Load cycling was done between $\sigma_{\max} = 0.95 \sigma_m$ and $\sigma_{\min} = 0.1 \sigma_m$ for an arbitrary but fixed number of 70 cycles. Load versus elongation graphs were plotted at regular intervals. After 70 cycles, the specimens were unloaded and again loaded to a higher strain and corresponding stress. Load cycling was carried out taking the limits corresponding to the new flow stress, again for 70 cycles. The procedure was repeated at incremental plastic strain. Finally the specimens were pulled in tension. [Schematic sketch is shown in Figure 3.4a].

Load cycling with creep hold tests were also done in a similar manner. The difference was that samples were held at the maximum stress for one minute. The time of one minute was chosen from the stress relaxation tests where most of the relaxation was found to take place within this time. A schematic sketch of load cycling with creep hold is shown in Figure 3.4b.

Energy measurements were done from the load-elongation curves using a mechanical planimeter to find the area. The area was multiplied by a suitable multiplier depending upon the full scale load and chart and cross-head speeds.

For all the above tests, machine stiffness corrections were applied by conducting similar tests using much thicker samples.

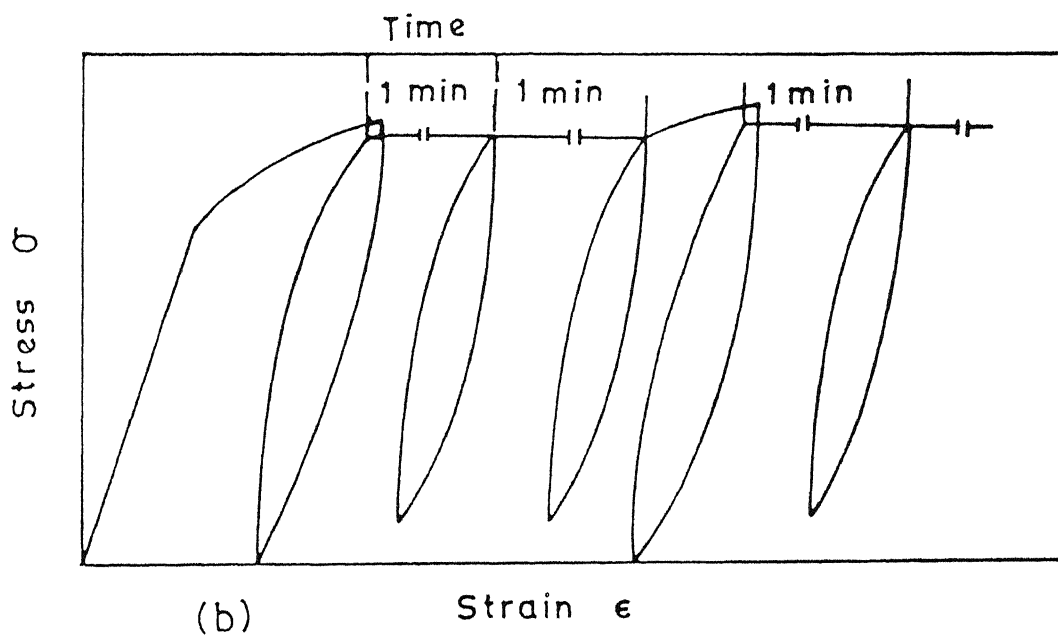
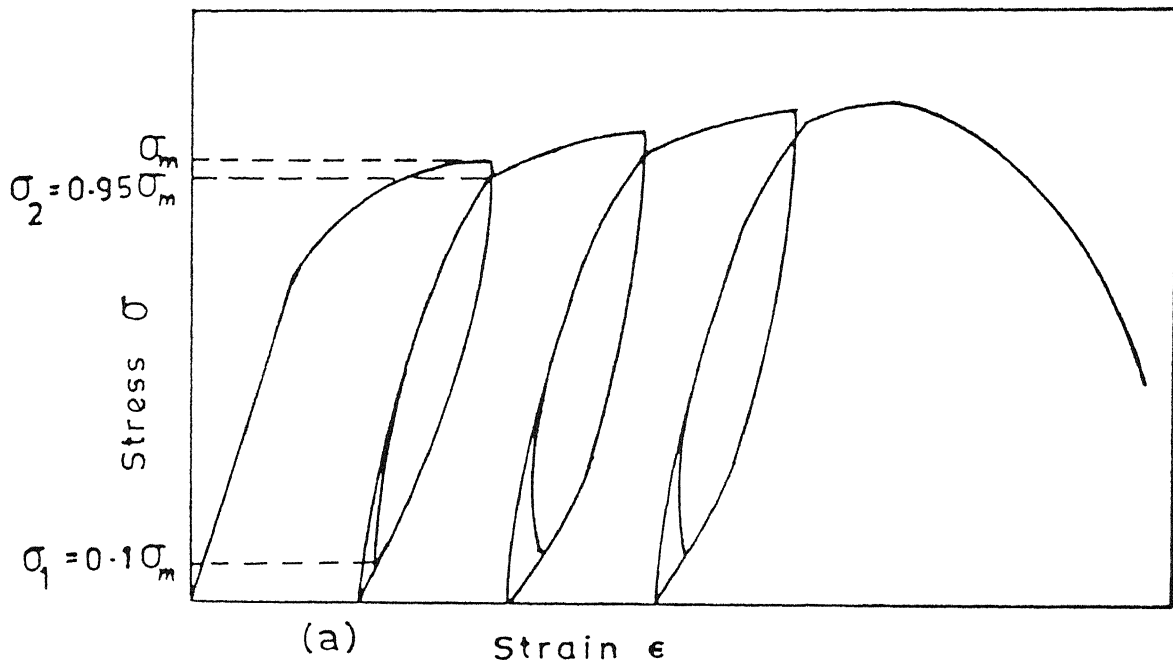


Fig. 3.4 Schematic sketch of load cycling (a) without creep holds and (b) with creep holds of one minute at maximum load.

CHAPTER 4

RESULTS AND DISCUSSIONS

4.1 General:

Typical engineering stress-strain curves obtained from constant strain rate tests are shown in Figures 4.1 and 4.2 for 9 Cr-1 Mo steel and 316 SS respectively. Ultimate tensile strength (UTS) and 0.4% proof stress (σ_y) were obtained from these plots. Shear modulus corrections were applied to these values. Ratio of flow stress at the temperature and that at the room temperature following the method of Basinski [67] is plotted as in Figure 4.3 along with the absolute values of UTS and σ_y . These values agree very well with the reported values [2, 4]. Serrated flow was observed in the case of 9 Cr-1 Mo steel at 573K (ref. Figure 4.1) but 316 SS did not show any noticeable serrated flow even though it is known to exhibit this behaviour with different combinations of temperature, strain rate and grain size [68, 39]. The σ_y and UTS plotted in Figure 4.3 show a flat region upto 723K and then dropdown [9 Cr-1 Mo steel] to about 50% at 873K.

4.2 Strain Rate Cycling:

Some selected true stress, true strain curves under strain rate cycling tests are given in Figures 4.4 and 4.5 for 9 Cr-1 Mo steel and 316 SS respectively. Shear stress and shear strain are obtained from the true stress and true strain using resolution factors of 1/2 and 1/1.4 respectively [31].

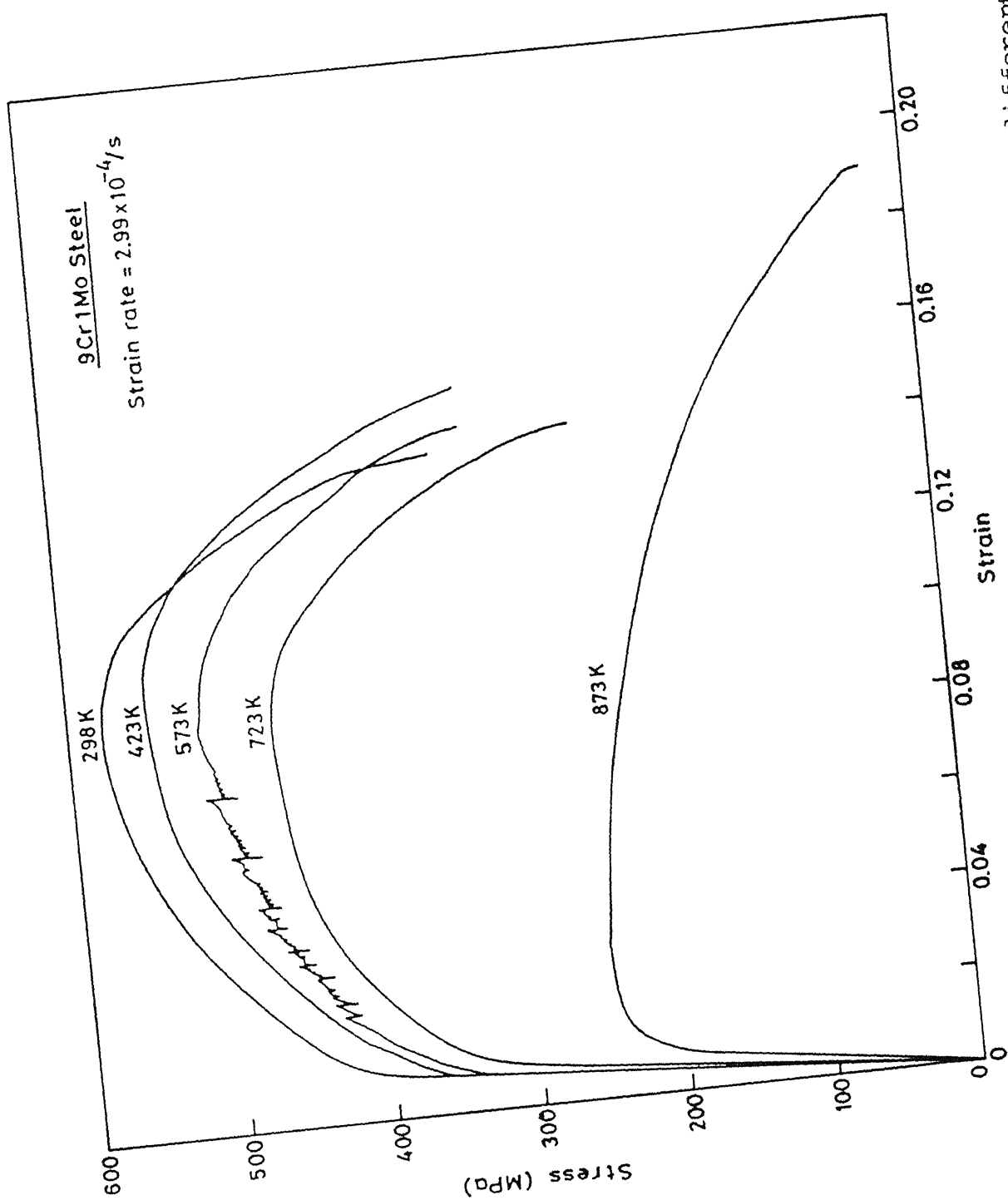


Fig. 4.1 Engineering stress-strain curves for the 9 Cr-1 Mo steel at different temperatures.

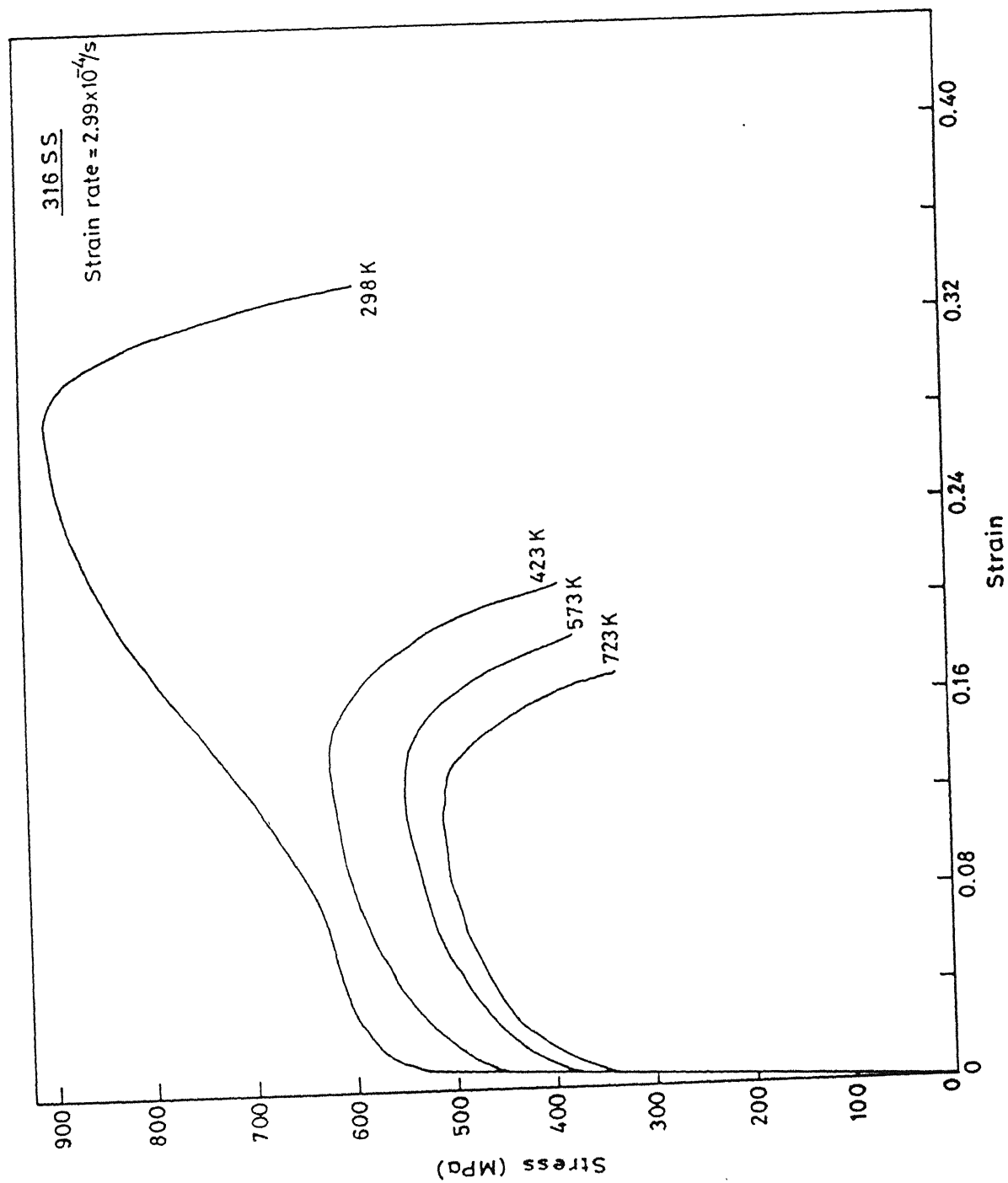


Fig. 4.2 Engineering stress-strain curves for the 316 SS at different temperatures.

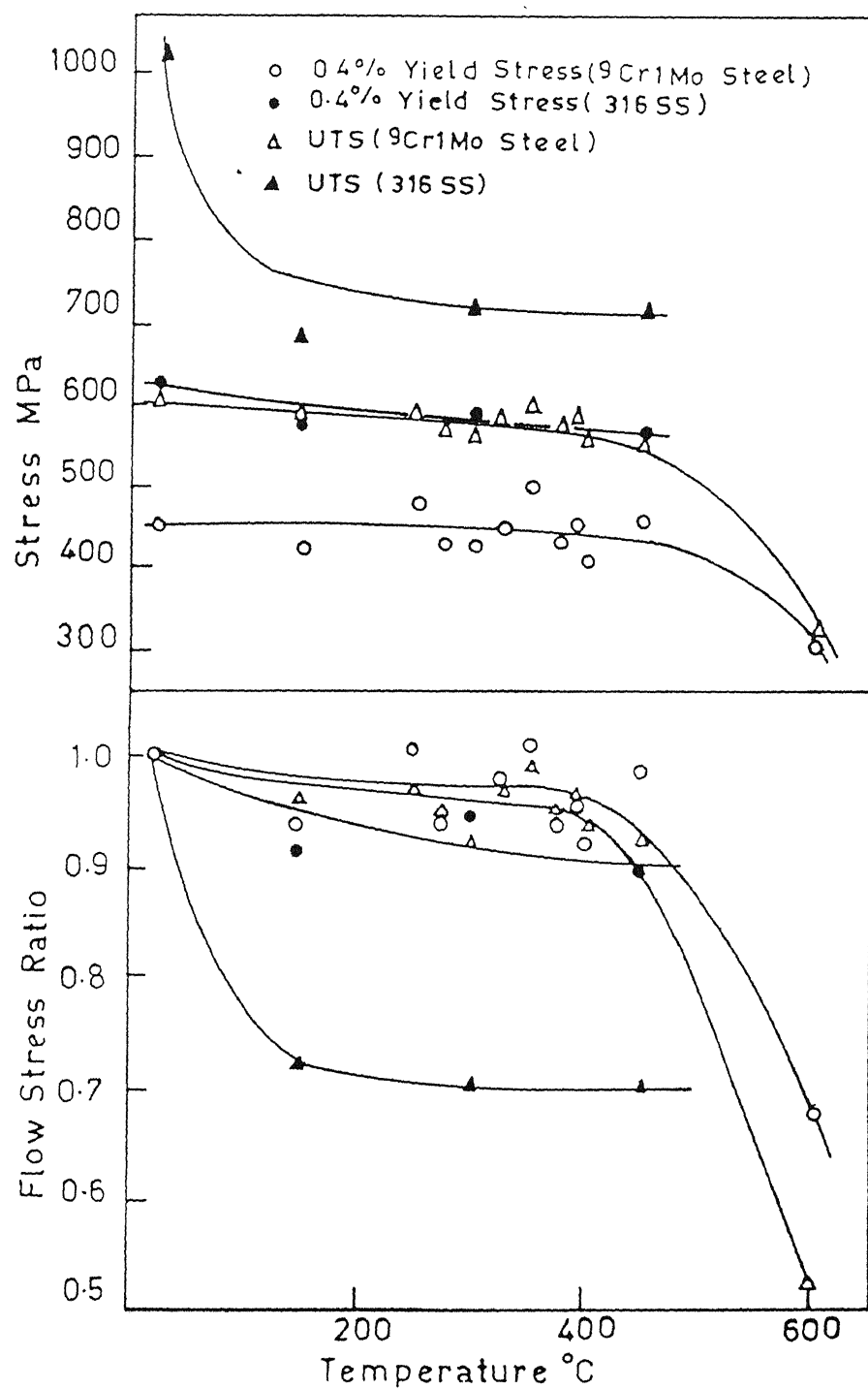


Fig. 4.3 Variation of the flow stress and flow stress ratio $(\sigma_T/E_T)/(\sigma_{298}/E_{298})$ at yield and UTS.

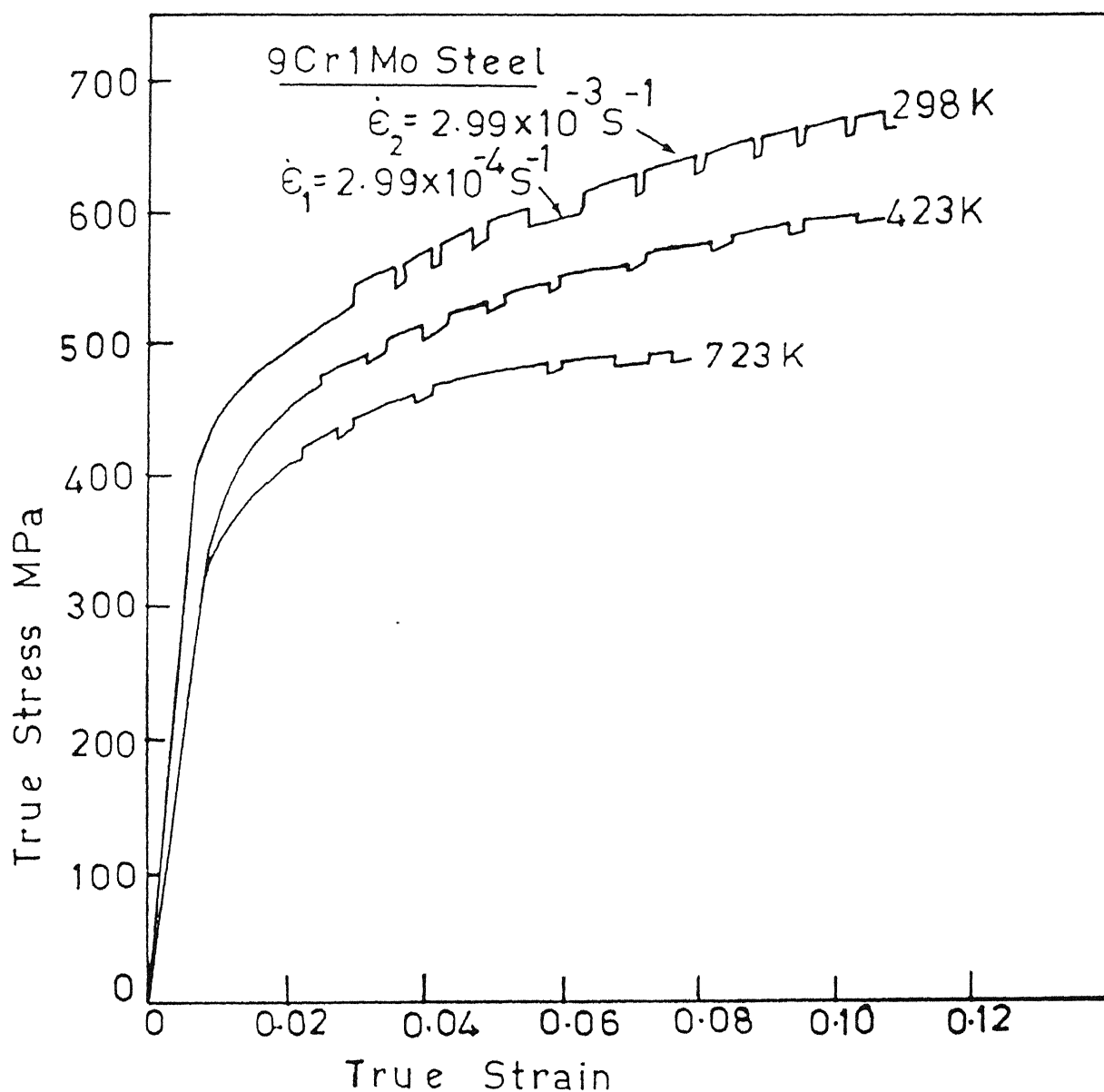


Fig. 4.4 Some selected strain rate cycling curves for the 9 Cr-1 Mo steel.
 Note: In all subsequent representations the resolved shear stress (τ) and shear strain (γ) are obtained from the corresponding tensile test data by using $\tau = \sigma/2$, $\gamma = \epsilon/1.4$.

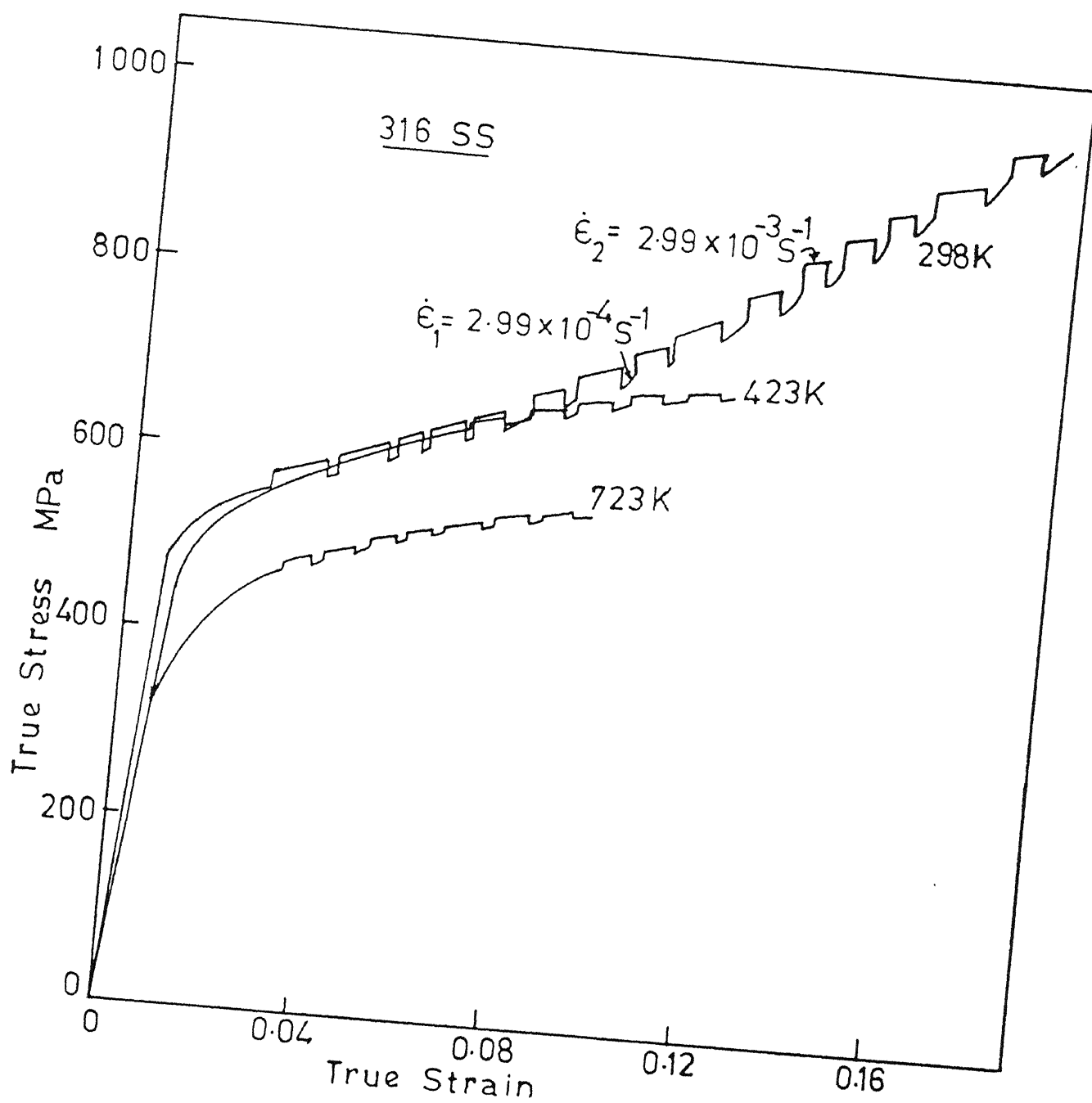


Fig. 4.5 Some selected strain rate cycling curves for the 316 SS.

4.2.1 Determination of m^* :

The inverse of strain rate sensitivity(m) at a particular strain is calculated from instantaneous strain rate change tests and using the relation:

$$m' = \frac{1}{m} = \left(\frac{\Delta \ln \dot{\gamma}}{\Delta \ln \tau} \right)_T = \left(\frac{\ln \dot{\gamma}_2 / \dot{\gamma}_1}{\ln \tau_2 / \tau_1} \right)_T \quad (4.1)$$

where τ_2 and τ_1 are the shear stress values at the two shear strain rates $\dot{\gamma}_2$ and $\dot{\gamma}_1$ respectively. The values of m' obtained in this manner at different strain levels are plotted against shear strain in Figures 4.6 and 4.7. The general increase in m' observed is consistent with the observations in iron single crystals by Michalak [32].

The value of m^* at any temperature is determined by extrapolating m' versus shear strain (γ) plot to zero strain according to Eq. 2.30. This procedure is repeated at any other temperature for both 9 Cr-1 Mo steel and 316 SS to obtain the values of velocity stress exponent m^* . The variation of m^* with temperature for both steels is given in Figure 4.8. A linear relationship is observed and no abnormality in the region of dynamic strain ageing was seen. The velocity stress exponent decreases with increase in temperature, in agreement with the reported behaviour (ref. Figure 2.9).

4.2.2 Stress components τ , τ_i and τ^* :

From the stress increment $\Delta\tau$ obtained under applied strain rate ratio $\dot{\gamma}_2/\dot{\gamma}_1$, effective stress τ^* and internal stress τ_i are determined at various temperatures employing the Eqs. 2.11 and

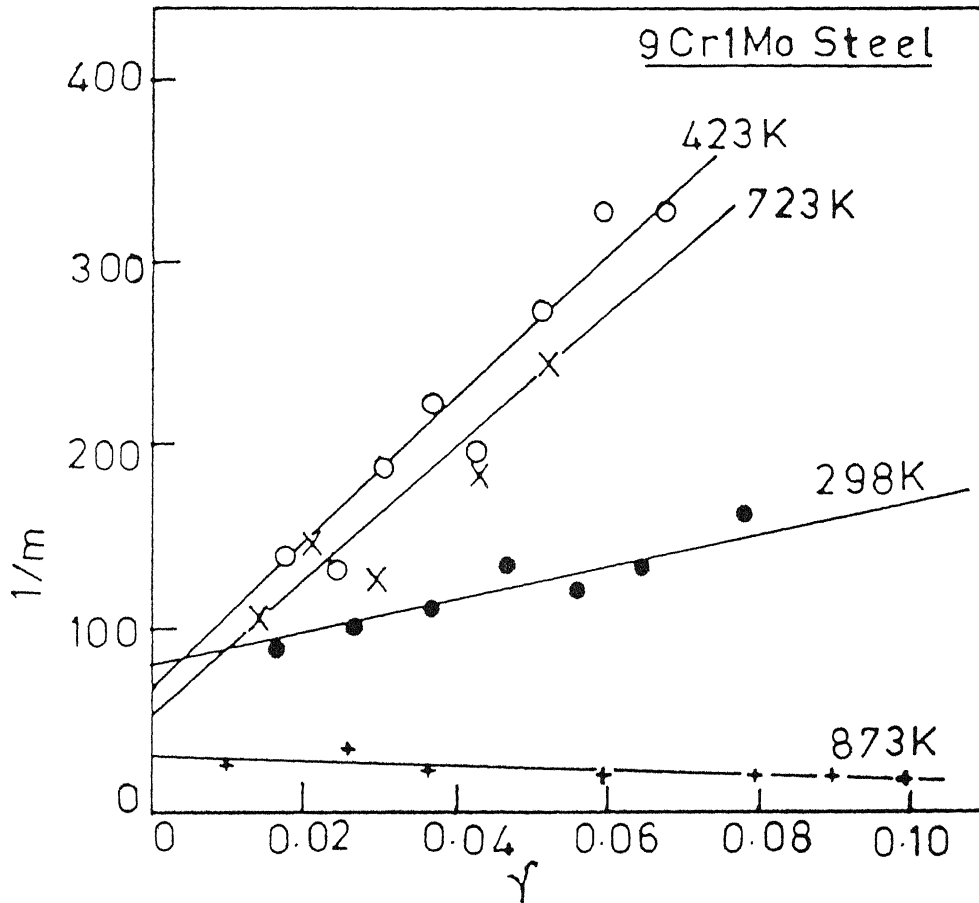


Fig. 4.6 Variation of reciprocal of strain rate sensitivity parameter, $m' (= 1/m = (\frac{\Delta \ln \dot{\gamma}}{\Delta \ln \tau}))$ at different temperatures for the 9 Cr-1 Mo steel.

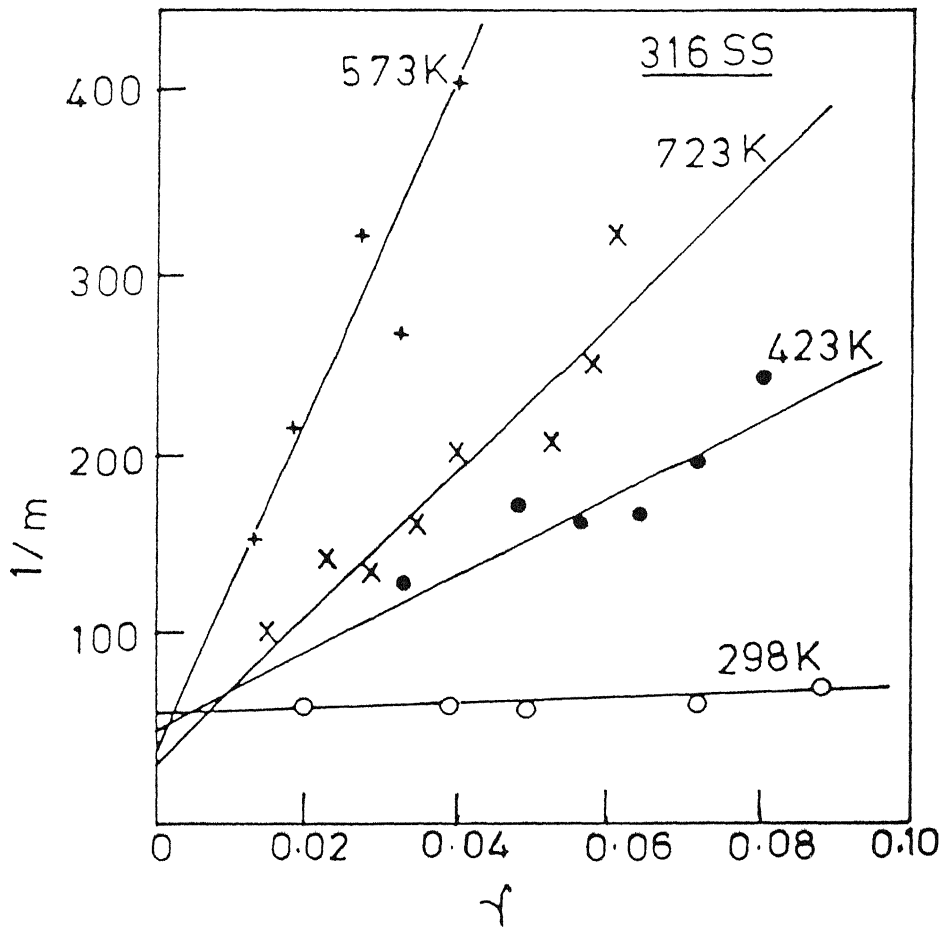


Fig. 4.7 Variation of reciprocal of strain rate sensitivity parameter, $m' (= 1/m = (\frac{\Delta \ln \dot{\gamma}}{\Delta \ln \tau}))$ at different temperatures for the 316 SS.

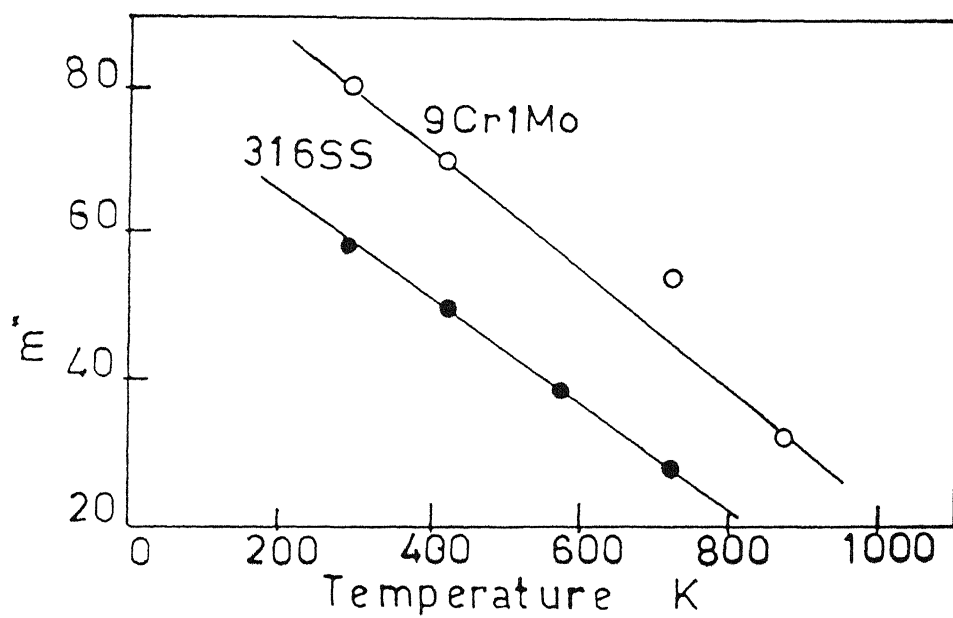


Fig. 4.8 Variation of velocity stress exponent m^* with temperature ($v = \text{const. } (\tau^*)^{m^*}$, τ^* = effective stress as in Fig. 4.9).

2.13. The τ_i values are found to be approximately equal to the flat region value of flow stress versus temperature curves in Figure 4.3. The calculated values of τ^* and τ_i are plotted against shear strain in Figures 4.9 and 4.10 for the two materials. The shear stress data in these figures correspond to the base strain rate (2.99×10^{-4} /sec).

The effective stress remains almost independent of strain as can be seen from Figures 4.9 and 4.10. This shows that there is no appreciable change in the density of mobile dislocations with increasing the strain rate. With the increase in temperature, τ^* is observed to decrease in support of the theory of thermal activation.

The Figures 4.9 and 4.10 show that the internal stress increases with strain. The increase in internal stress is due to the increase in density of dislocations. The ratio α between the internal stress and the applied stress is plotted against shear strain at different temperatures in Figure 4.11. The increase in internal stress with strain is clearly manifested in these plots.

A negative internal stress is obtained for 9 Cr-1 Mo steel at 873K. At this temperature 9 Cr-1 Mo steel reaches ultimate tensile strength (UTS) at a very low strain and UTS and 0.4% proof stress (σ_y) are comparable. Furthermore, there is a drastic reduction in strength at this temperature resulting in easy flow of material once the yield point is reached. The steel has a tempered martensitic structure, and there might be considerable alterations in the microstructure resulting in a negative internal stress at higher temperatures.

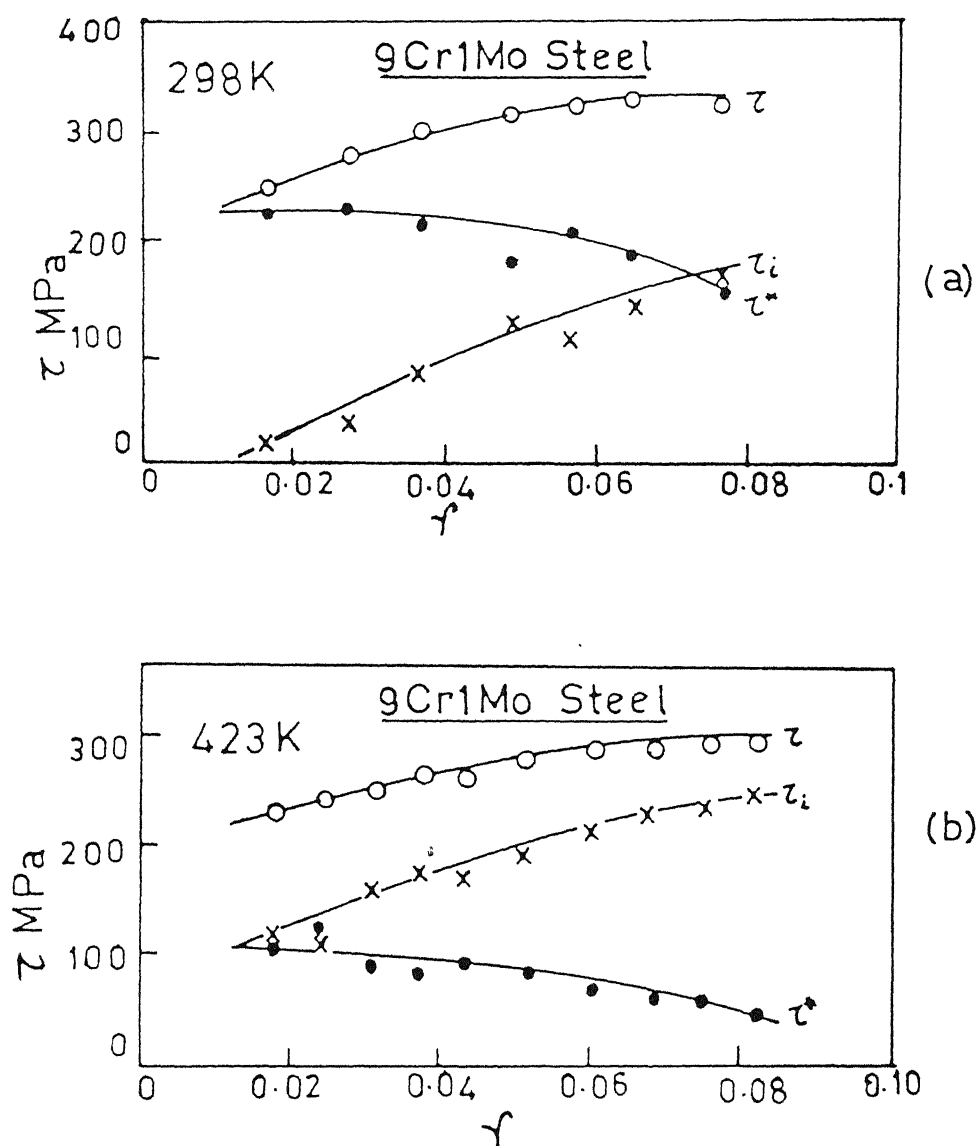
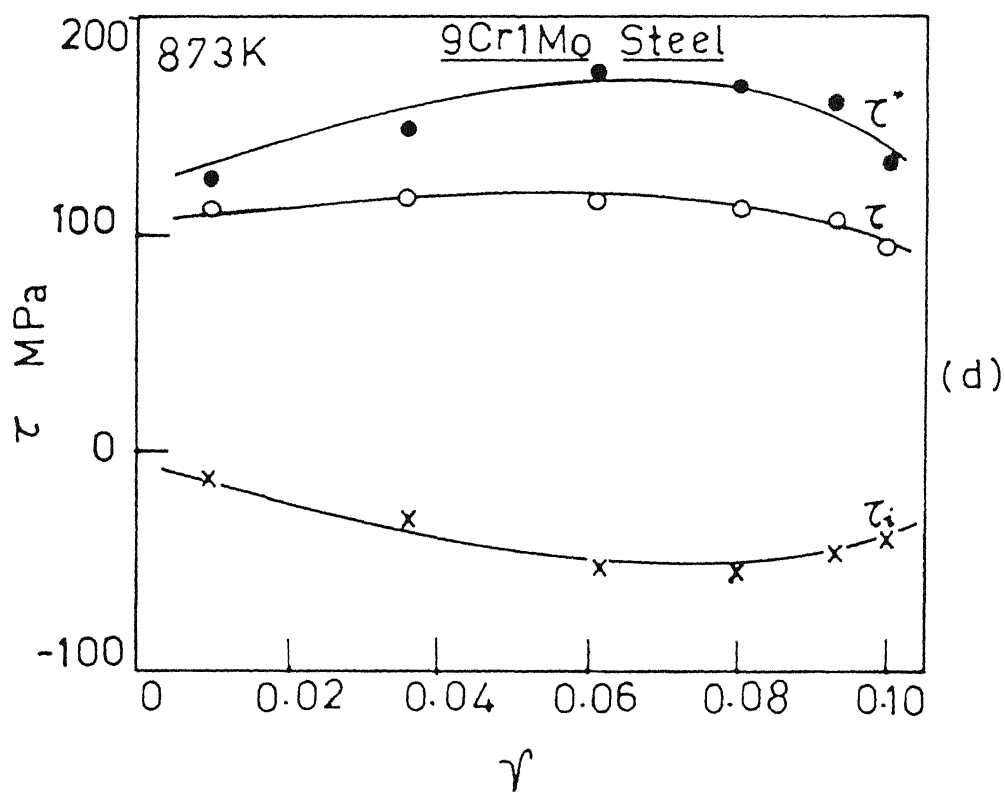
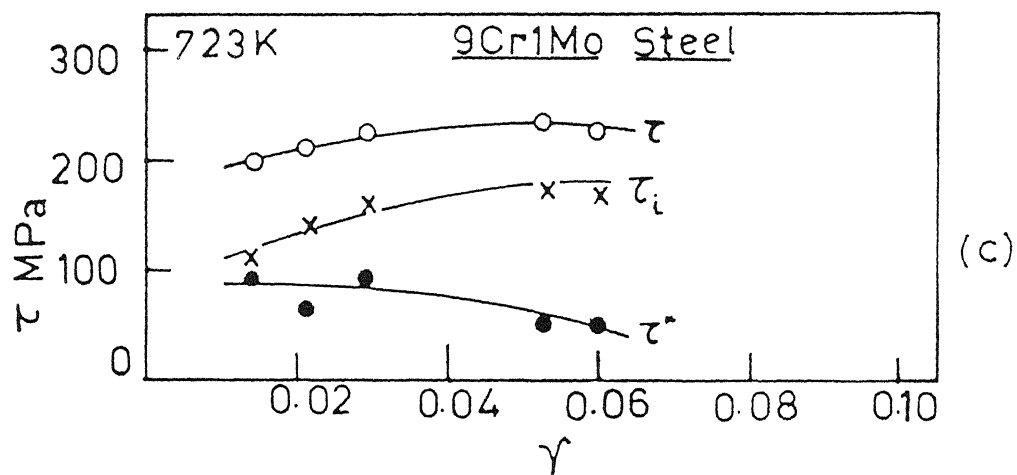


Fig. 4.9 Variation of shear stresses τ , τ^* and τ_i for the 9 Cr-1 Mo steel at (a) 298K (b) 423K (c) 723K and (d) 873 K (τ^* = effective stress, $\tau_i = \tau - \tau^*$ is the internal stress).



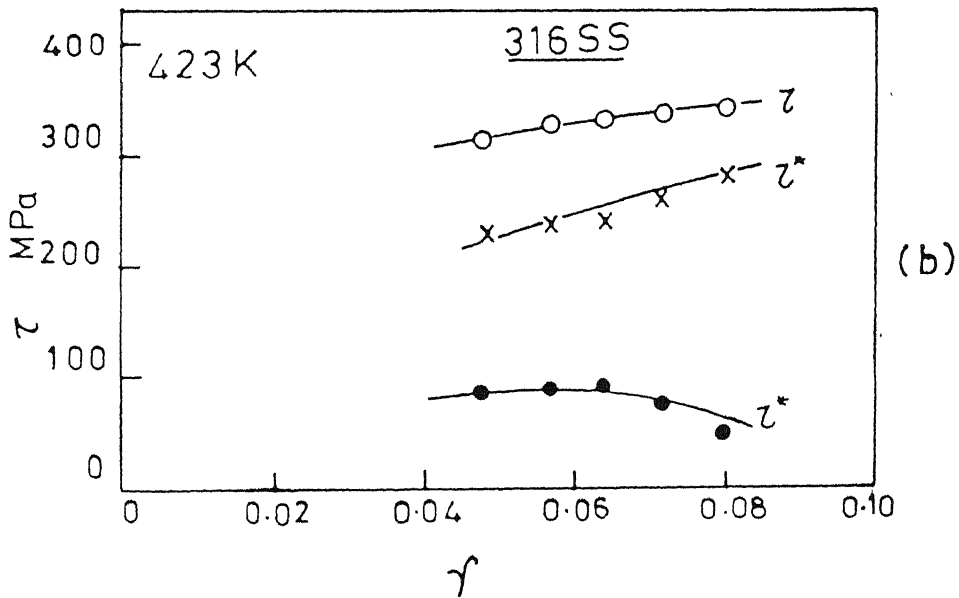
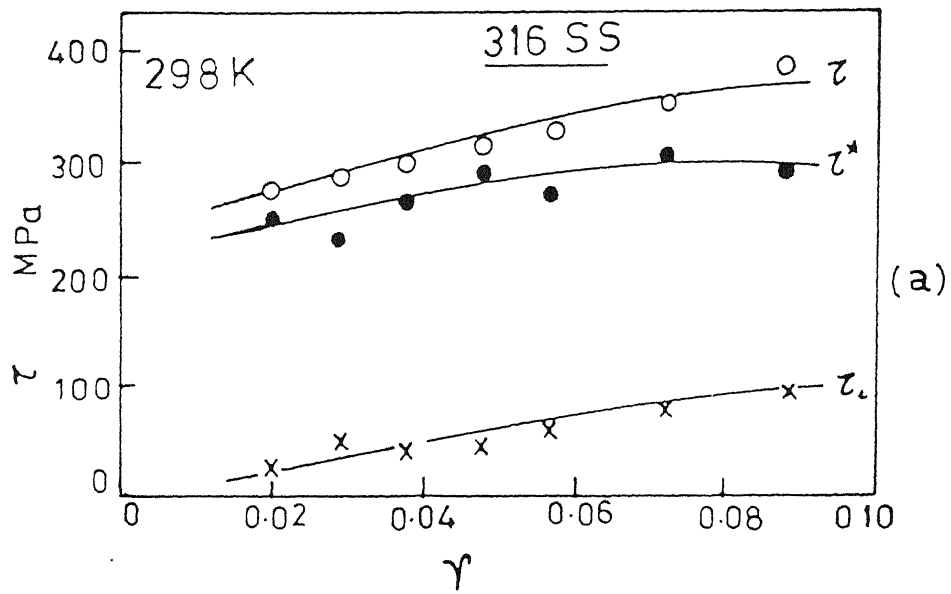
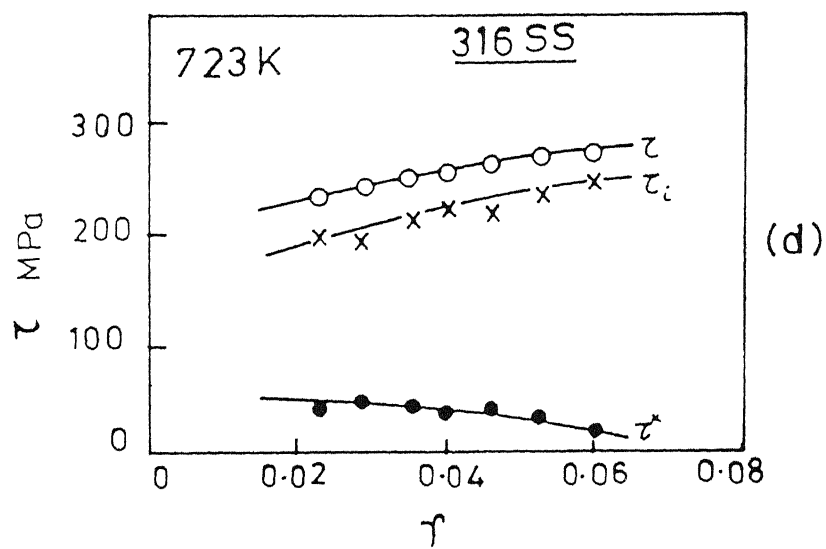
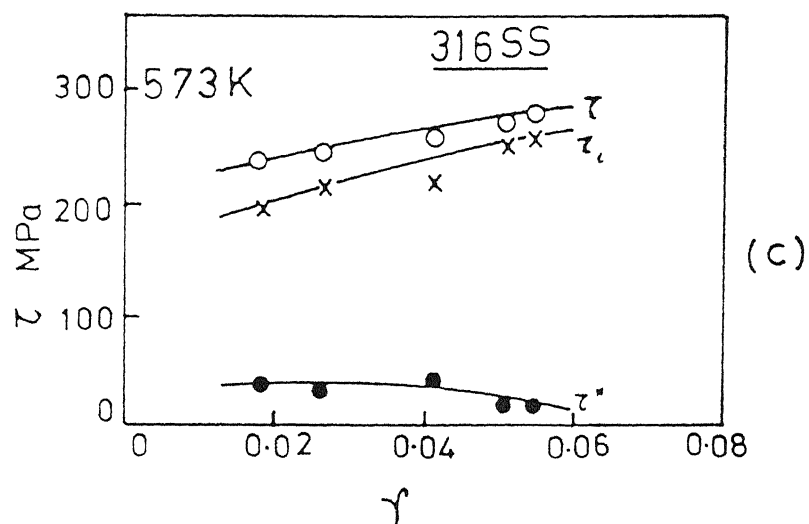


Fig. 4.10 Variation of shear stresses τ , τ^* and τ_i for the 316 SS at (a) 298K, (b) 423K, (c) 573K and (d) 723K.



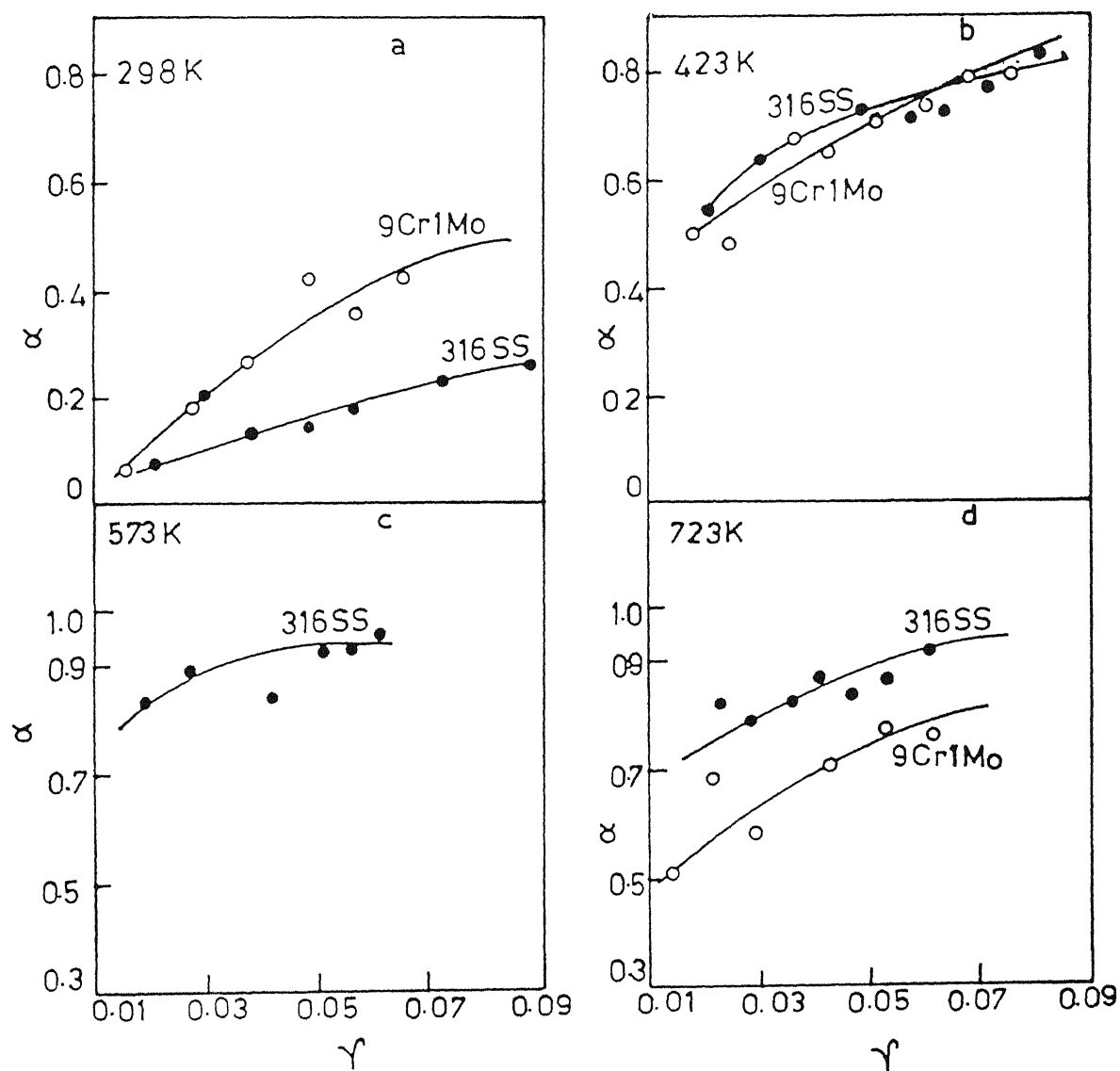


Fig. 4.11 Variation of the ratio of internal stress to the applied stress, α with shear strain at (a) 298K, (b) 423K, (c) 573K and (d) 723K.

4.2.3 Activation parameters:

The evaluation of activation volume using the strain rate change tests is done according to the Eq. 2.22a

$$V^* = kT \left(\frac{\ln \dot{\gamma}_2 / \dot{\gamma}_1}{\Delta \tau} \right)_{T, \gamma} \quad (2.22a)$$

Activation volume obtained is plotted against the effective stress at different temperatures as in Figure 4.12. The parabolic curves obtained by least square fit are extended on both sides for better comparison. The parabolic relation obtained is in agreement with the reported behaviour [31, 54]. Activation volume ranged between 90 b^3 and 600 b^3 for 9 Cr-1 Mo steel and 50 b^3 to 800 b^3 for 316 SS.

At a particular strain, the value of $V^* \tau^*$ is calculated using the experimentally determined V^* and τ^* values. This is repeated at other strains and an average $V^* \tau^*$ value is obtained. Similarly $V^* \tau^*$ values at other temperatures are also obtained. Determination of the activation energy is done according to Eq. 2.33. A plot of $\frac{V^* \tau^*}{kT}$ versus $1/kT$ as in Figure 4.13 should yield a straight line, for a single activation process. The activation energy values obtained as the slope of these straight lines for 9 Cr-1Mo steel and 316 SS are $4.8 \times 10^{-19} \text{ J}$ (2.99 eV) and $3.6 \times 10^{-19} \text{ J}$ (2.25 eV) respectively. The intercepts had small negative values of -9 and -13 for $\ln(\dot{\gamma}/\dot{\gamma}_0)$ giving the thermal component of activation energy $U(\tau^*, T) = -kT \ln \dot{\gamma}/\dot{\gamma}_0$ at any temperature to be about 9 kT and 13 kT for 9 Cr-1 Mo steel and 316 SS respectively.

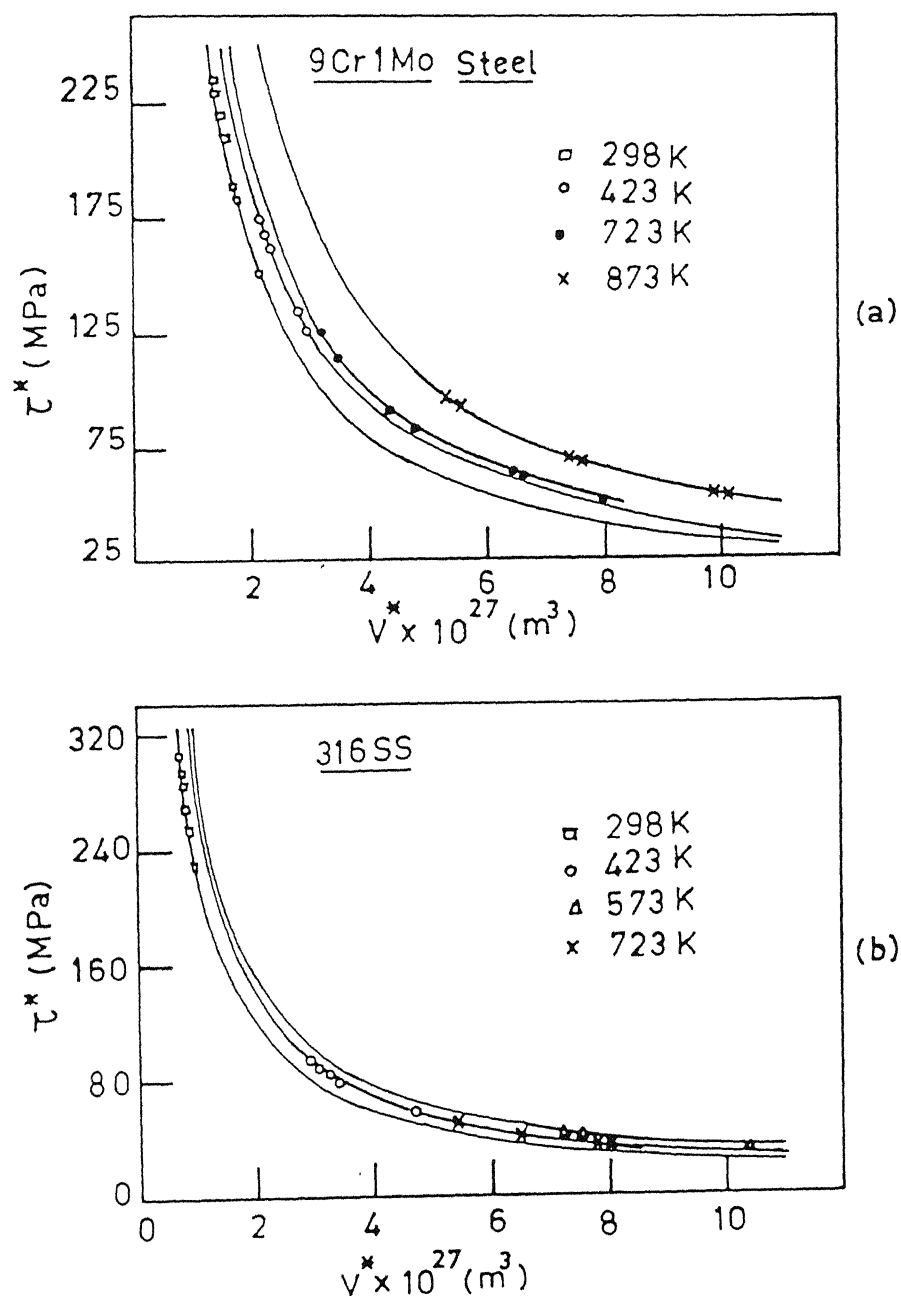


Fig. 4.12 Activation volume V^* versus effective stress τ^* for (a) 9 Cr-1 Mo steel and (b) 316 SS.
 Note: Thick lines with points marked show the experimental regime. $V^*\tau^* = \text{constant}$, or $\tau^* = \text{constant}/V^*$.

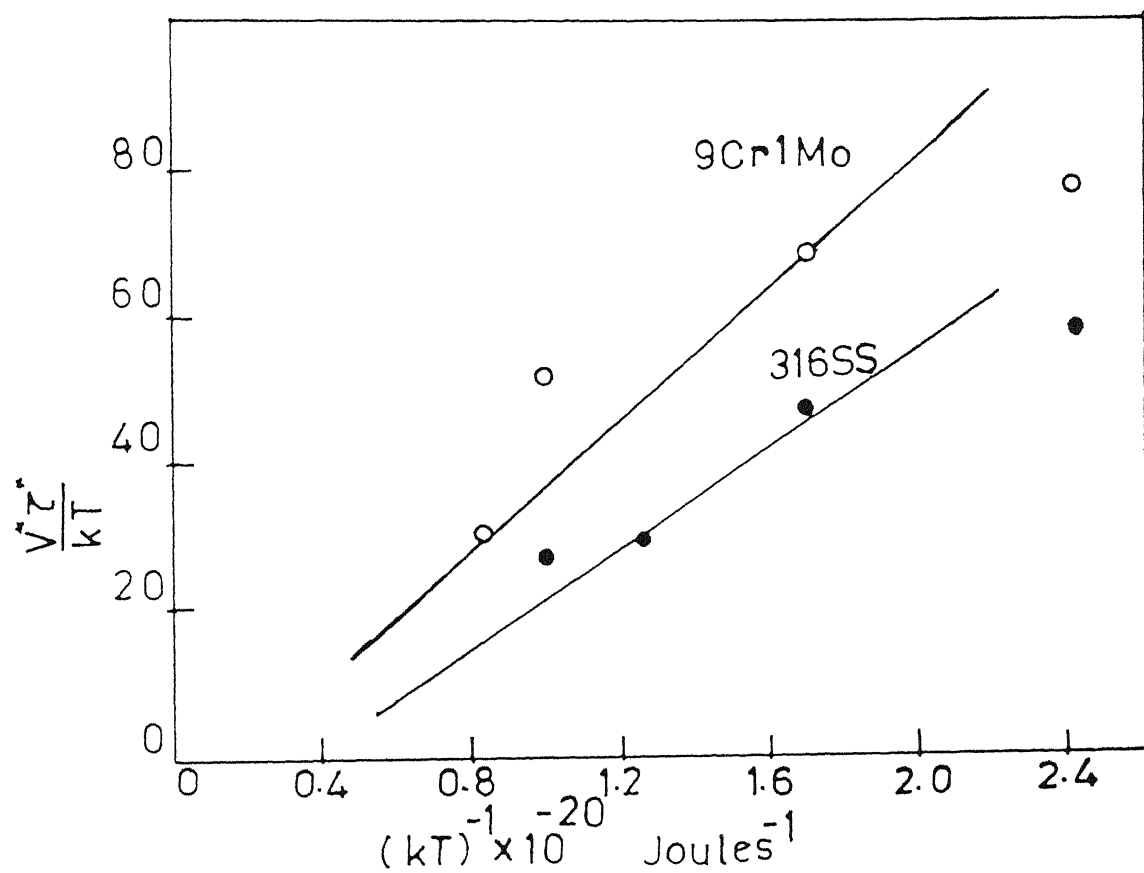


Fig. 4.13 $\frac{V^*\tau^*}{kT}$ versus $\frac{1}{kT}$ for determination of activation energy U_0 $\left[\frac{V^*\tau^*}{kT} = \frac{U_0}{kT} + \ln \frac{\dot{\gamma}}{\dot{\gamma}_0} \right]$.

An estimation of the dislocation frequency can be made using the intercepts $\ln \dot{\gamma}/\dot{\gamma}_0$ for the two materials. We have for 9 Cr-1 Mo steel

$$\ln \dot{\gamma}/\dot{\gamma}_0 = \ln \dot{\gamma}/NAb\nu = -9$$

$$\nu = \frac{\dot{\gamma} \exp(9)}{NAb}$$

Taking:

$$N = 10^{15}/\text{m}^3 \text{ (determined later from toughness measurement)}$$

$$A = 50 b^2$$

$$b = 2.5 \times 10^{-10} \text{ m and}$$

$$\dot{\gamma} = 2.99 \times 10^{-4}/\text{sec.}$$

$$\nu = \frac{2.99 \times 10^{-4} \times \exp(9)}{10^{15} \times 50(2.5 \times 10^{-10})^2(2.5 \times 10^{-10})} \simeq 10^{12}$$

Similarly for 316 SS ν is found to vary in the range of $10^{12} - 10^{13}$. This is consistent with the generally accepted dislocation vibration frequency of 10^{-1} to 10^{-2} times the atomic vibration frequency of 10^{13} .

Extensive literature [69] is available on dislocation mechanisms for thermally activated deformation in pure metal single crystals and alloys including a variety of steels. In fact in single crystals the identification of the rate controlling mechanism is rather easy. In materials like the 9 Cr-1 Mo steel and 316 SS which have different precipitate particles and large number of grains, the activation process may not be simple. A spectrum of obstacles may have to be overcome by the dislocation and hence an identification of a rate controlling process is difficult.

With the activation parameters observed in the present work and in view of the fact that in individual grains at least 2-3 slip systems are operating, a potential mechanism to consider would be the intersection of two dislocations. This is one of the most extensively investigated mechanisms in pure metals and alloys, both as a thermally activated mechanism and also as a source of work hardening. Intersection leads to the formation of jogs and kinks on dislocations. Majumdar and Shetty [70] have estimated the activation energy for the intersection of two dislocations leading to the formation of two jogs. Considering two extended dislocations the activation energy was calculated as the sum of energy of formation of two jogs, energy of constriction, corners and an additional short range interaction between one jog and the other dislocation that builds up during intersection. The activation energy is estimated to be about 4.518×10^{-19} J (2.82 eV). The activation energy values obtained in the present work - 4.8×10^{-19} J (2.99 eV) and 3.6×10^{-19} J (2.25 eV) respectively for 9 Cr-1 Mo steel and for the 316 SS - can be completely accounted for, if dislocation intersection is taken as the rate controlling process. The activation volumes are also in good agreement with such a mechanism.

Assuming that square kinks are formed on the intersecting dislocations along the line of approach, an average activation distance \bar{d} can be estimated from the activation volume using the relations $V^* = A^*b$ and $\bar{d} = \sqrt{A^*}$. The value of \bar{d} ranges between 10 b to 25 b for the 9 Cr-1 Mo steel and 5 b to 30 b for 316 SS. A plot of (τ^*/G) versus \bar{d}/b is shown in Figure 4.14. A least

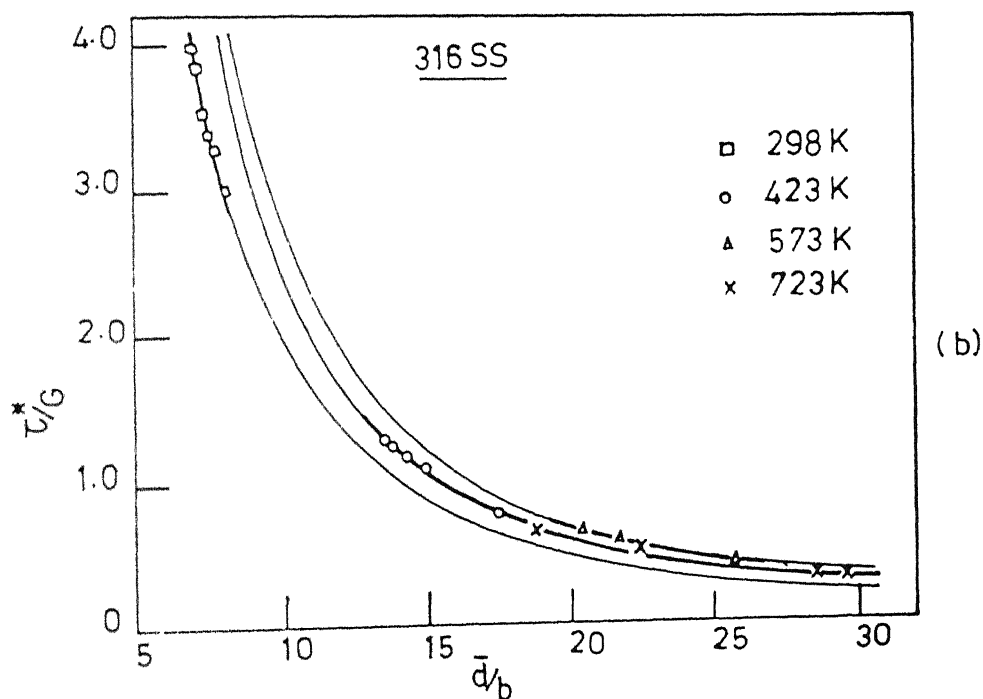
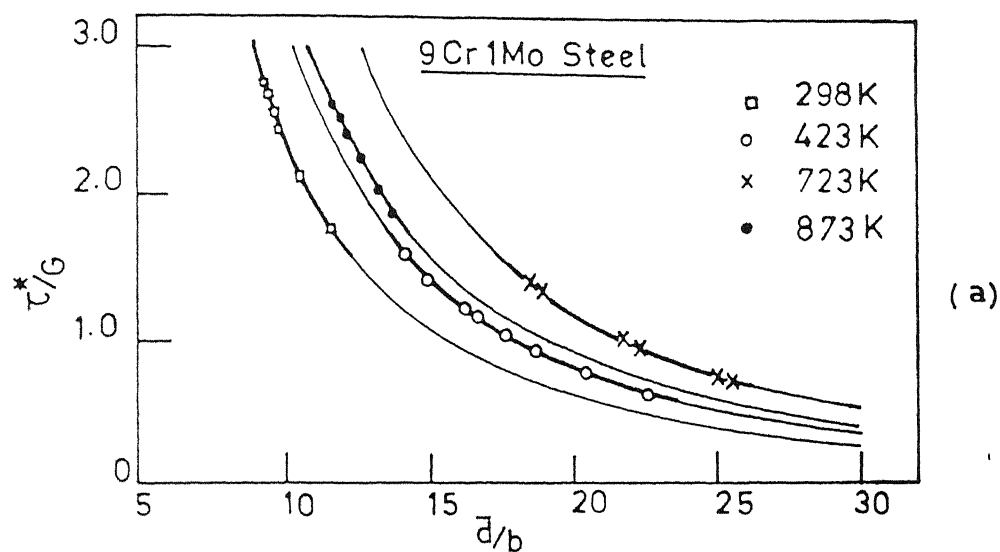


Fig. 4.14 Normalised effective stress versus \bar{d}/b plot at different temperatures for (a) 9 Cr-1 Mo steel and (b) 316 SS. [$\bar{d} = (\text{Activation area})^{1/2}$].

square fit gives a relationship of $\tau^* \propto d^{-1/2}$, contrary to an expected hyperbolic force-distance curve for infinite dislocations. With $\tau^* \propto d^{-n}$ the value of $n = 0.5$ lies in the range of $0.8 \geq n \geq 0.08$, determined by Shetty and Hirth [71] using an approximate shape and exact energy method for two intersecting dislocations and the theory of infinitesimal dislocations. This reaffirms the intersection of dislocations as the rate controlling process.

4.3 Dynamic Strain Ageing:

Serrated flow was observed in the 9 Cr-1 Mo steel in the range of 523K to 673K in the nominal strain rate test as shown in Figure 4.15. Effect of strain rate on the stress-strain curve is shown in Figures 4.16, 4.17 and 4.18 at the temperatures 523K, 573K and 648K respectively for the strain rates ranging from 2.99×10^{-5} /sec to 1.19×10^{-3} /sec.

From these stress-strain curves critical strain values for the onset of serrated flow were obtained. Variations of $\ln \dot{\epsilon}$ with $\ln \epsilon_c$ and $\ln \epsilon_c$ with $1/T$ are shown in Figures 4.19 and 4.20 respectively. From these plots we get $m_1 + \beta = 2.3, 3.1$ and -3.3 as the slopes of $\ln \dot{\epsilon}$ versus $\ln \epsilon_c$ plot at 523K, 573K and 648K respectively. The plot of $\ln \epsilon_c$ versus $1/T$ at a constant strain rate gives a series of parallel straight lines corresponding to different strain rates. The plot shows a reversal at higher temperatures but the magnitude of the slope remains unchanged. The slope of the plots give $[Q_m/k(m_1+\beta)] = 3.1 \times 10^3$ at temperatures less than 580K and -3.1×10^3 above 580K. From these experimentally obtained values, activation energy for the

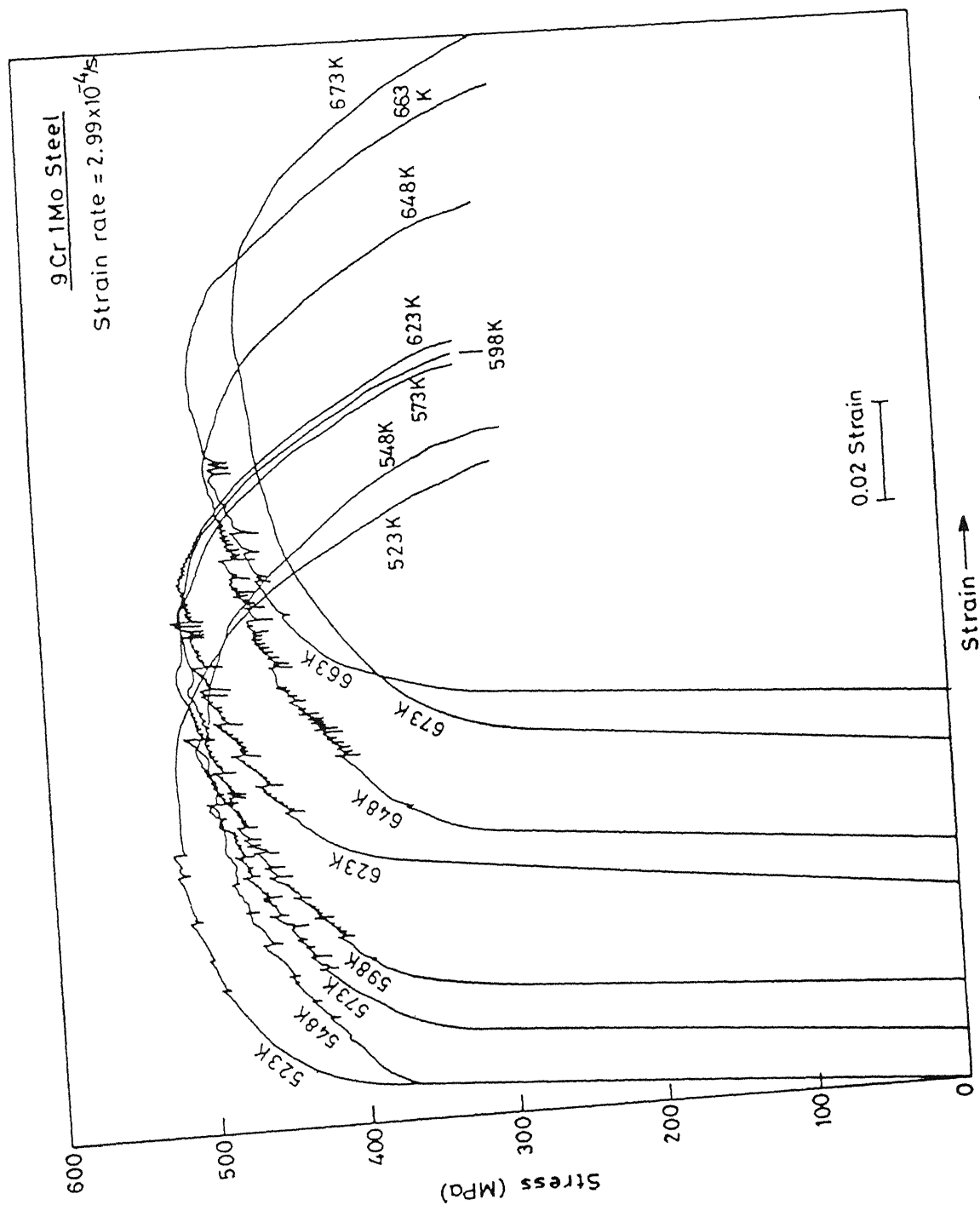


Fig. 4.15 Engineering stress-strain curves for the 9 Cr-1 Mo steel in the dynamic strain ageing (DSA) regime.

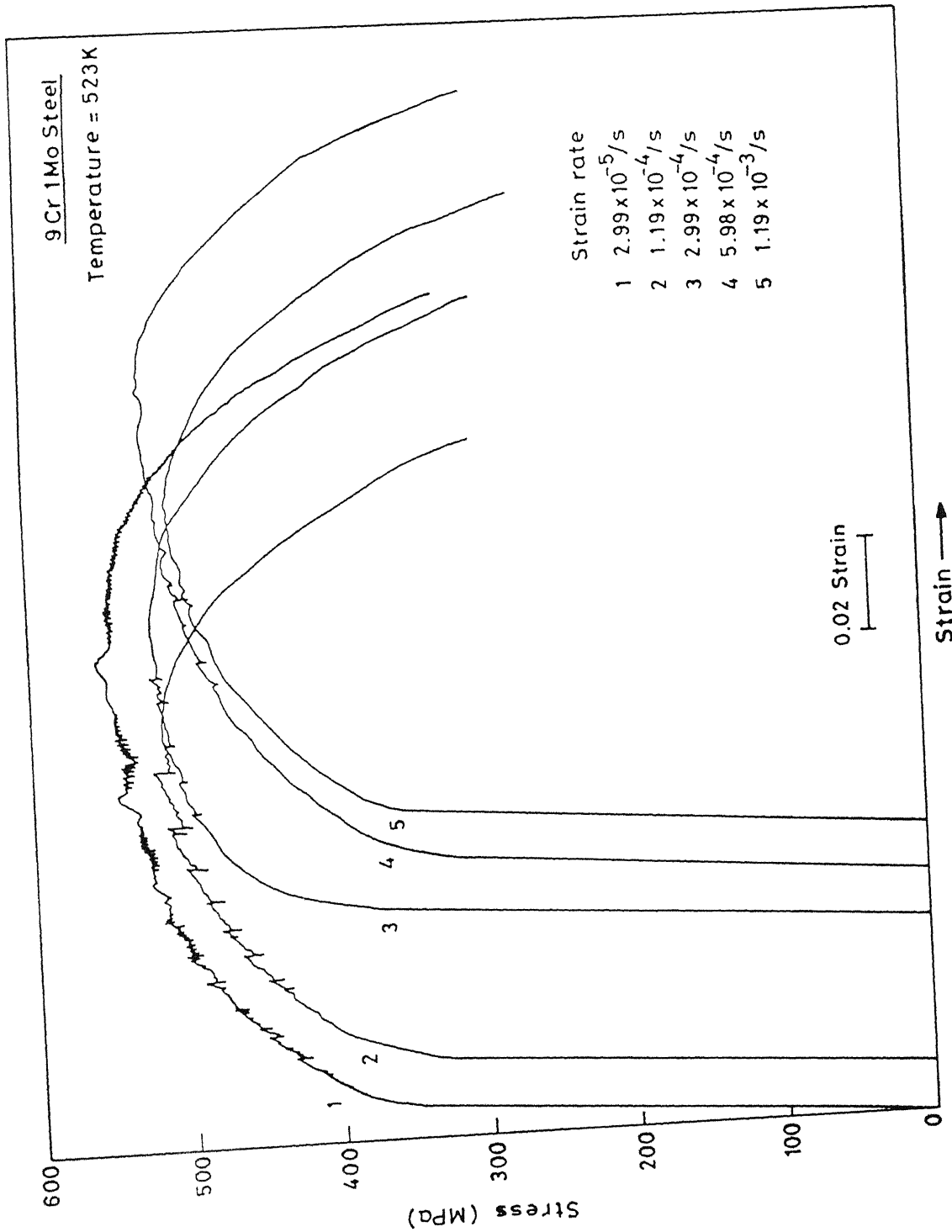


Fig. 4.16 Appearance of serrations (DSA) at 523K at different strain rates for 9 Cr-1 Mo steel.

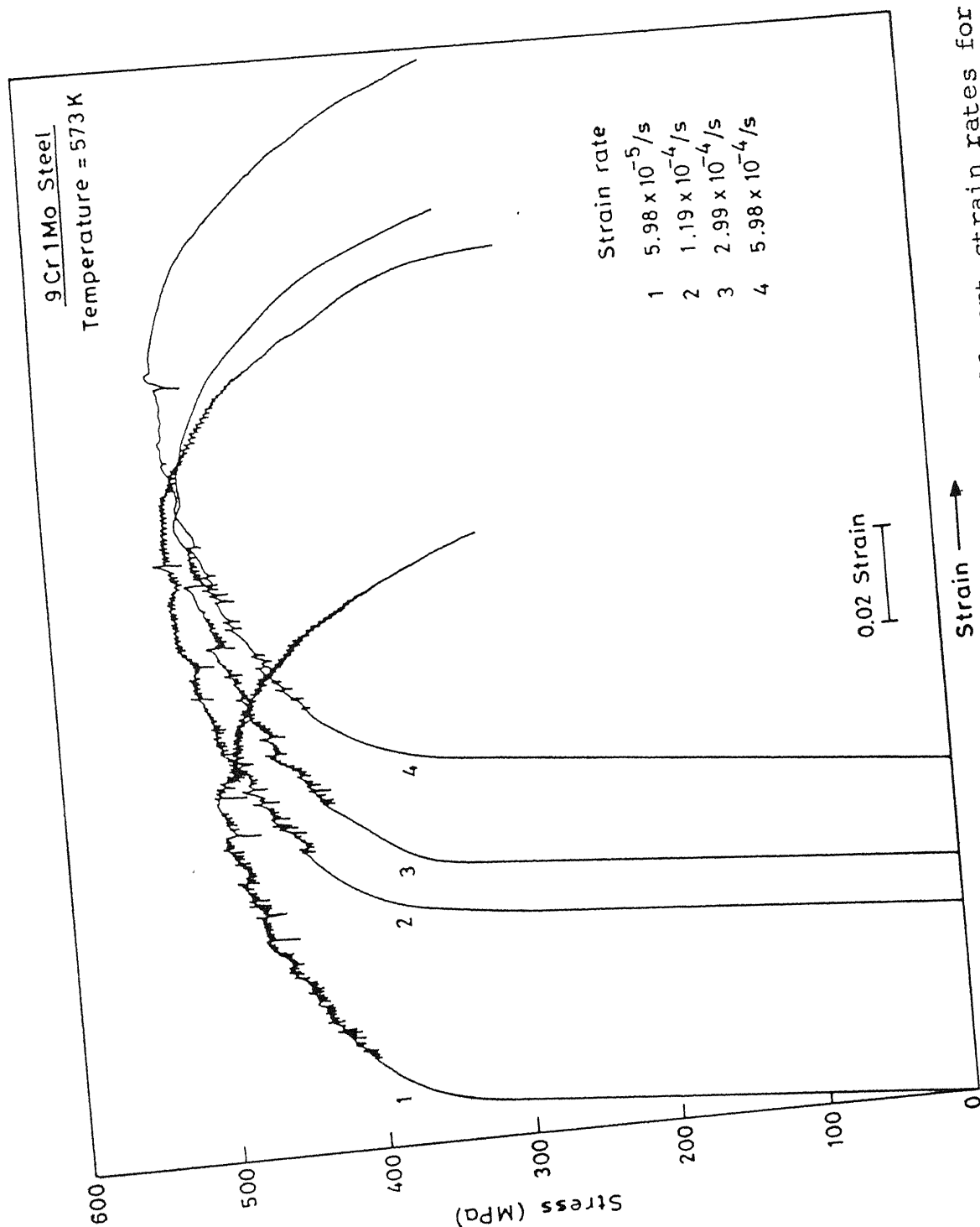


Fig. 4.17 Appearance of serrations (DSA) at 573K at different strain rates for 9 Cr-1 Mo steel.

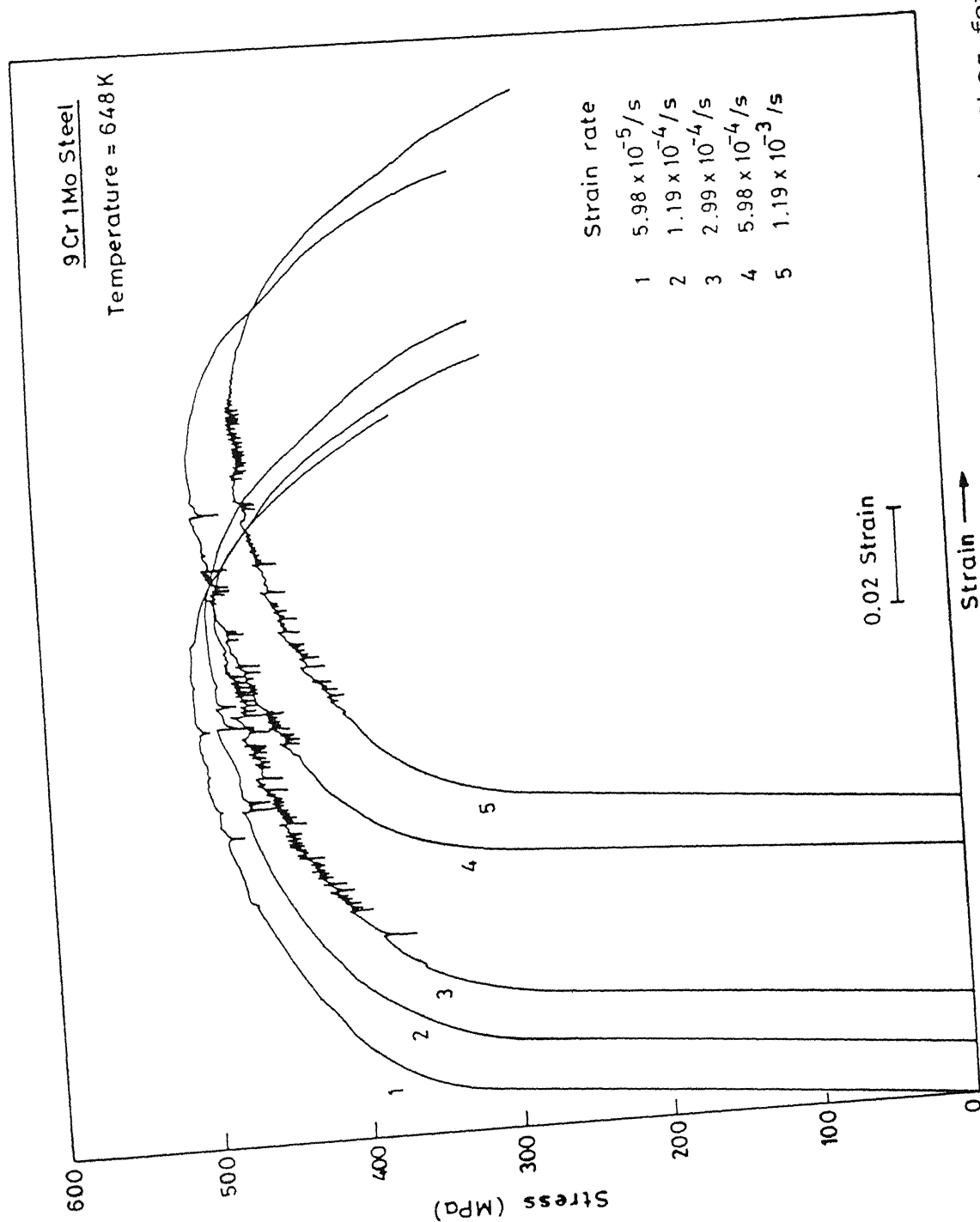


Fig. 4.18 Appearance of serrations (DSA) at 648K at different strain rates for 9 Cr-1 Mo steel.

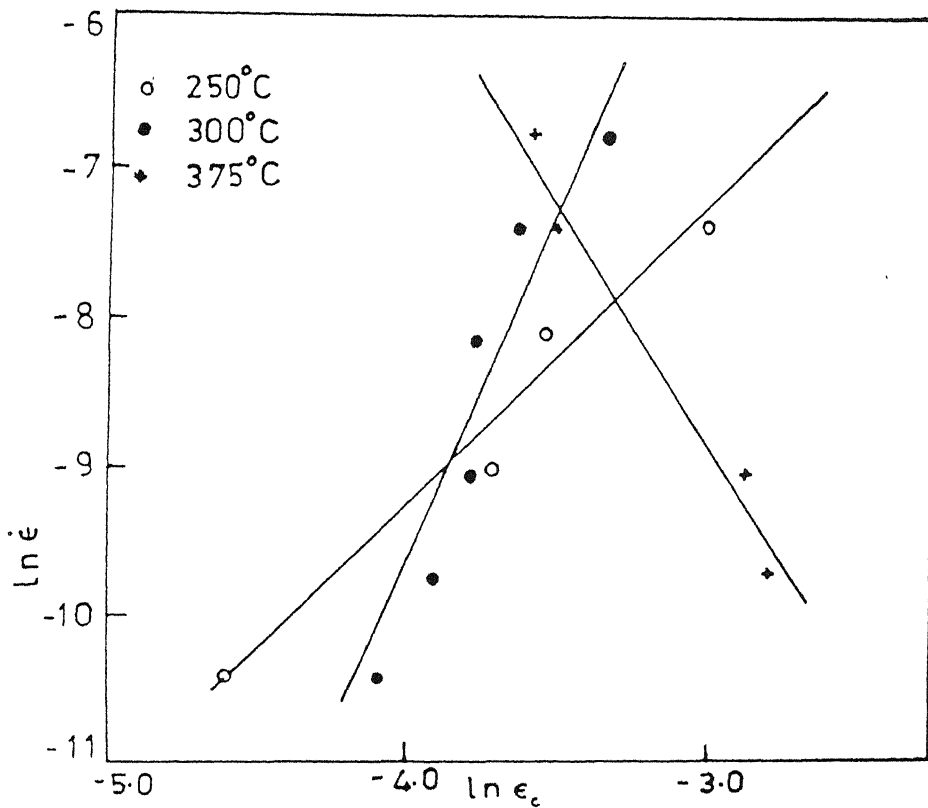


Fig. 4.19 Variation of critical strain at the appearance of DSA in 9 Cr-1 Mo steel as a function of strain rate at different temperatures.

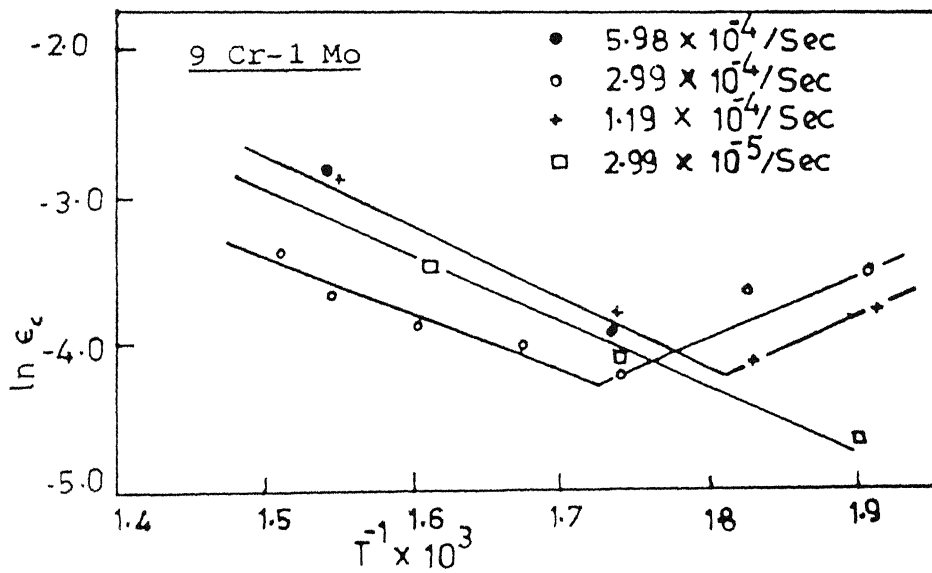


Fig. 4.20 Variation of critical strain at the appearance of DSA as a function of temperature at different strain rates.

process is obtained as 9.839×10^{-20} J (0.614 eV), 1.326×10^{-19} J (0.828 eV) and 1.369×10^{-19} J (0.854 eV) at 523K, 573K and 648K respectively.

The activation energy for carbon diffusion in iron is about 1.2×10^{-19} J (0.75 eV). The experimentally obtained values agree with this value within the experimental error. Hence the arrest of dislocations by carbon diffusing into the dislocations might be the rate controlling process.

Figure 4.20 shows an anomalous behaviour of $\ln \epsilon_c$ versus $1/T$ at higher temperatures. A similar behaviour is also observed in Figure 4.19. It indicates that the carbon may be tied up in some other way than the pinning of dislocation during the earlier parts of the deformation process at these higher temperatures. Similar behaviour was reported by Nakado and Keh [47] for Ni-C alloys, Hayes and Hayes [46] for Waspalloy and Hayes and Hayes [48] for AISI 1020 and $2\frac{1}{4}$ Cr-1 Mo steels.

4.4 Stress Relaxation:

Stress relaxation as a function of time for the 9 Cr-1 Mo steel strained to 3% tensile strain at different temperatures is shown in Figure 4.21. In general, the amount of stress relaxed in a particular time decreases as temperature is increased upto 573K. Above this temperature, the relaxation is increased but again following the same trend with temperature. Similar behaviour is also observed in Figures 4.22 and 4.23 which show stress relaxation taking place in samples deformed to 4.7% and 6.0% tensile strains respectively.

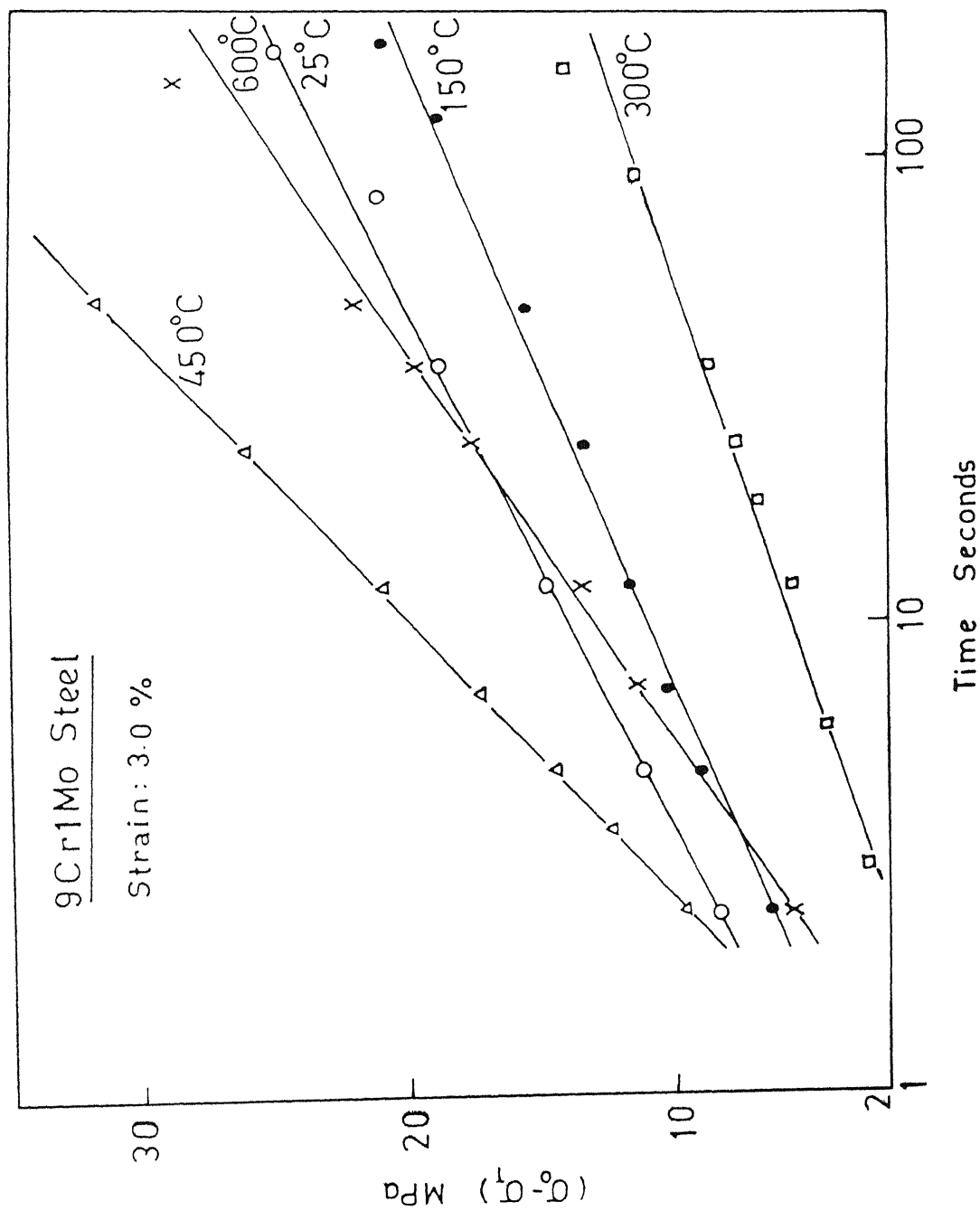


Fig. 4.21 Stress relaxation versus time at 3% tensile strain for the 9 Cr-1 Mo steel at different temperatures.

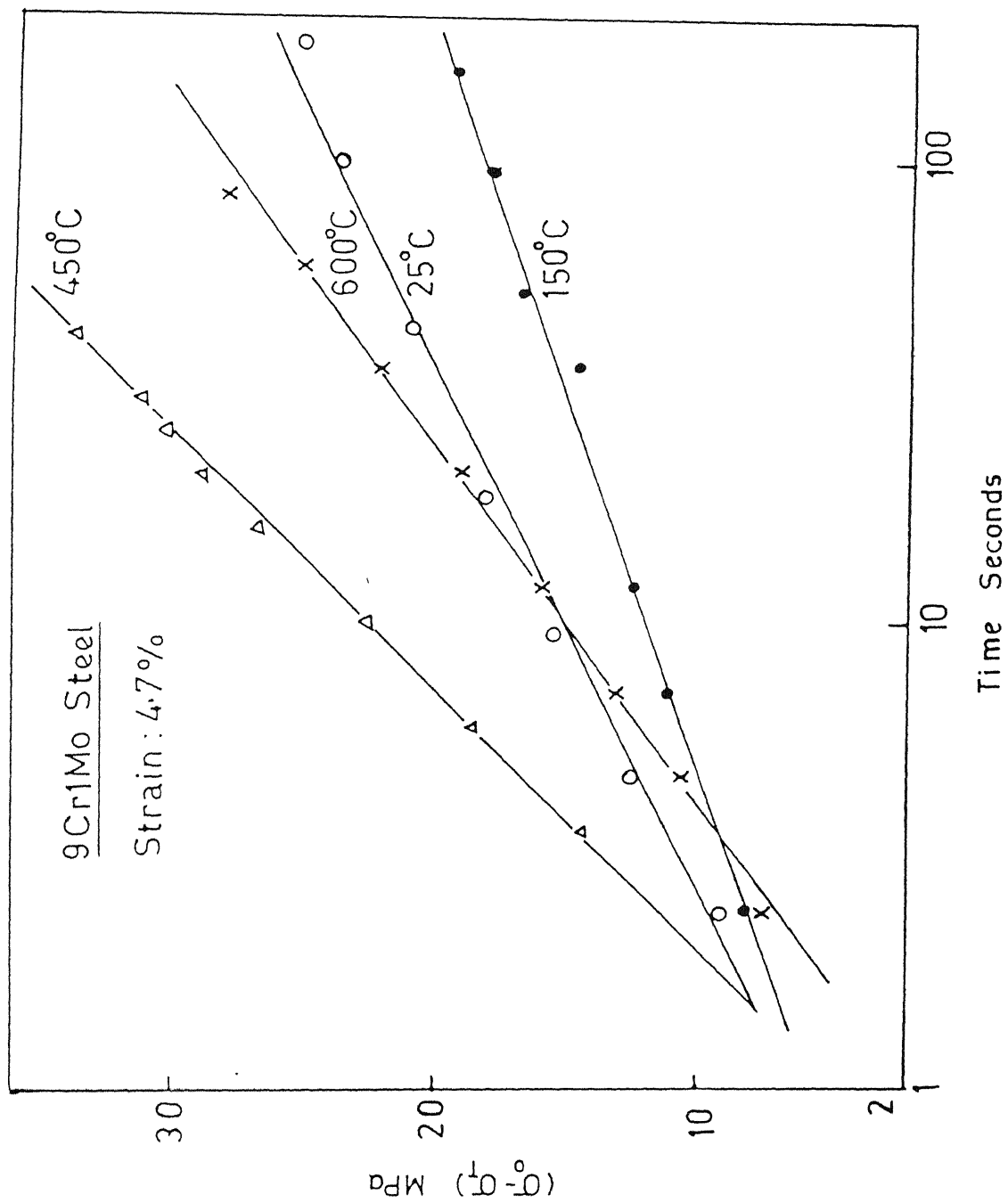


Fig. 4.22 Stress relaxation versus time at 4.7% tensile strain for the 9 Cr-1 Mo steel at different temperatures.

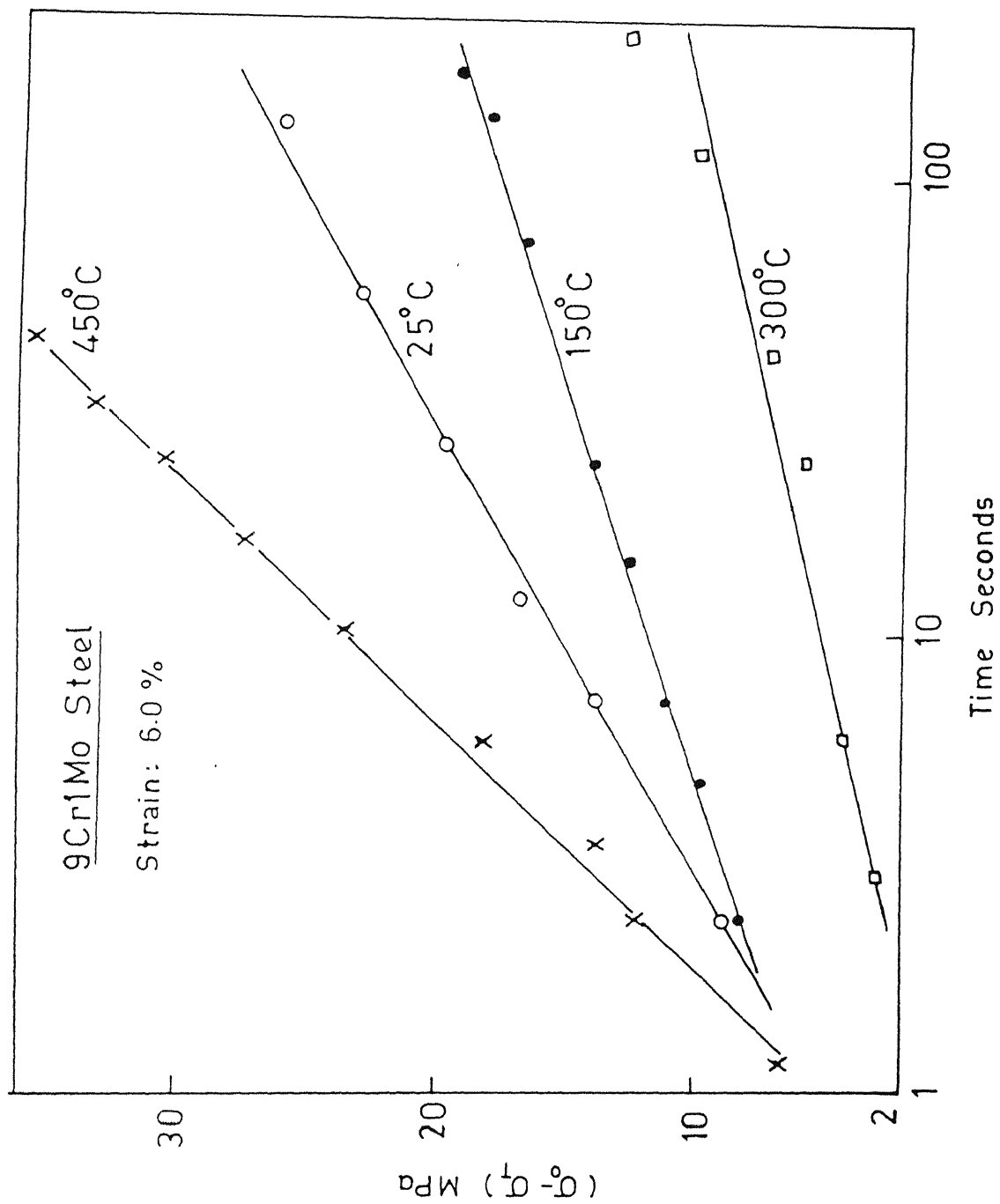


Fig. 4.23 Stress relaxation versus time at 6.0% tensile strain for the 9 Cr-1 Mo steel at different temperatures.

Figures 4.24 and 4.25 give the variation of stress relaxation as a function of time for the 9 Cr-1 Mo steel deformed to different strain levels at 298K and 723K respectively. Both of these show that the stress relaxed in a particular time period do not vary much as strain level is changed. Nevertheless, the increase in stress relaxation as the strain level is increased can be clearly seen.

Figures 4.26, 4.27 and 4.28 show the results of stress relaxation experiments on 316 SS done at different temperatures to strain levels of 3%, 5.5% and 8.2% respectively. A behaviour similar to that of the 9 Cr-1 Mo steel is observed although the stress relaxed at 723K is not greater than that at 298K. Stress relaxation as a function of time at different strain levels at 298K and 423K are shown in Figures 4.29 and 4.30 respectively. As observed in 9 Cr-1 Mo steel, the stress relaxation increases with the increase in the strain level.

These observations can be explained by considering the dislocation motion, since the stress relaxation takes place due to the continued motion of dislocations at constant strain. At any particular stress, the number of dislocations crossing the barriers depends on the thermal fluctuation. At higher temperature, thermal fluctuations enhance the number of dislocations moving past the obstacles. This results in decreased number of dislocations held up at the barriers which are available for stress relaxation as temperature is increased.

Physical metallurgy of both these steels is well known [1, 8, 72, 73]. Secondary hardening takes place in the temperature range of 700-900K. This would increase pinning of dislocations.

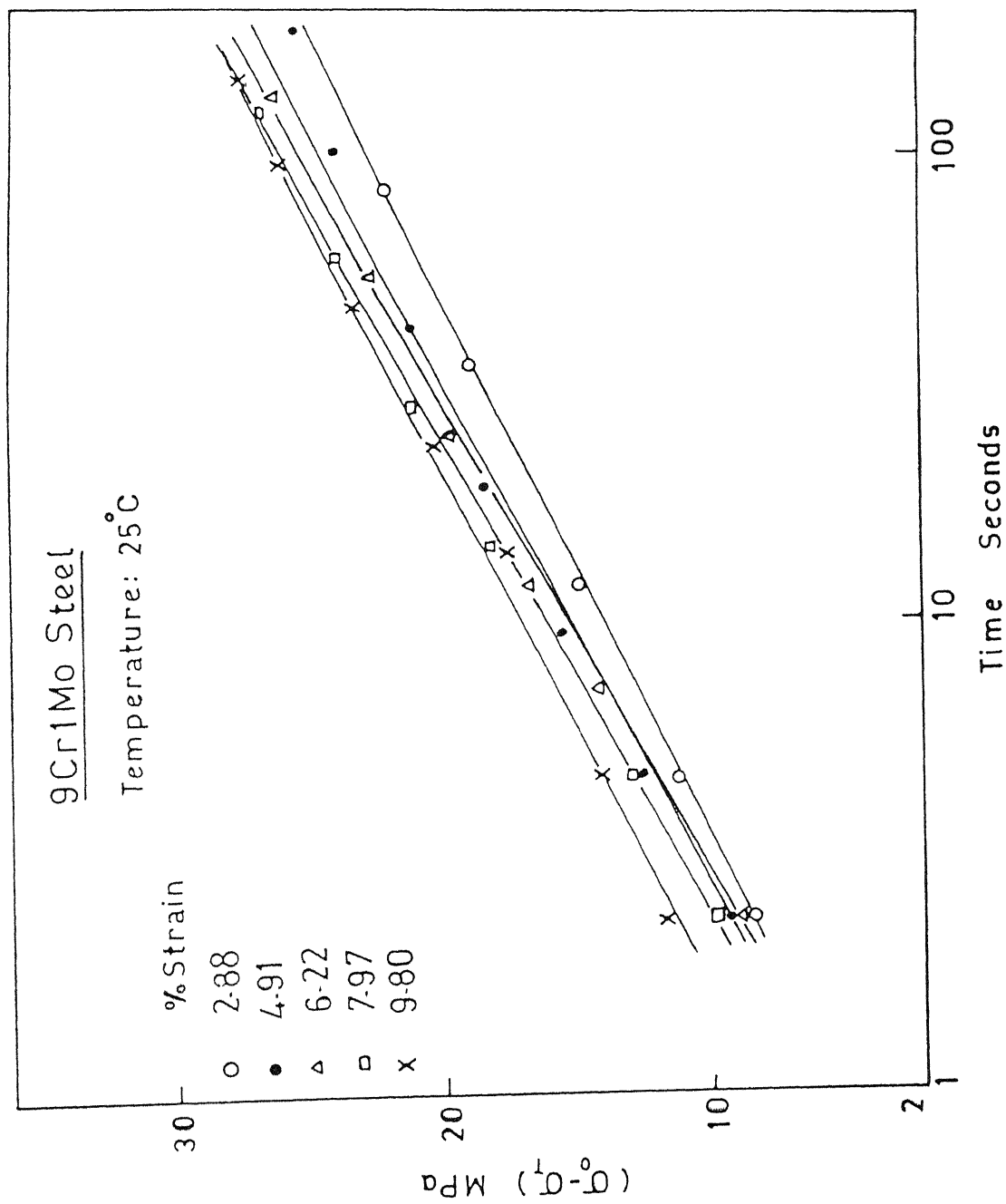


Fig. 4.24 Stress relaxation versus time at 25°C (298K) for the 9 Cr-1 Mo steel at different strain levels.

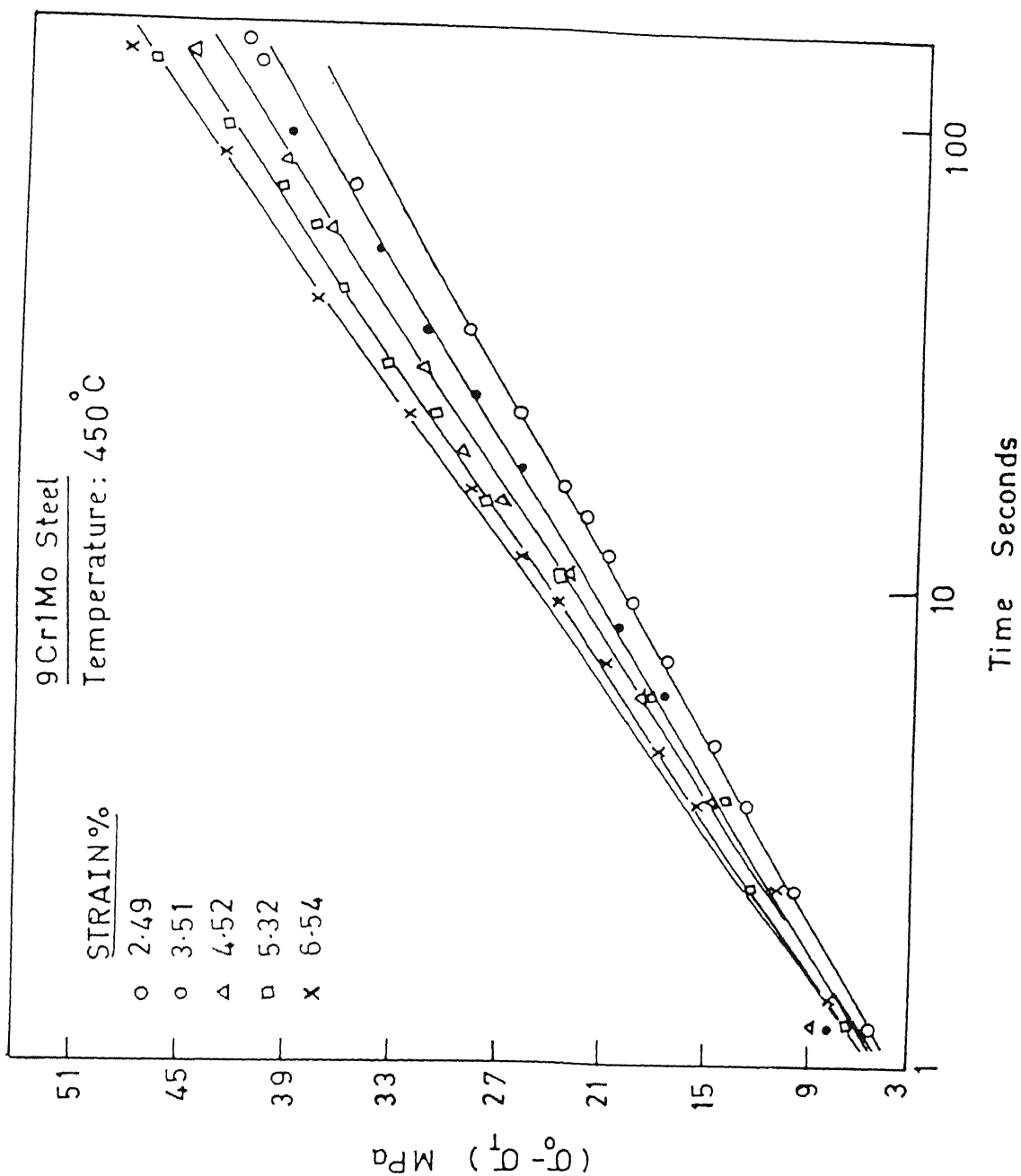


Fig. 4.25 Stress relaxation versus time at 450°C (723K) for the 9 Cr-1 Mo steel at different strain levels.

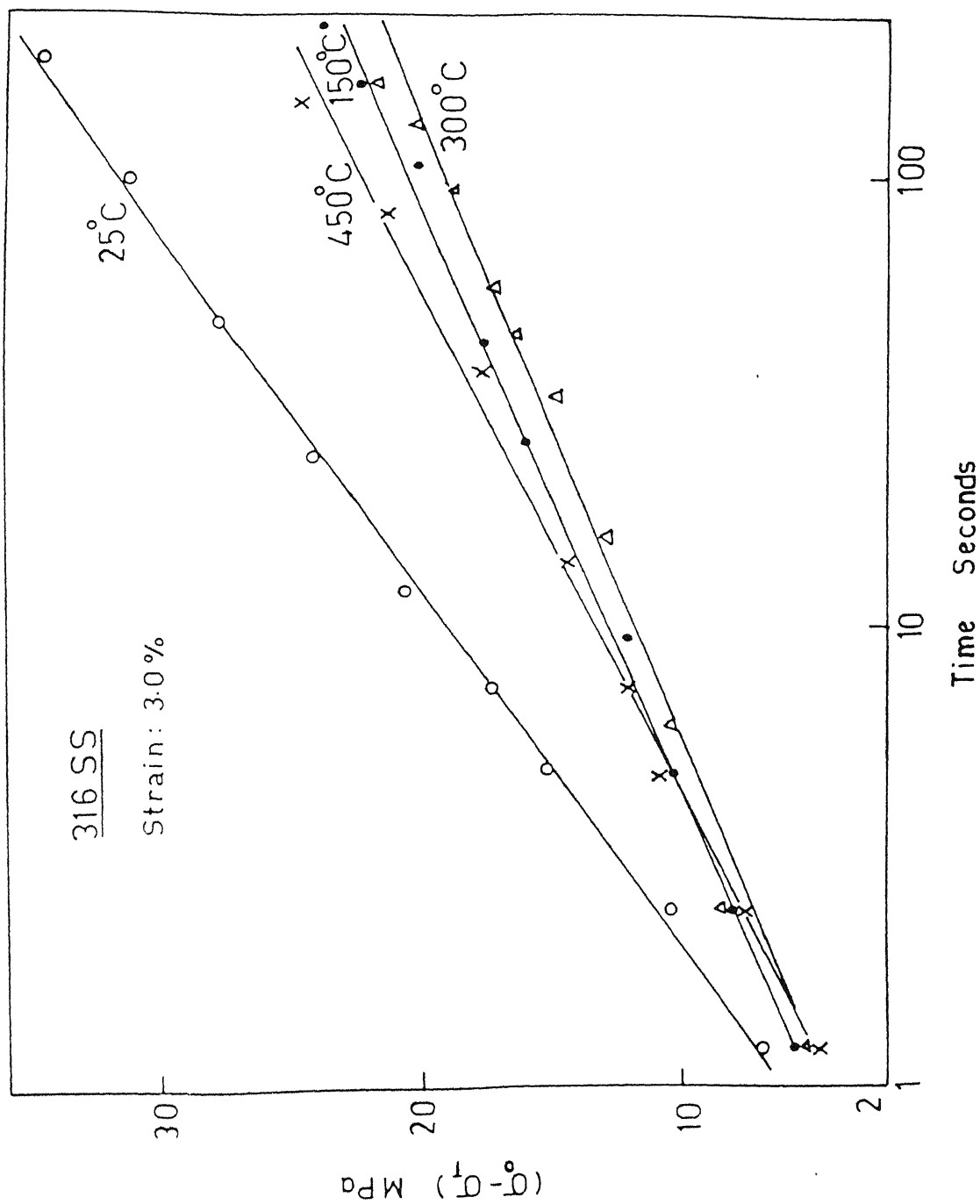


Fig. 4.26 Stress relaxation versus time at 3% tensile strain for the 316 SS at different temperatures.

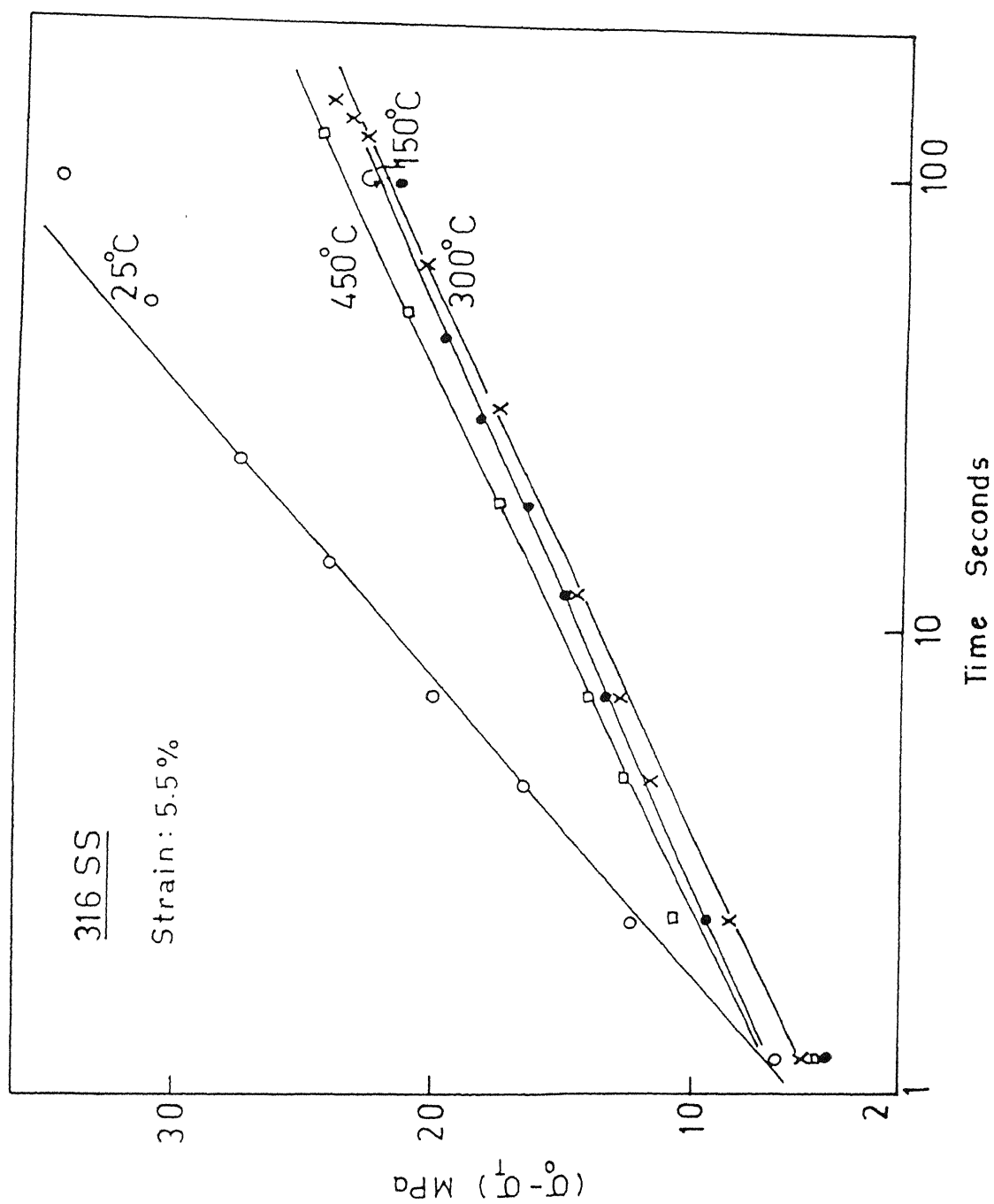


Fig. 4.27 Stress relaxation versus time at 5.5% tensile strain for the 316 SS at different temperatures.

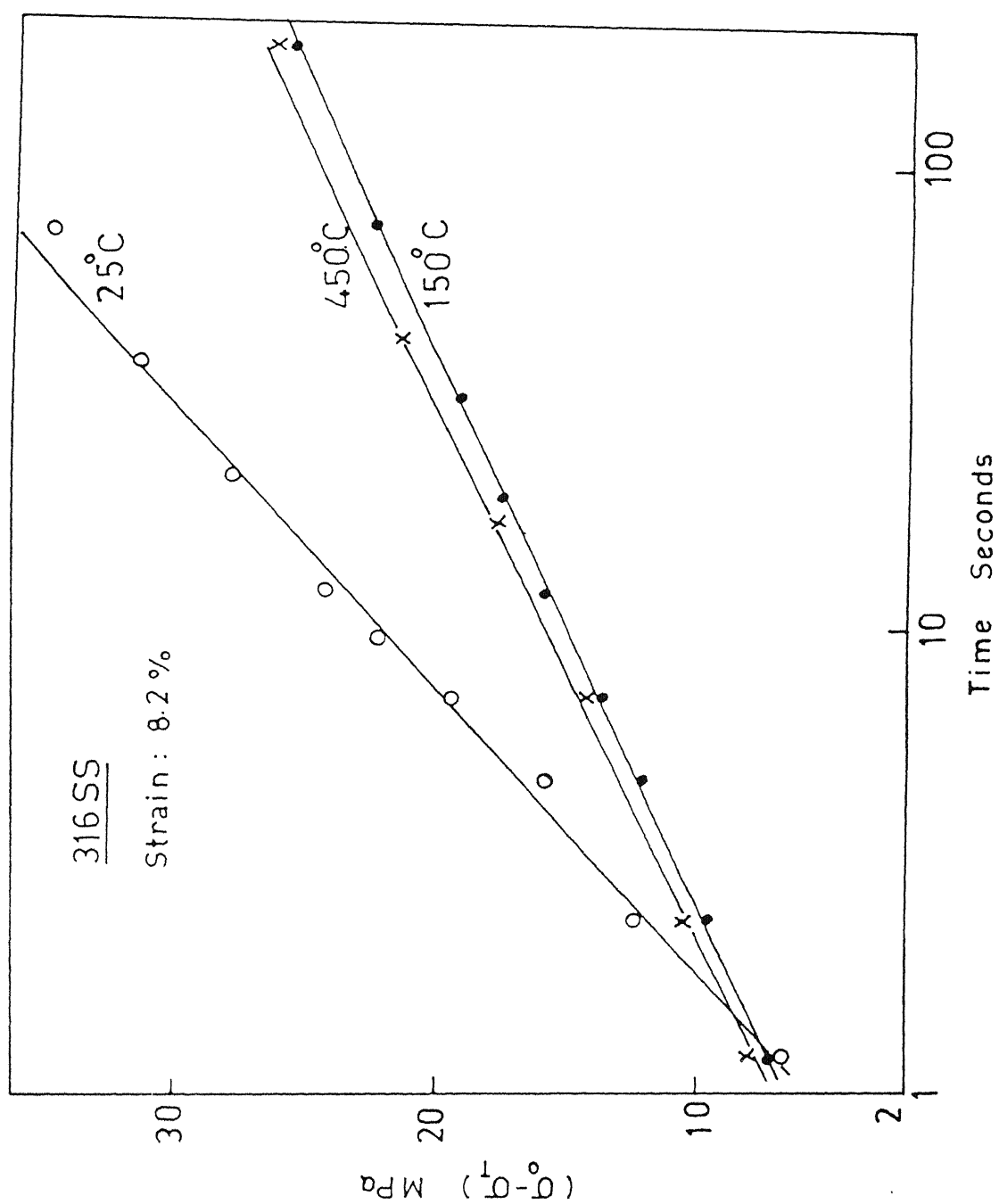


Fig. 4.28 Stress relaxation versus time at 8.2% tensile strain for the 316 SS at different temperatures.

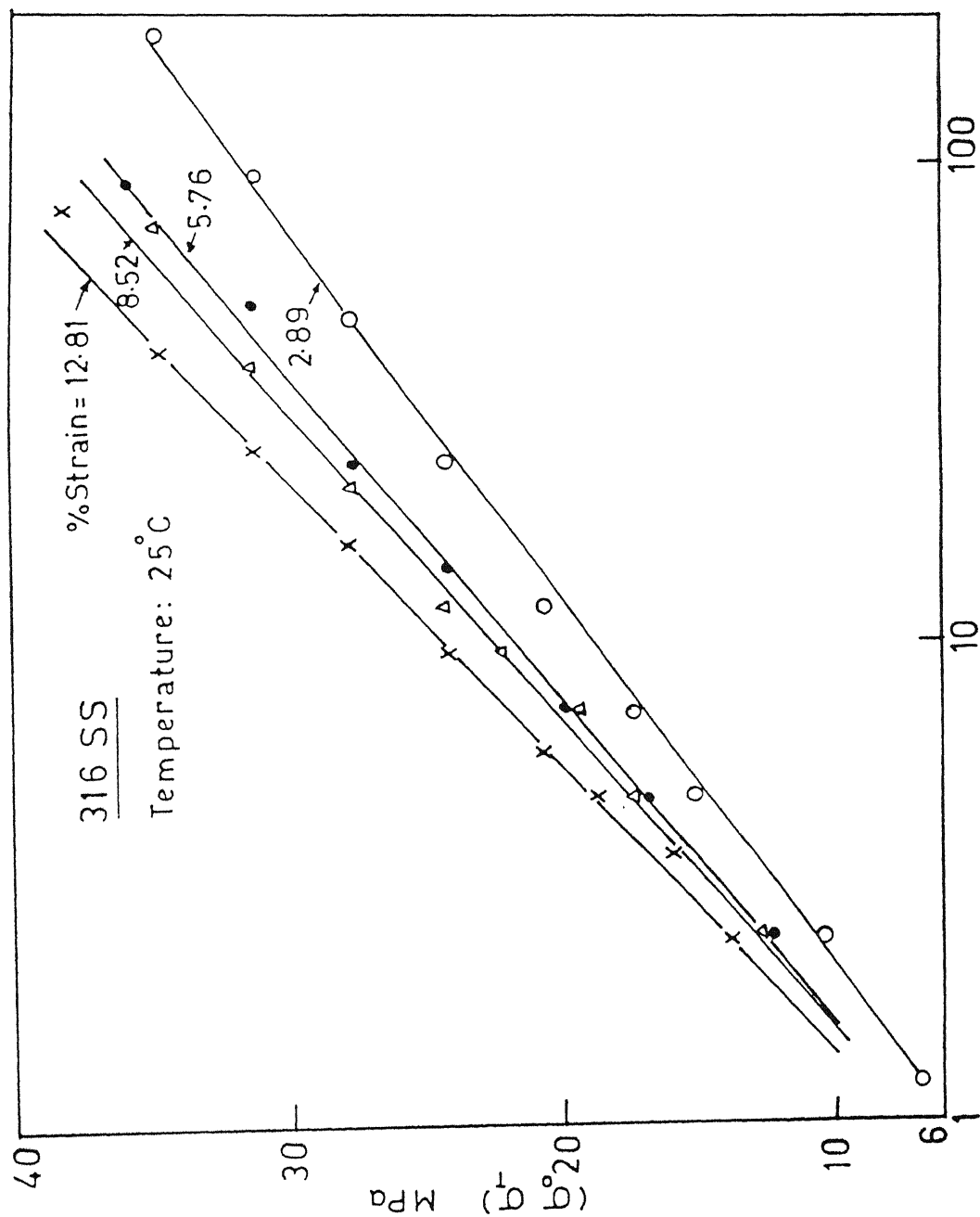


Fig. 4.29 Stress relaxation versus time at 25°C (298K) for the 316 SS at different strain levels.

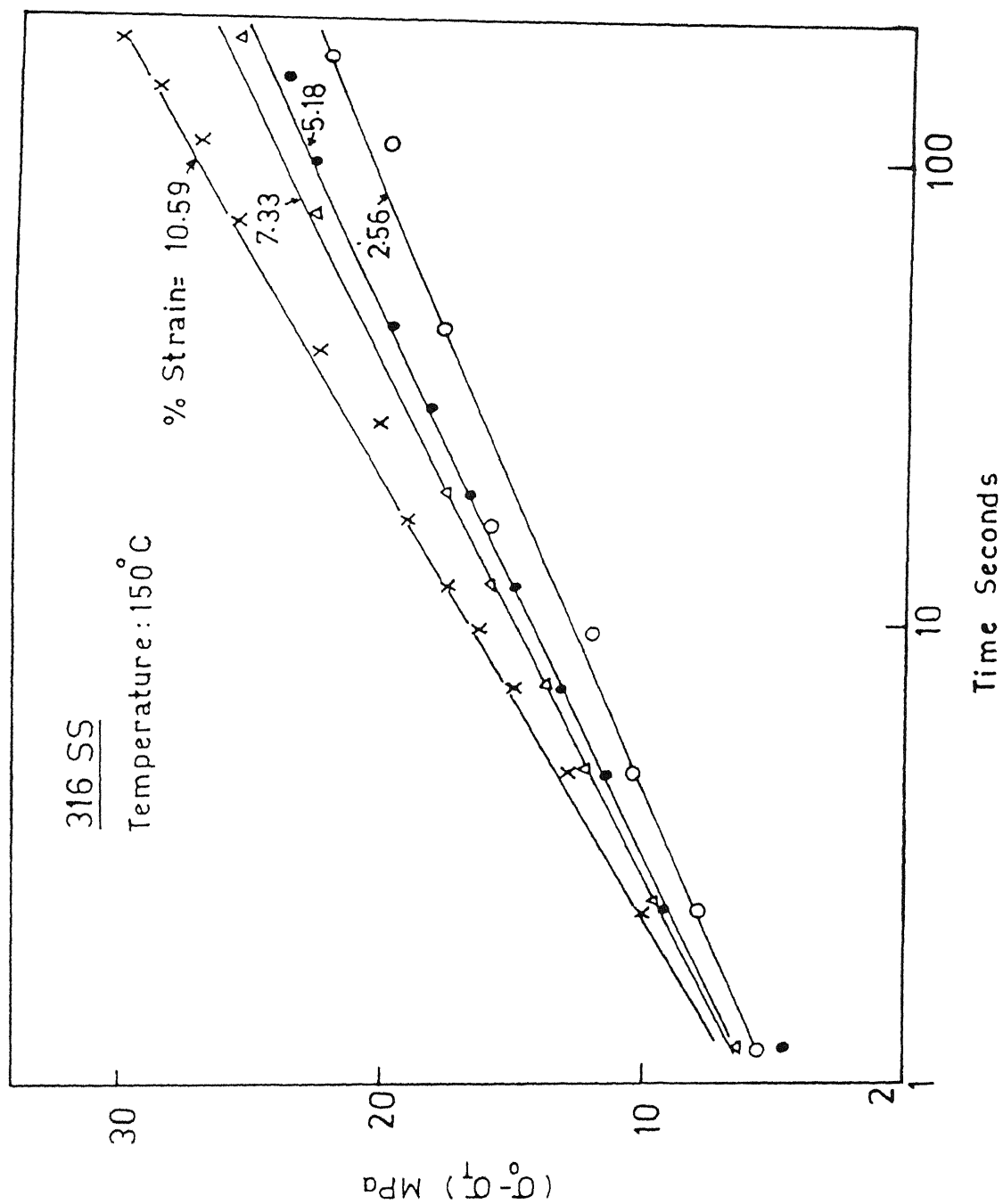


Fig. 4.30 Stress relaxation versus time at 150°C (423K) for the 316 SS at different strain levels.

These dislocations would be thermally activated causing plastic flow and stress relaxation.

The stress relaxation versus time in log scale fall on a straight line very much like the original findings of Feltham [52, 53]. A least square fit was used to get the slopes of these plots. This is used to calculate activation volume using the rewritten Eq. 2.62,

$$V^* = \frac{2kT}{S_r} / \left[1 + \frac{\theta a}{E l_s} \right] \quad (4.2)$$

where

S_r is the slope of $(\sigma_0 - \sigma_t)$ versus t plot,

σ_0 is the stress at the beginning of stress relaxation,

σ_t is the stress at any time t ,

θ is the work hardening coefficient,

$= \frac{d\sigma}{d\epsilon}$ obtained from the true stress versus true strain curve,

a is the cross-sectional area of the specimen,

E is the modulus of load cell and

l_s is the length of the specimen at the strain at which relaxation is done.

In the present case,

$$\theta = 2500 \text{ MPa } (2500 \text{ N/mm}^2)$$

$$a = 7.05 \text{ mm}^2$$

$$E = 3.3 \times 10^6 \text{ N/mm and}$$

$$l_s = 28.5 \text{ mm}$$

This gives

$$\frac{\theta a}{E l_s} \simeq 0.0002$$

Hence this term can be neglected without much effect on the calculated value of activation volume. Activation volumes calculated are shown in Figures 4.31 and 4.32 against shear strain at different temperatures for the 9 Cr-1 Mo steel and for the 316 SS respectively. As can be seen from these plots, activation volume essentially remains constant with strain and increases with increase in temperature. Activation volumes obtained fall in the ranges of 100-200 b^3 for the 9 Cr-1 Mo steel and 50 to 150 b^3 for the 316 SS.

4.5 Load Cycling:

It was observed that the introduction of creep hold does not alter the amount of energy absorbed per cycle. Hence only the results of simple load cycling tests are represented. Experimentally obtained energy absorbed per cycle (ΔE_0) values are shown in Figure 4.33 as a function of time and tensile strain at which load cycling was carried out. The energy absorbed per cycle values are observed to fall in a band in both the steels.

For the experimentally obtained values of energy absorbed per cycle, a multiplication factor of 1/2.8 was used to get the energy under shear stress-strain curves. Shear modulus and lattice parameter corrections are applied to these energy values. The shear modulus variations are obtained from the works of Engler [74] on B.C.C. iron and Hoke [75] for 9 Cr-1 Mo steel and 316 SS respectively. To correct for the variations in lattice parameter, the thermal expansion coefficient $\alpha = 12 \times 10^{-6}/^\circ\text{K}$ for steels is made use of in both the cases. The correction factor is given by

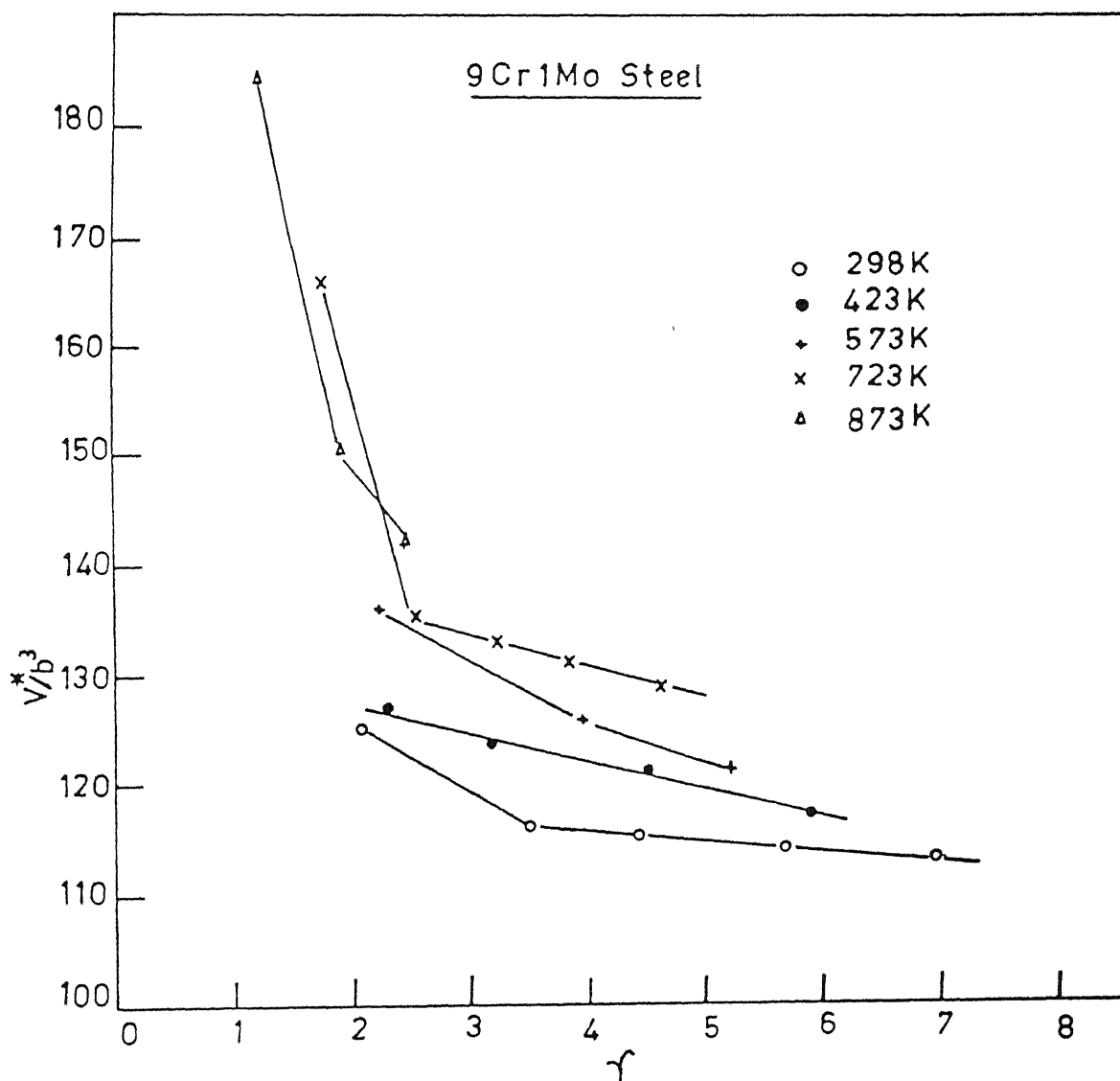


Fig. 4.31 Activation volume determined from stress relaxation versus shear strain for the 9 Cr-1 Mo steel at different temperatures.

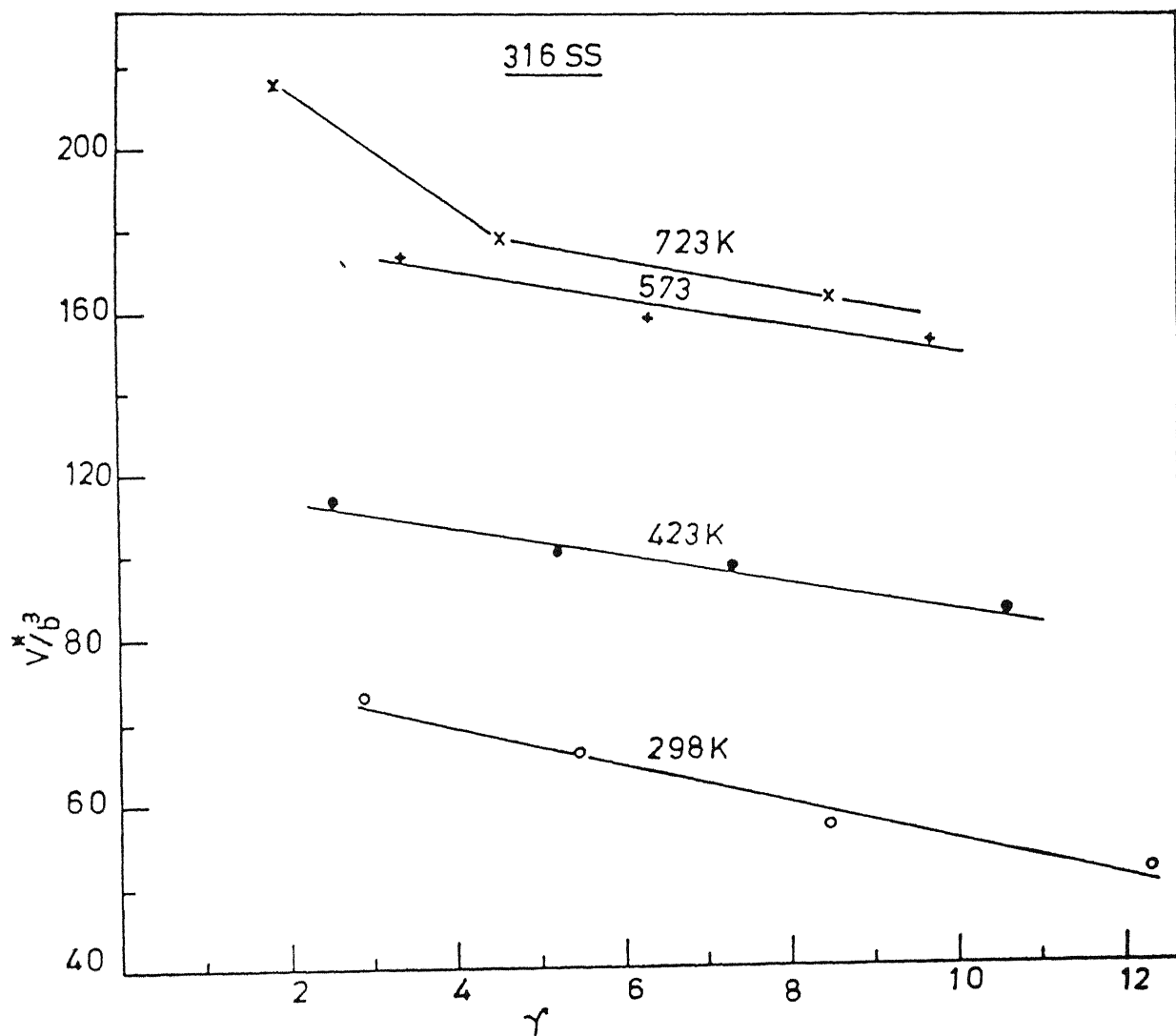


Fig. 4.32 Activation volume determined from stress relaxation versus shear strain for the 316 SS at different temperatures.

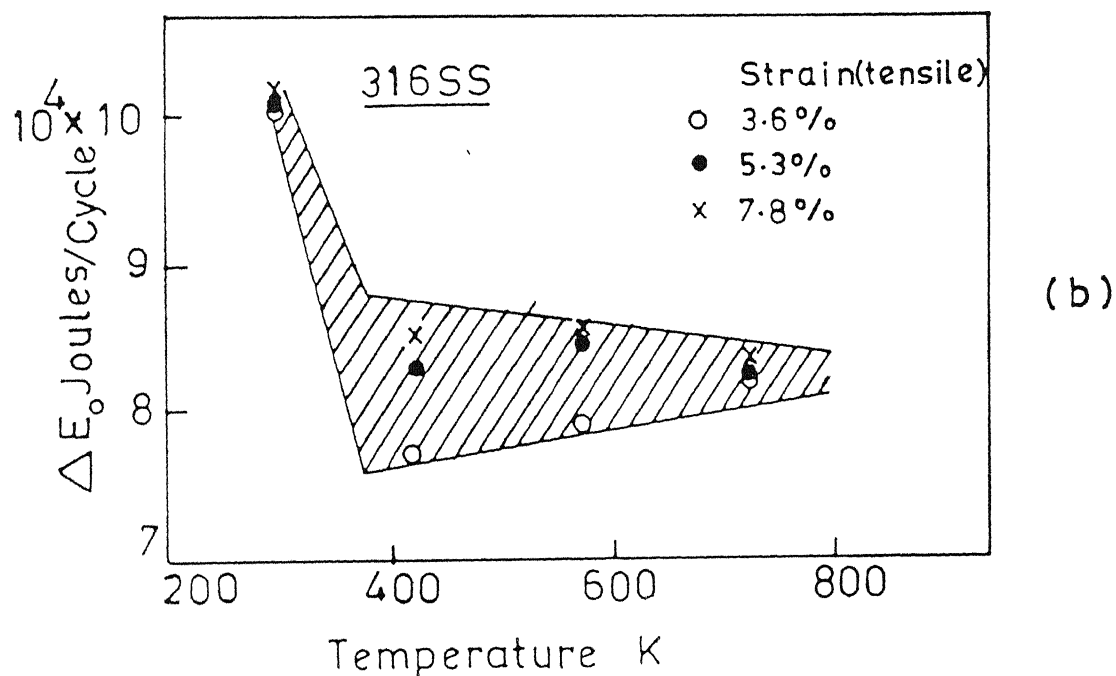
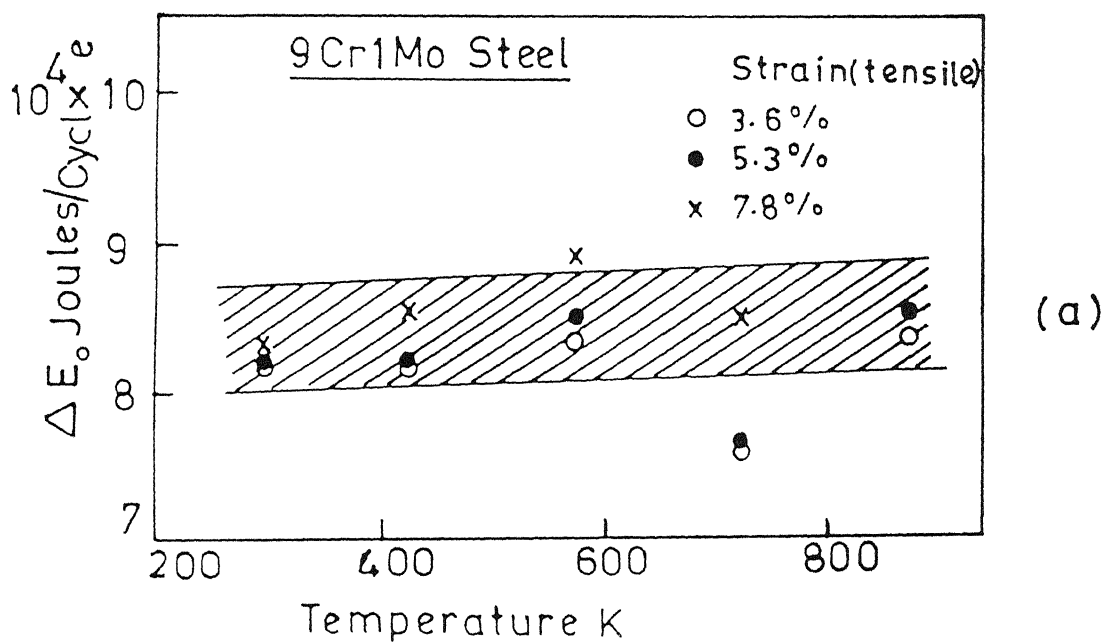


Fig. 4.33 Energy absorbed per cycle, ΔE_0 versus temperature at different strain levels for (a) 9 Cr-1 Mo steel and (b) 316 SS.

$$\frac{G_O b_O^2}{G_T b_T^2} = \left(\frac{G_O}{G_T}\right) \frac{1}{(1 + 2\alpha T)}$$

where

G_O is the shear modulus at 0°K

G_T is the shear modulus at $T^\circ\text{K}$

b_O is the lattice parameter at 0°K

b_T is the lattice parameter at $T^\circ\text{K}$

$$= b_O (1 + \alpha T)$$

α is the thermal expansion coefficient

$$[b_T^2 = b_O^2 (1 + 2\alpha T + \alpha^2 T^2) = b_O^2 (1 + 2\alpha T)]$$

Figure 4.34 shows the variation of ratio of energy absorbed per cycle (not corrected for variations in shear modulus and lattice parameter) to twice the elastic energy against temperature. For 9 Cr-1 Mo steel it shows a high value at 873K. Probably the curves obtained show a peak at around that temperature which is to be confirmed by carrying out energy measurements at temperatures less than 298K and higher than 873K. The shape of these curves is very similar to those found in internal friction after work hardening which is known as Köster peaks.

Variation of the ratio of energy absorbed per cycle (not corrected for variations in shear modulus and lattice parameter) to twice the elastic energy of 316 SS with temperature shows a small but wide peak at around 600°K . Before commenting on this behaviour it is necessary to make experimental measurements at other temperature regions.

Figure 4.35 shows the variation of $\ln\left(\frac{V^* \Delta E}{kT}\right)$ versus $1/kT$ where ΔE is the value corrected for shear modulus and lattice

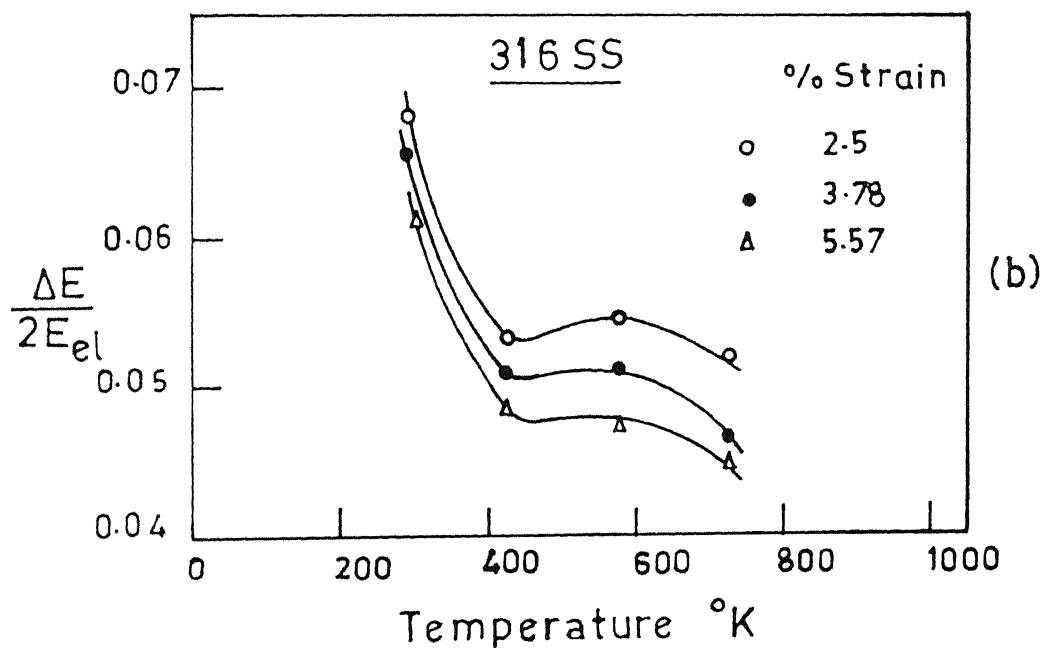
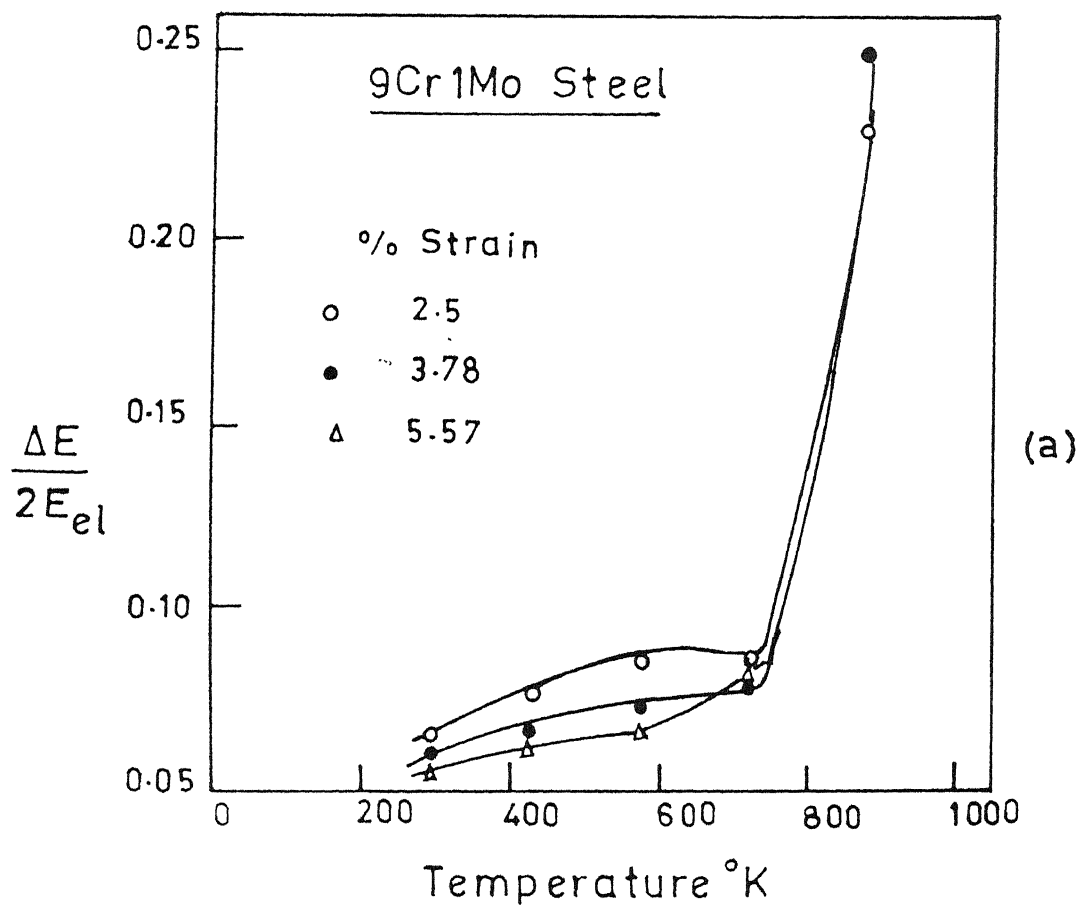


Fig. 4.34 Ratio of energy absorbed per cycle to twice the elastic energy versus temperature at different strains for (a) 9 Cr-1 Mo steel and (b) 316 SS.

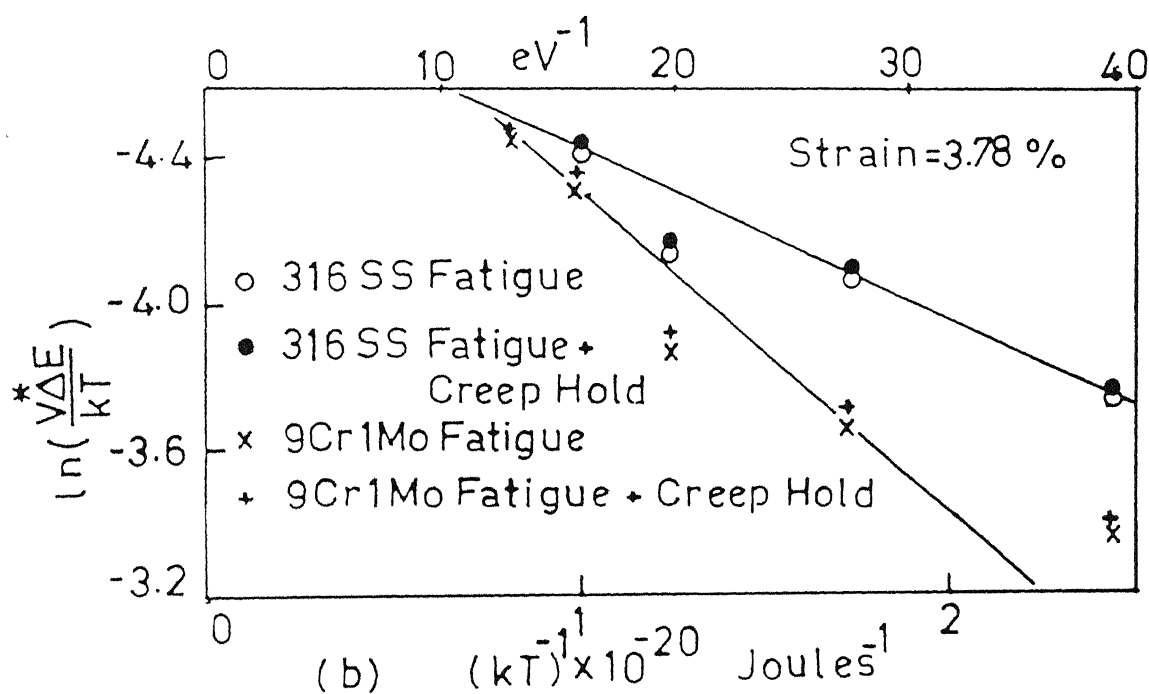
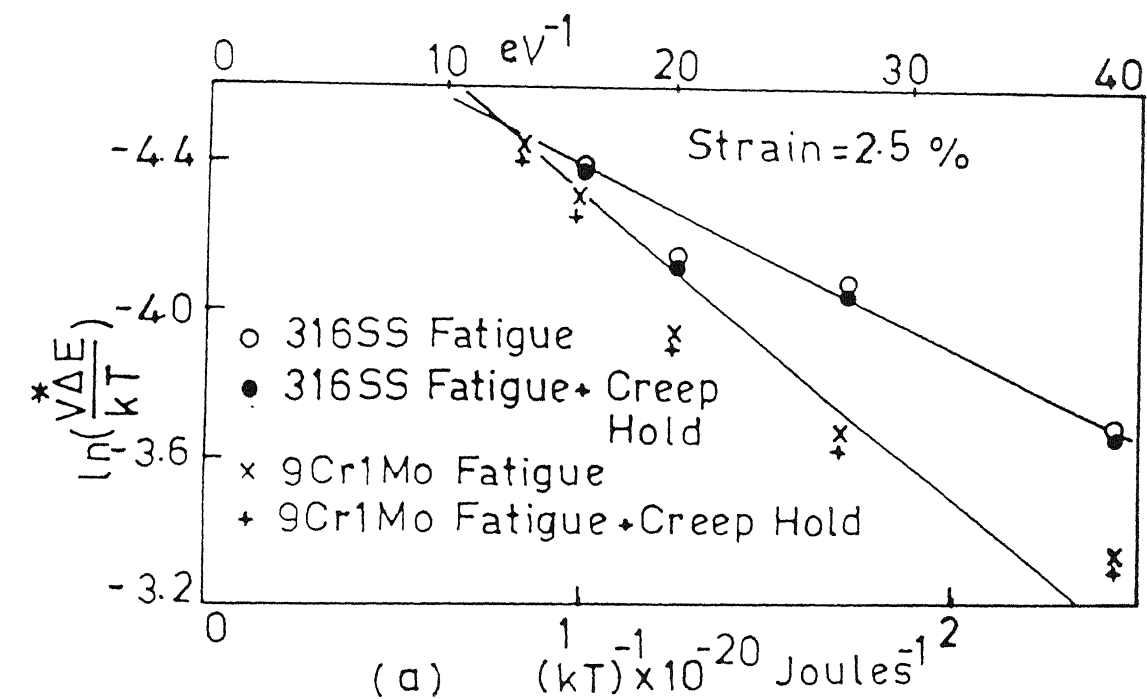
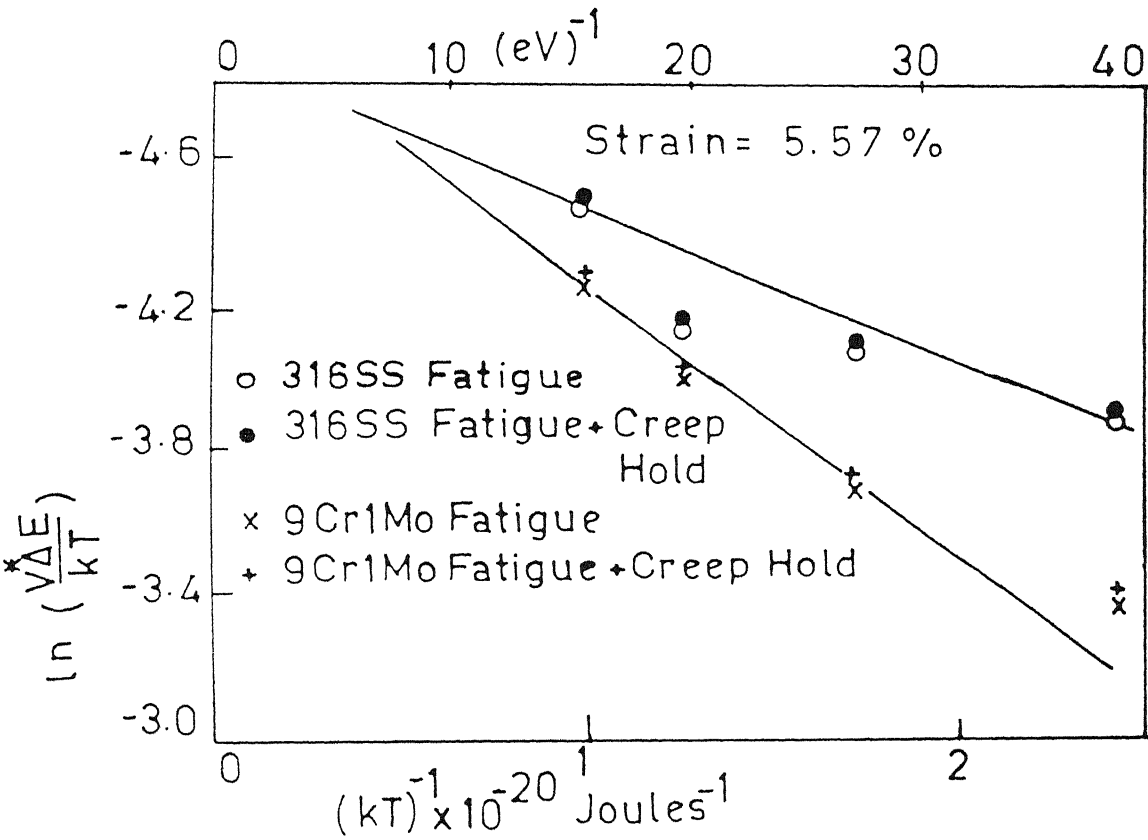


Fig. 4.35 $\ln\left(\frac{V^* \Delta E}{kT}\right)$ versus $1/kT$ for the two steels at
(a) 2.5%, (b) 3.78% and (c) 5.57% shear strains.



(c)

parameter variations. The linear plot gives the slope varying between 7.8×10^{-21} J (0.049 eV) and 8.6×10^{-21} J (0.054 eV) for the 9 Cr-1 Mo steel and, 4.4×10^{-21} J (0.027 eV) and 4.8×10^{-21} J (0.03 eV) for 316 SS. From these slopes and knowing V^* , $\Delta\tau_R$ and τ_i , the value of U_0 is calculated at different temperatures. The variation of U_0 with temperature is shown in Figures 4.36 and 4.37 for the 9 Cr-1 Mo steel and 316 SS respectively. The values of U_0 at different temperatures agree with the values of the binding energy of carbon to a dislocation. Hence the activation process which controls the dislocation motion during load cycling might be overcoming the interaction between carbon interstitials and a dislocation.

The variation of U_0 with temperature is interesting and it differs in the two materials considered. 9 Cr-1 Mo steel which is B.C.C. gives a decreasing U_0 with increase in temperature. This is in agreement with the fact that thermal fluctuations decrease the binding energy. But the behaviour of 316 SS is in opposition to this, and increases with temperature and shows a peak at about 650K. Dislocations in the 316 SS with an F.C.C. structure, will be extended giving rise to stacking faults and stainless steels are known to have a stacking fault energy of about 25-45 mJ/m². The Suzuki interaction which involves either segregation of substitutional solutes into the stacking fault or their desegregation would lead to carbon-substitutional solute atom binding instead of carbon-dislocation binding. All these would lead to a complicated behaviour.

Here it is interesting to consider the first term on the right side of Eq. 2.76,

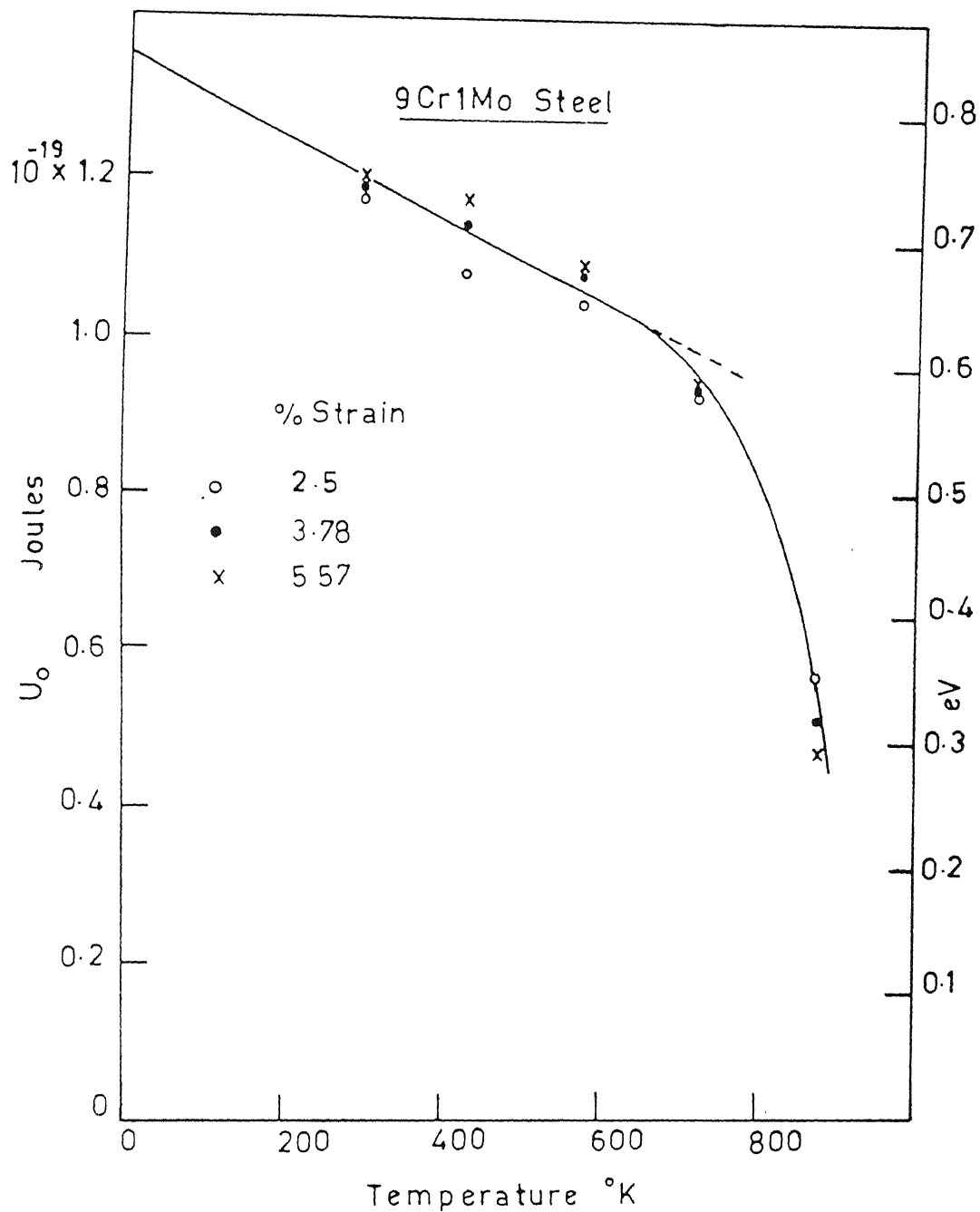


Fig. 4.36 Variations of activation energy U_0 with temperature for 9 Cr-1 Mo steel at different strain levels.

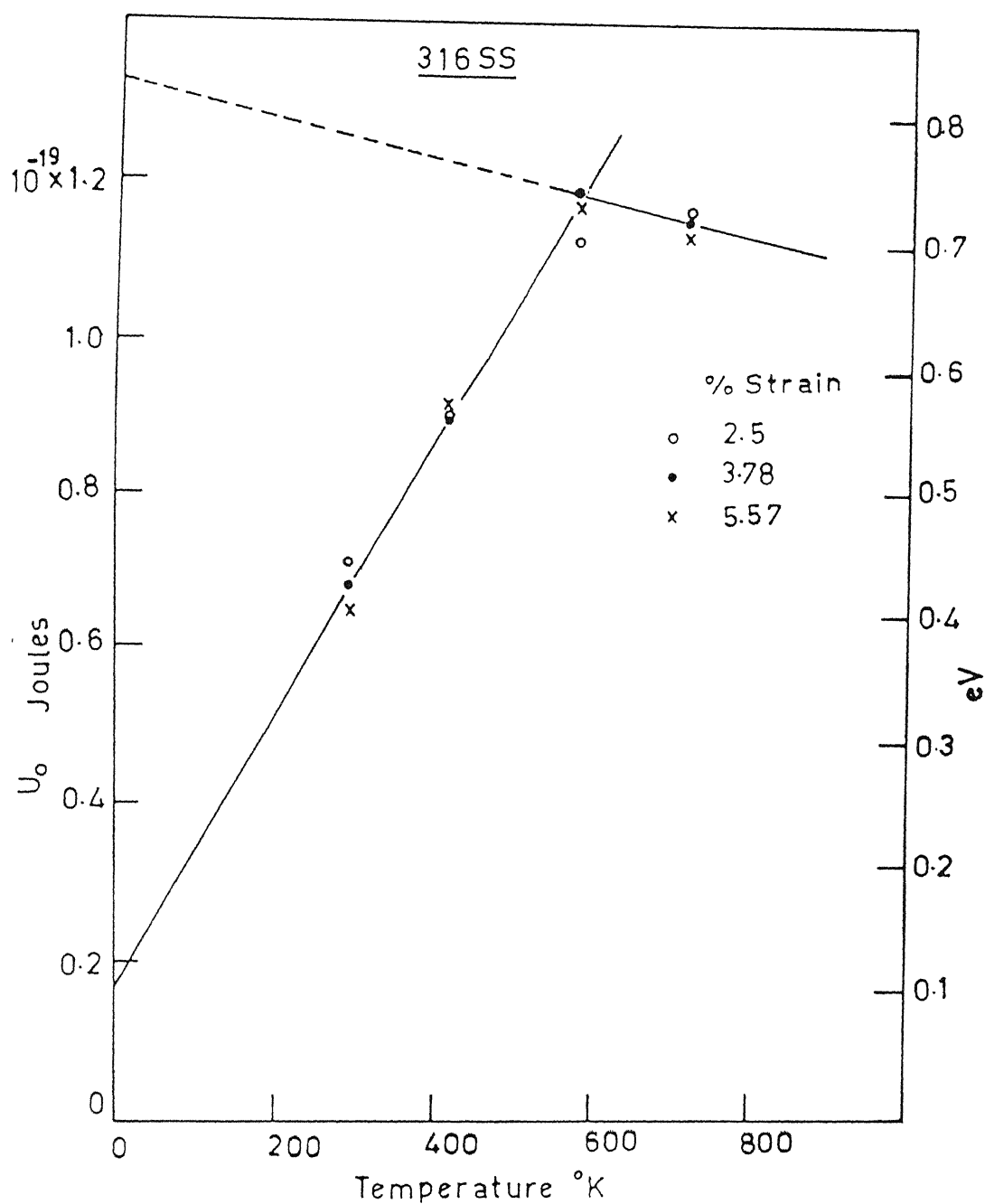


Fig. 4.37 Variation of activation energy U_0 with temperature for the 316 SS at different strain levels.

$$\ln\left(\frac{V^* \Delta E}{kT}\right) = \ln 2\beta \left(\frac{V^* \tau_i}{h\nu}\right) (\rho b d^*) - \frac{U_0 - V^* (\Delta \tau_R - \tau_i)}{kT} \quad (2.76)$$

The value of β may vary between 0 and 1. Activation volume is obtained from relaxation test and τ_i from strain rate cycling tests as 60% of flow stress τ_m . The value of $V^* \tau_i$ remains essentially constant with temperature. In the present work for the 9 Cr-1 Mo steel it is 3.0216×10^{-19} J (1.886 eV). The dislocation density in this material is of the order of $10^{15}/\text{m}^2$ as determined in a later section. The characteristic distance d^* can be of the order of Burgers vector b which is 2.5×10^{-10} m for iron. The frequency of vibration of dislocation can be of the order of 10^{11} to $10^{13}/\text{sec}$. Assuming the dislocation frequency to be $10^{12}/\text{sec}$, we can estimate the constant as

$$\ln 2 \times \beta \times \frac{3.0216 \times 10^{-19}}{6.63 \times 10^{-34} \times 10^{12}} \times 10^{15} \times 2.5 \times 10^{-10} \times 2.5 \times 10^{-10} \\ \approx -5.168 \quad 0.0 \leq \beta \leq 1.0$$

This estimation of the intercept of $\ln \frac{V^* \Delta E}{kT}$ versus $1/kT$ plot matches with the experimentally obtained value which ranges between 5.0 and 5.75 at different strain levels. This close agreement between the experimental results and theoretical prediction would support the analysis.

4.6 Toughness Measurements:

Toughness values are obtained for the direct tensile tested samples. The specimens which were cycled for 70 cycles at three strain levels were then pulled in tension till fracture. The same was done for the specimens tested for load cycling with creep hold.

Toughness values obtained for each set of conditions are plotted against temperature in Figure 4.38 after applying shear modulus and lattice parameter corrections as explained in an earlier section. These values fitted into a series of straight lines of the form $U = U_0 - TS$ where U_0 is the toughness at absolute zero, U is the toughness at any temperature T and S is the slope corresponding to an entropy term. The toughness value of 316 SS at 298K was deviating very much from this linearity. This is associated with a very high strength and strain to fracture when compared to the high temperature values. The values of S and U_0 obtained by a least square fit are tabulated in Table 4.1 after applying a multiplication factor of 1/2.8. This is required because the measured toughness values are corresponding to engineering stress-strain curves and relating this to dislocation mechanism requires a conversion to shear stress-strain toughness.

When a crystal is plastically deformed a part of the work of deformation is stored in the lattice while the remaining work is dissipated as heat. The stored energy is used up in the formation of vacancies and as dislocation strain energy. It has been shown that the energy stored with the dislocations is about 5% of the total work [76]. The vacancy creation amounts for about 4.5 times the energy associated with the dislocations [77], i.e., about 22.5% of the total work is used up generally in the creation of point defects most of which would be vacancies. The remaining portion gets converted into heat.

The energy stored in dislocations depends only a little on the dislocation configuration, provided they are not piled up in large groups and the energy per unit length is given by:

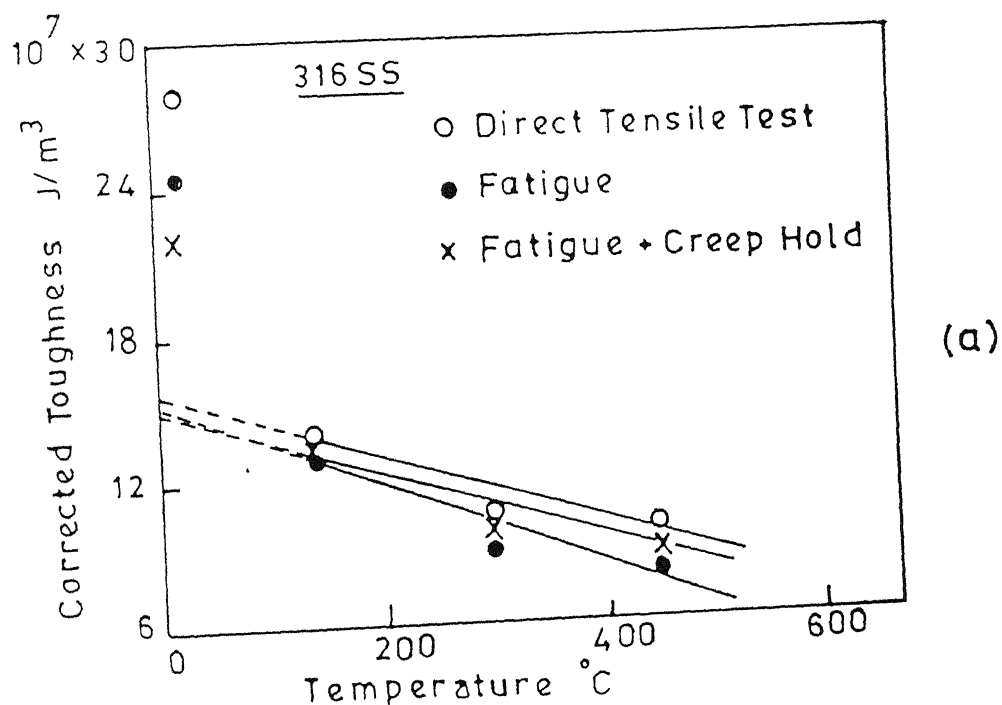
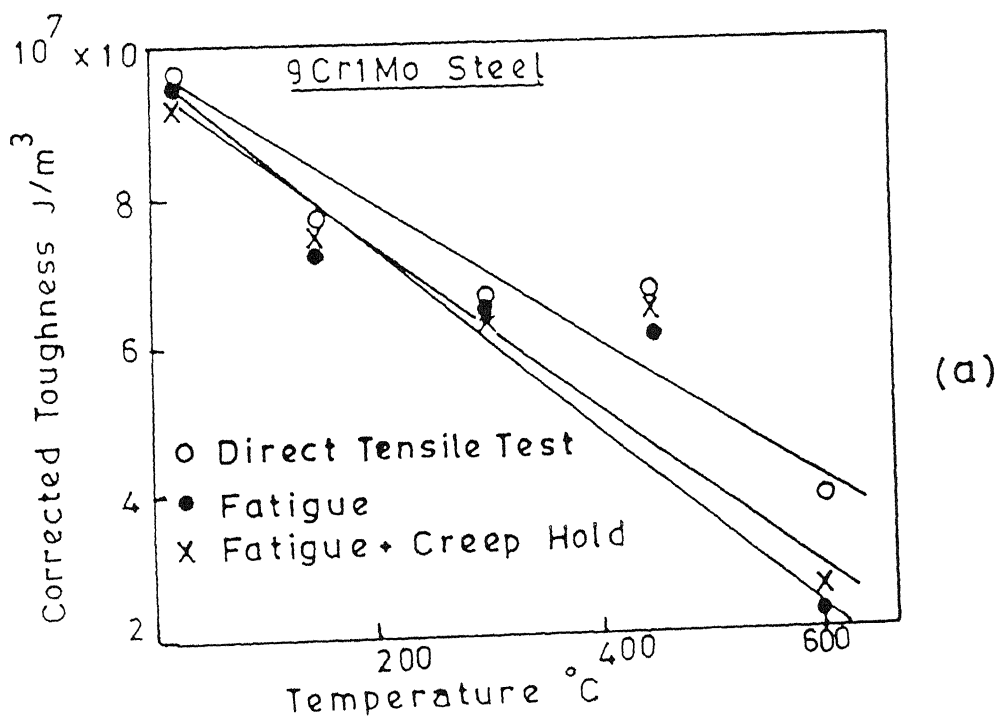


Fig. 4.38 Variation of corrected toughness with temperature at different test conditions for (a) 9 Cr-1 Mo steel and (b) 316 SS.

$$E_s = \frac{Gb^2}{4\pi(1-\nu)} (1 - \nu \cos^2\theta) \ln\left(\frac{R}{r_o}\right) \quad (4.3)$$

where, θ is the composition angle,

R is the outer cut off radius,

r_o is the inner cut off radius and

ν is the Poissons ratio.

In heavily deformed materials a suitable selection of the outer cut off radius R is to be made. In specimens of diameter 0.003 m the dislocation strain field may not extend beyond a radius of 10^{-5} m. A suitable approximation will be the average spacing between dislocations which is simply $(1/\rho^{1/2})$ where ρ is the dislocation density. Generally dislocation density is of the order of 10^{13} to $10^{16}/m^2$. It gives an average spacing of 10^{-7} m which will be very good approximation for the outer cut off radius. Taking $\nu = 0.3$ and $\theta = \pi/4$, energy per unit length of dislocation can be written as:

$$E_s = 0.58 Gb^2 \quad (4.4)$$

The energy stored by dislocations is related to the toughness at $0^\circ K$ as:

$$0.05 U_o = \rho E_s \quad (4.5)$$

where ρ is the dislocation density. Dislocation density can be estimated using this relation. Taking $G = 8.7 \times 10^{10} \text{ N/m}^2$ and $b = 2.5 \times 10^{-10} \text{ m}$ at $0^\circ K$, Eqs. 4.4 and 4.5 can be combined to get dislocation density. The estimated dislocation density values are given in Table 4.2.

Table 4.1: Intercept U_0 and slope S converted to shear values for the different test conditions

Test	S = Slope, $J/m^3/K$		U_0 = Intercept, $10^7 J/m^3$	
	9 Cr-1 Mo	316 SS	9 Cr-1 Mo	316 SS
Direct tensile	35524	42529	4.4893	6.7479
Fatigue	45239	57204	4.76430	7.1021
Fatigue + creep	44015	52576	4.6979	6.9971

Table 4.2: Estimated values of dislocation density and vacancy concentration for the two steels

Test	Dislocation density, $10^{15}/m^2$		Vacancy concentration, $10^{26}/m^3$	
	9 Cr-1 Mo	316 SS	9 Cr-1 Mo	316 SS
Direct tensile	0.711	1.06	2.55	3.83
Fatigue	0.755	1.12	2.71	4.03
Fatigue + creep	0.745	1.11	2.67	3.97

Vacancy concentration can be estimated from the energy used up in creating vacancies. The energy of formation of a single vacancy in Fe is 1.76×10^{-19} J (1.1 eV). The vacancy concentrations calculated for the three conditions are shown in Table 4.2.

The entropy of a dislocation array is composed of positional entropy, vibrational entropy of the dislocation line and vibrational entropy of the surrounding lattice. The first contains contributions from the position of dislocation loops in the lattice and from the possible internal configurations of the loop, it is estimated to be $2k$ per atomic length of dislocation line. The vibrational entropy associated with dislocations is about k per atomic length while the increase in vibrational entropy of the lattice is $2k$ per atomic length of dislocation. Thus the total entropy per atomic length of dislocation line is of the order of $5k$ per atomic length. The entropy per unit volume due to dislocations is then,

$$S_{\text{dis}} = 5k \cdot \frac{1}{b} \cdot \rho \quad (4.6)$$

The estimated entropy values are given in Table 4.3, columns 2 and 3.

The entropy associated with vacancy creation is given by

$$S_{\text{vac}} = k n \ln \frac{N}{n}; \quad N \gg n \quad (4.7)$$

where

n is the vacancy concentration and

N is the maximum possible vacancy concentration equal to the number of atomic sites per unit volume.

The entropy values calculated are tabulated in Table 4.3, columns 4 and 5.

The total entropy contribution due to dislocations and vacancies contribute only to about 50% of the entropy of deformation. The remaining part could be attributed to the heat dissipation in the specimen during deformation but the measurements in this connection were not carried out.

Table 4.3: Estimated entropy values due to dislocations and vacancies, total entropy and that attributed to the heat dissipation

Test	Entropy of dislocations $J/m^3/K$		Entropy of vacancies $J/m^3/K$		Experimentally obtained entropy $J/m^3/K$		Attributed to heat dissipation $J/m^3/K$	
	9 Cr-1 Mo	316 SS	9 Cr-1 Mo	316 SS	9 Cr-1 Mo	316 SS	9 Cr-1 Mo	316 SS
1	2	3	4	5	6	7	8	9
Direct tensile	196	292	22894	28359	35524	42529	12434	13878
Fatigue	208	309	24108	29546	45239	57204	20923	27349
Fatigue + creep	206	306	23805	29187	44015	52576	20004	23083

CHAPTER 5

CONCLUSIONS

The experimental results on different aspects of deformations can be used in arriving at the following conclusions:

1. The velocity stress exponent m^* for both the materials decreases with the increase in temperature without showing any abnormality in the temperature range of dynamic strain ageing.
2. In confirmity with the theories of thermal activation, effective stress is independent of strain at a constant temperature and at a constant strain decreases with increase in temperature and the internal stress increases with increase in strain at constant temperature and strain rate.
3. From the activation energy values of 4.8×10^{-19} J (2.99 eV) for 9 Cr-1 Mo steel and 3.6×10^{-19} J (2.25 eV) for the 316 SS, and the corresponding activation volume of 90 b^3 to 600 b^3 for 9 Cr-1 Mo steel and 50 b^3 to 800 b^3 for the 316 SS, determined from the strain rate change tests the rate controlling process can be identified as the intersection of two dislocations leading to the formation of two jogs.
4. Experimentally it is found that $V^* \tau^* = \text{Constant}$ giving rise to a hyperbolic relationship between activation volume V^* and effective stress τ^* .
5. With the rate controlling mechanism identified as dislocation intersection, the force (F)-distance (d) relationship is found to be of the type,

$$F = \text{Constant} \times d^{-0.5}$$

6. The diffusion of carbon atoms on to dislocations controls the process of dynamic strain ageing in 9 Cr-1 Mo steel in the temperature range 523K to 648K.
7. The activation volume for stress relaxation is found to be about 1/4 the activation volume required for plastic deformation as determined from strain rate change test.
8. The energy absorbed per cycle in load cycling increases with strain and at the same strain decreases with increase in temperatures.
9. The cause of microstrain in load cycling experiments may be attributed to the relaxation of carbon atoms from pinned positions of dislocations resulting in small dislocation motions. The process is simple in the 9 Cr-1 Mo steel whereas in 316 SS it is complicated because of the presence of stacking faults which give rise to in addition a Suzuki type of interaction with substitutional solution.

REFERENCES

1. S.J. Sanderson, ASM International Conference on Production, Fabrication, Properties and Application of Ferritic Steels for High Temperature Applications, Warren, Pa, p. 85 (1981).
2. G.V. Smith, Evaluation of the Elevated Temperature Tensile and Creep-Rupture Properties of 3 to 9 Percent Chromium Molybdenum Steels, ASTM (1975).
3. O.K. Chopra, K. Natesan and T.F. Kassner, Journal of Nuclear Materials, Vol. 96, p. 269 (1981).
4. Source Book on Stainless Steels, American Society for Metals, Metals Park, Ohio (1976).
5. B.P. Kashyap, K.M. Taggart and K. Tangri, Phil. Mag. (In Press).
6. J.L. Mannan, K.G. Samuel and P. Rodriguez, 6th International Conference on the Strength of Metals and Alloys, Melbourne, Vol. 2, p. 637 (1982).
7. R. Becker, Z. Physik, Vol. 26, p. 919 (1925).
8. R. Peierls, Proceedings of Phys. Soc. (London), Vol. 52, p. 34 (1940).
9. F.R.N. Nabarro, Proceedings of Phys. Soc. (London), Vol. 59, p. 256 (1947).
10. A. Seeger, Phil. Mag., Vol. 1, p. 651 (1956).
11. J. Lothe and J.P. Hirth, Phys. Rev., Vol. 115, p. 543 (1959).
12. A. Seeger, Dislocations and Mechanical Properties of Crystals, Wiley, New York, p. 243 (1957).
13. J. Friedel, Phil. Mag., Vol. 46, p. 1169 (1955).
14. N.F. Mott, Phil. Mag., Vol. 43, p. 1151 (1952).
15. A. Seeger, Phil. Mag., Vol. 46, p. 1194 (1955).
16. G. Schoeck and A. Seeger, Defects in Crystalline Solids, Phys. Soc. (London), p. 340 (1955).
17. J. Weertman, Journal of Applied Physics, Vol. 26, p. 2131 (1955).
18. N.T. Read, Dislocations in Crystals, McGraw Hill, New York (1953).

19. A. Seeger, *Z. Naturforsch.*, Vol. 9a, p. 758, 819, 856 (1954).
20. H. Conrad and H. Weidersich, *Acta Met.*, Vol. 8, p. 128 (1960).
21. J.W. Christian and B.C. Masters, *Proceedings of Roy. Soc. (London)*, Vol. A 281, p. 240 (1964).
22. J.C.M. Li, *Trans. of Metallurgical Society of AIME*, Vol. 223, p. 219 (1965).
23. J.C.M. Li, *Canadian Journal of Physics*, Vol. 45, p. 493 (1967).
24. P.W. Osborne, *Acta Met.*, Vol. 11, p. 998 (1963).
25. G.B. Gibbs, *Phys. Stat. Solidi*, Vol. 3, p. 693 (1964).
26. G. Schoeck, *Phys. Stat. Solidi*, Vol. 8, p. 499 (1965).
27. H.P. Hirth and W.D. Nix, *Phys. Stat. Solidi*, Vol. 35, p. 177 (1969).
28. W.G. Johnston and J.J. Gilman, *Journal of App. Phys.*, Vol. 30, p. 129 (1959).
29. W.G. Johnston and D.F. Stein, *Acta Met.*, Vol. 11, p. 362 (1963).
30. D.F. Stein and J.R. Low, *Journal of App. Phys.*, Vol. 31, p. 362 (1960).
31. H. Conrad, *Journal of Metals*, Vol. 16, p. 582 (1964).
32. J.T. Michalak, *Acta Met.*, Vol. 13, p. 213 (1965).
33. H. Conrad, *Mat. Sci. Engg.*, Vol. 6, p. 265 (1970).
34. E. Orowan, *Proceedings of Phys. Soc. (London)*, Vol. 52, p. 8 (1940).
35. W. Frank, *Phys. Stat. Solidi*, Vol. 26, p. 197 (1968).
36. A.S. Basinski and J.W. Christian, *Australian Journal of Physics*, Vol. 13, p. 299 (1960).
37. R.N. Gaurd, *Acta Met.*, Vol. 9, p. 163 (1961).
38. A.S. Keh, *Acta Met.*, Vol. 13, p. 213 (1965).
39. C.F. Jenkins and G.V. Smith, *Trans. of Metallurgical Society of AIME*, Vol. 245, p. 2149 (1965).
40. N. Charnock, *Phil. Mag.*, Vol. 18, p. 89 (1968).

41. A.H. Cottrell, Dislocations and Plastic Flow in Crystals, Clarendon Press, Oxford (1953).
42. A.H. Cottrell, Phil. Mag., Vol. 44, p. 829 (1953).
43. P.G. McCormick, Acta Met., Vol. 20, p. 351 (1972).
44. P.G. McCormick, Acta Met., Vol. 19, p. 463 (1971).
45. K. Mukherjee, T. May, C.D'Antonio and R.J. McClag, Met. Trans., Vol. 1, p. 3223 (1970).
46. R.W. Hayes and W.C. Hayes, Acta Met., Vol. 30, p. 1295 (1982).
47. Y. Nakada and A.S. Keh, Acta Met., Vol. 18, p. 437 (1970).
48. R.W. Hayes and W.C. Hayes, Acta Met., Vol. 32, p. 259 (1984).
49. R.A. Mulford and U.F. Kocks, Acta Met., Vol. 27, p. 1125 (1979).
50. A.W. Sleeswyk, Acta Met., Vol. 6, p. 598 (1958).
51. L.J. Cuddy and W.L. Leslie, Acta Met., Vol. 20, p. 1166 (1972).
52. P. Feltham, Journal of the Inst. of Metals, Vol. 89, p. 210 (1961).
53. P. Feltham, Phil. Mag., Vol. 6, p. 259 (1961).
54. G.A. Sargent, Acta Met., Vol. 13, p. 663 (1965).
55. B.J. Shaw and G.A. Sargent, Acta Met., Vol. 12, p. 1225 (1964).
56. P. Feltham, Phil. Mag., Vol. 6, p. 847 (1961).
57. P. Feltham, Phil. Mag., Vol. 8, p. 989 (1963).
58. P. Feltham, Phys. Stat. Solidi, Vol. 3, p. 1340 (1963).
59. D.A. Miller, R.H. Priest and E.G. Ellison, High Temp. Mat. and Processes, Vol. 6, p. 155 (1984).
60. P. Pequignot, J. Perj and P. Gobin, Trans. of Metallurgical Society of AIME, Vol. 239, p. 439 (1967).
61. M.N. Shetty, Unpublished work.
62. N. Bonfield and C.H. Li, Acta Met., Vol. 13, p. 317 (1965).
63. R. De Batist, Internal Friction of Structural Defects in Crystalline Solids, North Holland, p. 265 (1972).

64. G.T. Galyon, *Acta Met.*, Vol. 16, p. 897 (1968).
65. S. Glasstone, K.J. Laidler and H. Eyring, *The Theory of Rate Processes*, McGraw Hill (1941).
66. A.S. Krausz, *Acta Met.*, Vol. 14, p. 1851 (1966).
67. Z.S. Basinski, *Phil. Mag.*, Vol. 4, p. 393 (1959).
68. S.L. Mannan, K.G. Samuel and P. Rodriguez, *Trans. of the Indian Inst. of Metals*, Vol. 36, p. 313 (1983).
69. *Proceedings of Conf. on Strength of Metals and Alloys*, *Trans. Japan Inst. of Metals*, Vol. 9, Supplement (1968).
70. A. Majumdar and M.N. Shetty, *Australian Conf. on H.S.L.A. Steels*, p. 168 (1984).
71. M.N. Shetty and J.P. Hirth, *Met. Trans.*, Vol. 2, p. 297 (1971).
72. B. Weiss and R. Stickler, *Met. Trans.*, Vol. 3, p. 1014 (1972).
73. J.K. Lai and M. Mektash, *Met. Sci.*, Vol. 12, p. 415 (1978).
74. O. Engler, *Ann. Physik [5]*, Vol. 31, p. 145 (1938).
75. John H. Hoke, *Stainless Steels Handbook*, Editors: D. Pecker and I.M. Bernstein, McGraw Hill Book Co., N.Y., p. 21 (1977).
76. F.R.N. Nabarro, *Theory of Crystal Dislocations*, Clarendon Press, Oxford, p. 691 (1967).
77. I. Kovacs and L. Zsoldos, *Dislocations and Plastic Deformation*, Pergamon Press, p. 249 (1973).

Thesis

669.142

Up La

A 104244